EXPLORATION OF CALCIUM RICH MARINE BENTHOS BIO-WASTE TO DEVELOP BIO-GENIC HYDROXYAPATITE FOR BONE REGENERATION AND UV PROTECTION

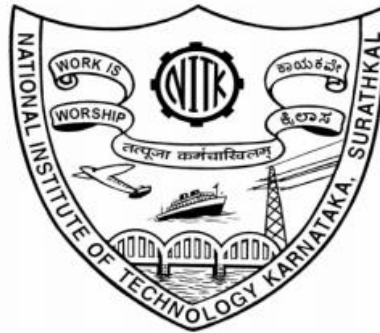Thesis

Submitted in partial fulfilment of the requirements for the degree of

DOCTOR OF PHILOSOPHY

By

KOMALAKRUSHNA HADAGALLI

(158027MT15F08)

DEPARTMENT OF METALLURGICAL AND MATERIALS ENGINEERING

NATIONAL INSTITUTE OF TECHNOLOGY KARNATAKA

SURATHKAL, MANGALURU – 575025

APRIL 2021

EXPLORATION OF CALCIUM RICH MARINE BENTHOS BIO-WASTE TO DEVELOP BIO-GENIC HYDROXYAPATITE FOR BONE REGENERATION AND UV PROTECTION

Thesis

Submitted in partial fulfilment of the requirements for the degree of
DOCTOR OF PHILOSOPHY

By

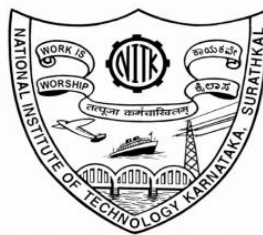**KOMALAKRUSHNA HADAGALLI**

(158027MT15F08)

Under the guidance of

Dr. Saumen Mandal

Assistant Professor

Department of Metallurgical and Materials Engineering,

NITK Surathkal

DEPARTMENT OF METALLURGICAL AND MATERIALS ENGINEERING

NATIONAL INSTITUTE OF TECHNOLOGY KARNATAKA

SURATHKAL, MANGALURU – 575025

D E C L A R A T I O N

I hereby *declare* that the Research Thesis entitled "**Exploration of calcium rich marine benthos bio-waste to develop bio-genic hydroxyapatite for bone regeneration and UV protection**" which is being submitted to the National Institute of Technology Karnataka, Surathkal in partial fulfillment of the requirements for the award of the Degree of **Doctor of Philosophy** in the Department of **Metallurgical and Materials Engineering**, is a *bonafide report of the research work carried out by me*. The material contained in this Research Thesis has not been submitted to any University or Institution for the award of any degree.

Place: NITK, Surathkal   Name: KOMALAKRUSHNA HADAGALLI
Date: 19-04-2021   Register Number: 158027MT15F08

Department of Metallurgical and Materials Engineering

CERTIFICATE

This is to certify that the Research Thesis entitled "**Exploration of calcium rich marine benthos bio-waste to develop bio-genic hydroxyapatite for bone regeneration and UV protection**" submitted by Mr. Komalakrushna Hadagalli (Register Number: 158027MT15F08) as the record of the research work carried out by him, is *accepted as the Research Thesis submission* in partial fulfillment of the requirements for the award of degree of Doctor of Philosophy.

Research supervisor

Dr. Saumen Mandal
Assistant Professor
Department of Metallurgical and Materials Engineering
NITK Surathkal

Chairman- DRPC

Chairman - DRPC
Dept. of Metallurgical and Materials Engineering
National Institute of Technology Karntaka, Surathkal
Post Srinivasnagar, Mangaluru - 575 025
Karnataka, India

DEDICATED TO

THE ALMIGHTY GOD……

ACKNOWLEDGEMENTS

<div align="right">KOMALAKRUSHNA HADAGALLI</div>

Abstract

In this study, a scalable biogenic synthesis of phase-pure hydroxyapatite $(Ca_{10}(PO_4)_6(OH)_2$, HA) (Ca/P = 1.66) scaffold from the marine-resource-derived HA together with different pore formers were conventionally sintered to produce physiologically relevant scaffolds with porous architecture. A combination of moderate compressive strength (12−15 MPa) with elastic modulus up to 1.6 GPa was achieved with ∼98% interconnected porosity using wheat flour as the pore former. More importantly, the faster nucleation and growth of the biomineralized apatite layer with full coverage within 3 days of incubation in a simulated body fluid, together with a combination of mechanical properties, establish the potential of marine-resource-derived biomimetic HA scaffold as a new generation of cancellous bone analogue. MTT assay and cell morphological analysis established the good cytocompatibility of naturally derived HA porous scaffolds, as evident from the good cellular adhesion, proliferation, and phenotypical features of osteoblast cells. The effect of Fe^{3+} ionic substitution in HA was studied using structural modification, such as lattice parameter, crystallite size, and particle size resulting into a drastic improvement in UV absorption through a tailored optical band structure. Ca^{2+} of HA being larger (0.99 Å) compared to Fe^{3+} (0.64 Å) contributes to the shrinkage of the lattice. Hence, hexagonal lattice parameters, a and c of HA are reduced successively as the concentration of Fe^{3+} increases, is observed via XRD. UV absorption of Fe-HA in the entire UVA and UVB range with an increase in Fe content because of the remarkable decrease in band gap with undoped and doped HA. Also, present work explores the use of marine resourced prawn exoskeleton/shell as a new class of naturally occurring composite containing UV absorbing proteins. Mycosporine-like amino acids with a central aromatic ring in the exoskeleton/shell of naturally occurring prawns (*Fenneropenaeus Indicus*) offer excellent UV protection. The presence of tryptophan, phenylalanine, and tyrosine, forming the basic building blocks of mycosporines, is confirmed by structural, compositional, and microscopic studies on prawn shells. The UV spectroscopic signatures at 290 and 320 nm provides strong evidence for the highest UV absorption. UV absorption attributes to the presence of mycosporine-like amino acids.

Keywords: Marine benthos, hydroxyapatite, scaffold, biomineralization, porosity, compressive strength, UV absorption, bandgap, sunscreen filter, UV absorption, Mycosporines.

Contents

Page left intentionally blank

NOMENCLATURE

HA	:	Hydroxyapatite
XRD	:	X- ray diffraction
SEM	:	Scanning electron microscopy
TEM	:	Transmission electron microscopy
XPS	:	X-ray photoelectron spectroscopy
EDS	:	Energy-dispersive X-ray spectroscopy
TGA	:	Thermo-gravimetric analysis
DSC	:	Differential scanning calorimetry
FTIR	:	Fourier transform infrared spectroscopy
UV	:	Ultraviolet
A.P.	:	Apparent porosity
B.D.	:	Bulk density
D	:	Dry weight
I	:	Immersed weight
S	:	Soaked weight
E	:	Young's modulus
SBF	:	Simulated body fluid
MC3T3-E1	:	The mouse osteoblast precursor cell line,
α-MEM	:	Alpha modified eagle's medium
DMEM	:	Dulbecco's modified eagle medium
FBS	:	Fetal bovine serum
PBS	:	Phosphate buffer saline

EDTA	:	Ethylene diamine tetra acetic acid
DMSO	:	Dimethyl sulfoxide
BSA	:	Bovine serum albumin
O.D.	:	Optical density

Page left intentionally blank

CHAPTER 1

INTRODUCTION

Hydroxyapatite (HA), ($Ca_{10}(PO_4)_6(OH)_2$) is a member of the Ca apatite family. It significantly resembles the natural bone in both chemical composition and structure. HA is the major mineral constituent (~ 67 wt.%) of natural bone and teeth. HA, owing to its biocompatible and bioactive properties, has been commonly employed as an implant material in bone tissue repair/regeneration (osteogenesis) (Basu 2017). Due to its bioactive nature, HA is substantially used for various bone repairs and regeneration and as coatings for metallic artificial devices to enhance their biological properties (Tripathi and Basu 2012). Among all calcium phosphates, HA is thermally the most stable compound under physiological conditions (Basu 2017).

HA and its derivatives are widely-explored biomaterials by a number of researchers with various processing techniques for its potential biomedical applications. HA powder can be synthesised by various methods, which are predominantly based on a chemical reaction between Ca and P-based salts. In the case of pure phase HA, the stoichiometric (Ca/P) ratio has to be equal to 1.67. HA can also be developed from biological resources. Marine resources such as skeletons of dead benthos can be utilised as a raw source for the synthesis of biogenic and biocompatible HA as they encompassed with $CaCO_3$. The conversion of natural seashells, bone ash, and eggshells can provide better biological properties due to the existence of advantageous cations like Mg^{2+}, K^+, Sr^{2+}, Na^+, Zn^{2+}, and so on or anions like Cl^-, SO_4^{2-}, F^-, and CO_3^{2-}. The existence of these ions is reported to facilitate rapid bone regeneration (Akram et al. 2014).

Porous HA is recurrently used as a biocompatible material to assist cell predestination for bone tissue engineering (Tripathi and Basu 2012). The scaffolds having interconnected porosity ideally enhances cell attachment and its growth, thus facilitating the required nutrient supply for bone tissue ingrowth (Basu 2017). It should enable the desired interlocking between the implanted biomaterial and the host natural bone, thus provide significant mechanical stability at the critical surface. In the last two decades, appreciable attention has been paid to the development of porous HA scaffolds

with interconnected pores for bone tissue engineering. Along with interconnected porosity, the HA scaffold should possess high mechanical strength, as the cortical bone has an elastic modulus in the range of 1− 20 GPa and a strength of 1− 100 MPa. Alike, cancellous (trabecular) bone requires an elastic modulus of 0.1 to 1.0 GPa and strength of 1−10 MPa (Sabree et al. 2015). Scaffolds are associated with a highly porous structure and a large surface area to favour cell attachment and proliferation. Along with considerable strength, they should possess porosity ranging from 40 to 90 % to encourage angiogenesis and osseointegration (Sabree et al. 2015). Also, extracellular fluid flow is facilitated by the porous HA scaffolds for biological fixation. Also, the pores give a mechanical interlock, which improves the bond strength between the porous HA scaffold surface and surrounding tissues to enhance osteoconductivity (Hannink and Arts 2011). From a biocompatibility point of view, the pore size and distribution play key roles in the adhesion and proliferation of osteoblast cells. The interconnected pores allow cells to migrate in multiple directions *in vivo*. Also, the vascular network and sufficient blood supply are crucial for the initiation of the vasculature, which leads to faster bone regeneration. Although porous HA has been extensively explored over the last three decades, a scalable biomimetic synthesis approach to develop HA with tailored porosity and tunable properties has still not been accomplished.

HA and its derivatives are well-known ceramic materials, have versatile applications other than bone tissue engineering such as antibacterial surface (Ag, Sr, Zn, doped in HA), toothpaste manufacturing (as remineralizing agent), catalysis, protein separation, water purification etc. Experimental nanostructured composite air filters containing hydroxyapatite were found to be efficient in absorbing and decomposing CO, which could eventually lead to its use in reducing automotive exhaust pollutants. Also, HA powder and its coating can be used in cosmetics (UV absorbing in sunscreen filter) and coating on UV sensitive food and drug packing). Commercially available sunscreen filters are categorized as organic or chemical and inorganic or physical filters depending on mechanisms to mitigate UV rays. Organic filters, those work on the principle of chemical changes in molecules to absorb UV rays, include salicylates, PABA esters, para-aminobenzoic acid (PABA), cinnamates,

benzophenones, etc. While, TiO_2 particles envelop a broad range of protection from UVA to UVB, whereas ZnO covers the whole UVA range (Piccirillo et al. 2014). Micron-sized TiO_2 and ZnO were initially used in sunscreens, as they have high a refractive index the sunscreen emerges unnaturally white on the skin by losing its aesthetic worth. To suppress the drawbacks occurring from micron-sized particles, it is replaced by nano-sized particles and combining of micron and nanosized together to further accomplish the required range of UV absorption. TiO_2 and ZnO, both oxides are phototoxic due to their photocatalytic reactivity under UV irradiation. To overcome the problem associated with existing filters, it is essential to introduce compatible sunscreen filters in all aspects. Ideal sunscreen filters must have the following two important characteristics, such as (a) absorption of the entire UV range and (b) compatibility with skin. It should not have any effect on the skin through the generation of reactive species (Antoniou et al. 2008). In this concern, the exploration of sunscreen filters using HA can be of attentiveness as HA having promising biocompatible properties. The selection of HA as a sunscreen filter is appropriate, owing to tune its property of UV absorption with the aid of incorporation of metal ions. In parallel, natural resources-based sunscreens are more effective than chemical and physical sunscreens as they won't produce free radicals.

Apart from synthetic UV absorbing materials, natural resources based materials namely, fish lenses and marine based mucus contain mycosporine-like amino acids, which facilitate the absorption of UV radiations. Mycosporine-like amino acids, namely, tryptophan, porphyra-334, shinorine, mycosporine-glycine, phenylalanine and tyrosine absorb the whole UV range due to the presence of complex amino acid with the central aromatic ring (Fernandes et al. 2015). Owing to these exceptional properties, these new categories of amino acids can be utilized as necessary ingredients in sunscreen products.

CHAPTER 2 deals with the existing literature in the area of the structure, properties and applications of hydroxyapatite and its products for bone tissue engineering, Besides, different biological resources to acquire hydroxyapatite and an overview of special applications like sunscreen filters are addressed. **CHAPTER 3** brings the study of hydroxyapatite from marine bio-waste; dense and porous HA**.**

CHAPTER 4 is dedicated to the *in vitro* cytocompatibility study. **CHAPTER 5** covers the study of Fe incorporated hydroxyapatite as promising sunscreen filters. **CHAPTER 6** addresses the exploration of the prawn exoskeleton as UV absorbing material. **CHAPTER 7** is devoted to the conclusions of the overall study.

CHAPTER 2

LITERATURE REVIEW

2.1 Introduction

In the last few decades, there has been extensive development in the field of biomaterials, which includes ceramics, metal alloys and composites. New materials are explored for various medical applications to improve the human's life quality. Bioceramics both dense as well as porous has been broadly used in biomedical applications, includes bone repairs, bone grafts, bone fillers, spinal fusion, bone fillers, maxillofacial reconstruction, etc (Figure 2.1). Calcium phosphates are the most essential materials that have been probed extensively in bone tissue engineering because human bones majorly contain Ca and P compounds as an inorganic constituent. Among all variety of calcium orthophosphates, hydroxyapatite (HA), $(Ca_{10}(PO_4)_6(OH)_2)$ with the Ca/P ratio of 1.67 mimics ingredients of human bone. HA exhibits outstanding specific properties like biocompatibility, osteoconductive, non-inflammatory, non-toxic and non-immunogenic. Moreover, HA has a structure and composition similar to human bone (Basu 2017; Prakasam et al. 2015). A wide range of techniques is available to synthesize HA such as hydrolysis, hydrothermal, combustion, wet chemical, sol-gel, mechano-chemical, micro-emulsion, spray pyrolysis, microwave, solid-state synthesis etc. The wet chemical route has been explored to synthesize HA powders with high level purity and homogeneity. This route has been broadly used by the researchers because it is simple, involved in low-temperature reactions and cost effective.
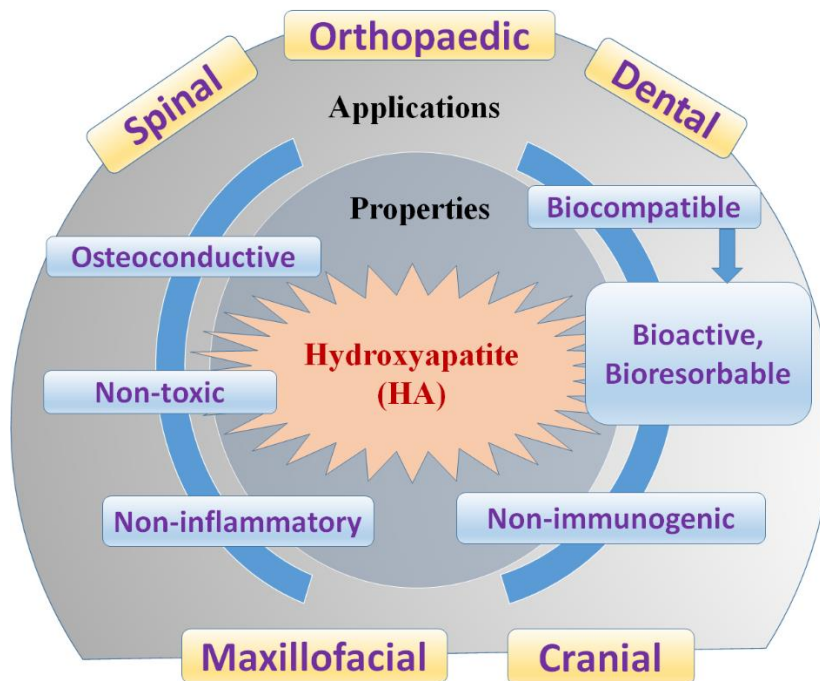
Figure 2.1: Schematic representation of different biomedical properties of hydroxyapatite and its applications.

2.2 Bone properties and its structure

Bone tissue is a hard tissue that is made of various cell types namely, osteoblast cells (bone forming), osteocytes (matured osteoblasts), osteoclasts cells (bone resorbing), and bone lining cells that construct a protective layer on the bone surface. Osteoblasts and osteocytes take part in the new bone formation and bone mineralization. The chemical composition of bone is divided into two phases inorganic (~ 67 %) and organic (~ 33 %). Hydroxyapatite is the prime constituent of the inorganic phase and collagen (28 %) with protein (5 %) is considered as organic phase (Figure 2.2). Bone tissue is encompassed of two well defined forms, cancellous bone and cortical bone. Cortical bone is also called compact bone which is denser, while cancellous bone is called trabecular or spongy bone which is consisted of a porous structure. The extremely hard exterior is formed by cortical bone, while the hollow interior of the bone is filled by the cancellous bone. Cortical bone has a reported Young's modulus of 1– 20 GPa and a strength of 1– 100 MPa. Similarly, cancellous bone exhibits Young's modulus of 0.1– 1.0 GPa and strength of 1–10 MPa. The

appropriate dimensions and suitable architecture of the scaffolds are needed to fulfill the requirements of mechanical stability and support the required biological activities (Sabree et al., 2015).
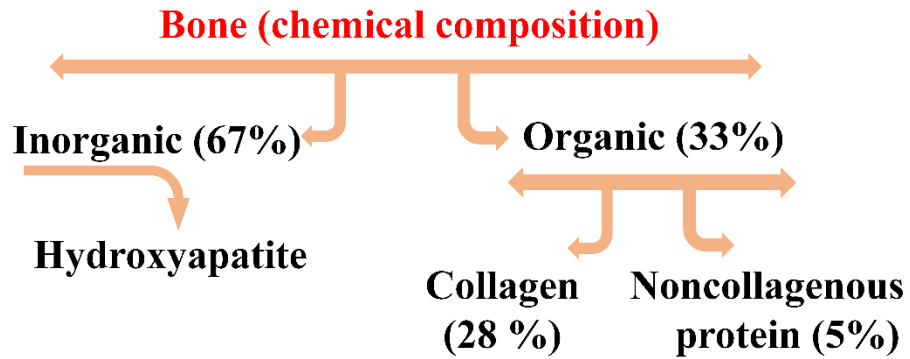
Figure 2.2: Chemical composition of human bone

2.3 Hydroxyapatite (HA)

HA ($Ca_{10}(PO_4)_6(OH)_2$) is an inorganic compound consisting of calcium phosphate which builds up most of the human bone and tooth structure. Pure HA is white colour, having a stoichiometric Ca/P ratio of 1.67, possesses hexagonal crystal structure (Figure 2.3) with lattice parameters a = b = 9.54534 Å, c = 6.91907Å. HA is the thermodynamically most stable compound under physiological conditions of the body fluids.
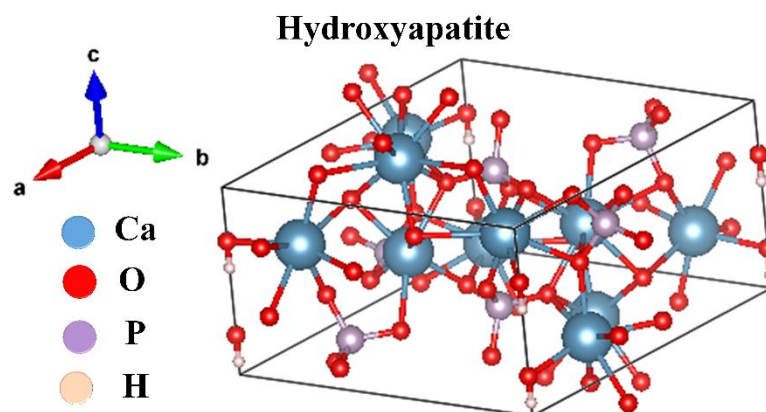
Figure 2.3: Hydroxyapatite crystal structure.

There are multiple methods to synthesize HA with a Ca/P ratio of HA phase close to 1.67. Available synthesis methods are tabulated in Figure 2.4, namely wet chemical method, dry method and extraction from biological resources. In a solid-state method, ingredients are mixed mechanically by milling and then calcined at a high temperature. Various kinds of calcium and phosphate ions based salts are used as precursors. Due to the calcination at high temperatures, a well crystallized structure of HA is acquired as the final product.

In the wet chemical route, chemical precipitation is an easy procedure to obtain HA. In this procedure, different Ca and P ion containing precursors are used for chemical reactions to produce HA. The dropwise addition of one reagent to the other are performed under continuous stirring with temperature $\sim 60 - 80\ ^{\circ}C$ to obtain precipitation of HA. The final precipitation is first washed with DI water to remove unreacted Ca compounds, then filtered with filter paper followed by drying in the oven to obtain milky white HA. HA can also be directly extracted from various biogenic sources, namely sea-shell, bovine bone, fish bone, fish scale, coral etc. This method is of particular interest because of its economic and environmental advantages. In parallel products closely resemble the bioapatite and are found to be more bioactive than HA which is produced synthetically.
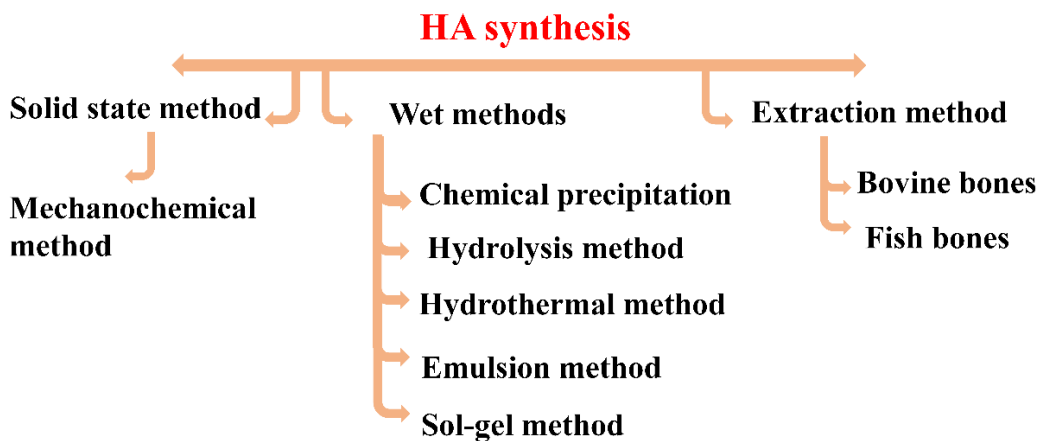
Figure 2.4: Different categories of synthesis routes to obtain HA

2.4 Hydroxyapatite from biological resources

2.4.1 Hydroxyapatite extraction/synthesis from natural sources

Biological origin based biomaterials have acquired more importance in developing and designing bioceramics mainly hydroxyapatite and its precursor. Any material which is natural or manmade can be a biomaterial as long as it serves the stated medical and surgical determination for ultimately secure implantation in or on the human body. Nature has contributed a wide range of materials with remarkable functional properties (Ramdan et al. 2016). The schematically summarized biological sources for HA and its precursors are shown in Figure 2.5. The consumption of natural resources, which are largely available can be a better biological source for HA. Natural resources are also a promising alternative to Ca precursors to produce phase-pure HA. HA synthesized from natural biowaste can be more advantageous as it often contains advantageous ions, which are also detected in the biological HA (Akram et al. 2016).
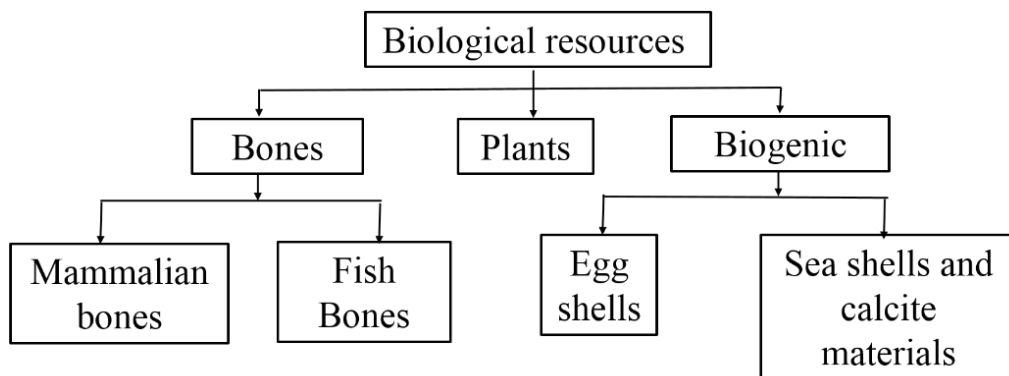
Figure 2.5: Different categories of biological resources for the extraction/synthesis of HA (Akram et al. 2014).

Despite the great variety of HA synthesis methods, but a few of them are satisfactory in terms of economic effectiveness and performance, mainly due to the diverse materials needed in the synthesis of hydroxyapatite. Figure 2.6 shows the preparation of HA via a variety of biogenic resources (Sadat et al. 2013). Five different biogenic sources of HA, together with minerals extraction from biowaste,

synthesis from eggshells, biomembranes, the exoskeleton of marine organisms, and with the aid of natural biomolecules.
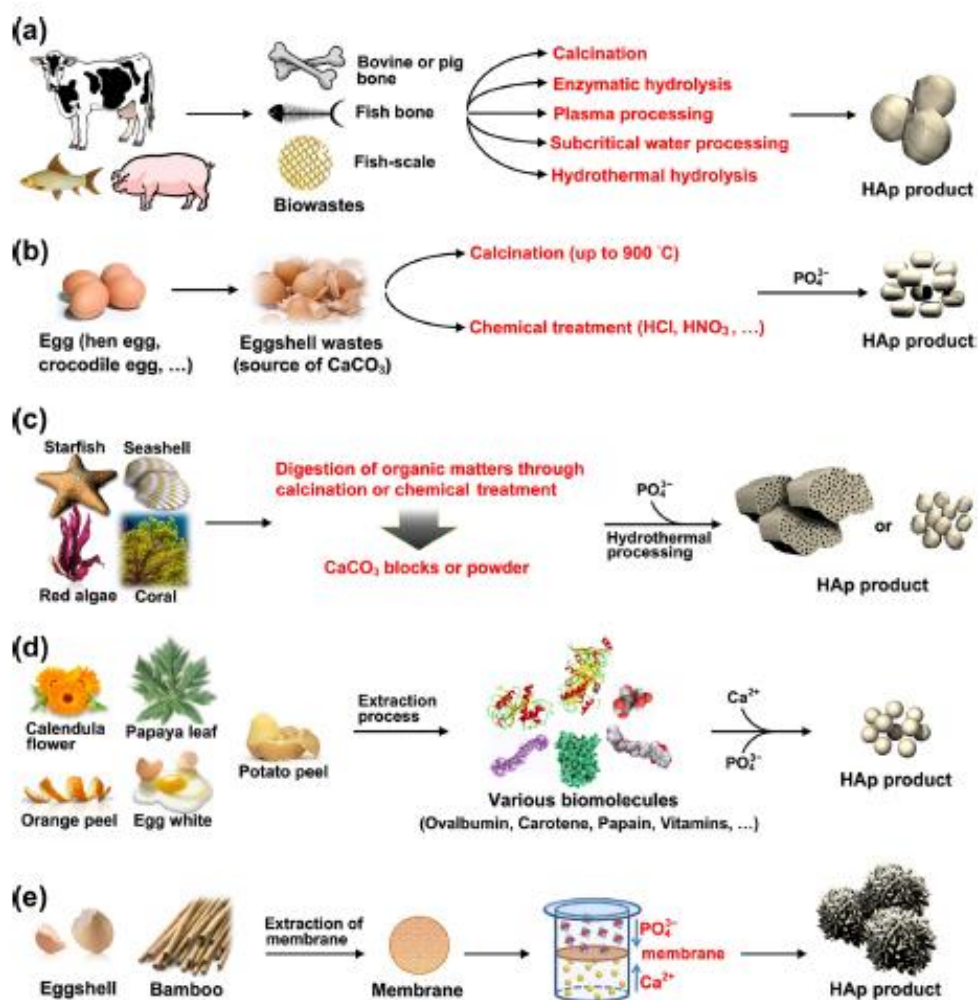
Figure 2.6: Preparation of HA via biological resources: (a) extraction of minerals from biowaste, synthesis from (b) eggshells, (c) exoskeleton of marine organisms, (d) the aid of naturally derived biomolecules and (e) biomembranes (Sadat et al. 2013).

2.4.2 Marine resources

About 72% of the earth is enclosed by water which is split by oceans, lakes, rivers, etc. out of which 97 % belongs to oceans. Oceans consist of not only salt water, an abundant resource of food, medicine and numerous minerals. Marine-derived biomolecules such as natural compounds, proteins, etc. are getting much importance in

medicine and engineering. The huge availability of calcium rich marine benthos biowaste leads to a large conversion of HA. Several inventions include shells of marine mollusks such as nacre shells, sea snails, sea coral, cuttlefish bones etc. Synthesis of HA with tropical sea snail shells based raw precursors (Tiger Cowrie–Cypraea Tigris) was reported by Sahin *et.al.* using chemical synthesis (Choug et al. 2015). Agaogullari *et.al.* produced Ca-phosphate powders, namely $CaHPO_4$ and TCP containing nano-sized particles by hotplate methods and ultrasonic from sea urchin (Ağaoğullari et al. 2012). Natural gypsum, bovine bone, natural calcite and cuttlefish bones were used to obtain HA (Herliansyah et al. 2012). Malaysian cockle shells based raw sources are the potential for versatile biomedical engineering applications. Synthesis of HA from dead snail was disclosed with excellent properties, so needed for bone tissue replacement (Adak et al. 2011).

Marine resources such as skeletons of dead species were utilised as resources to synthesize biocompatible hydroxyapatite (Clarke et al. 2014). Sea Urchins (*brissus latecarinatus*) (Ağaoğullari et al. 2012), sputnik sea urchin (*phyllacanthus imperialis)* (Tămăşan et al. 2013), sea snail (*trochidae infundibulum concavus*) (Tămăşan et al. 2013), eastern oyster (*crassostrea virginica*) (Yoon et al. 2011)*,* conch shells (*strombus gigas*) (Vecchio et al. 2007), giant clam (*tridacna gigas*) (Vecchio et al. 2007), *thunnus obesus* bone (Venkatesan et al. 2011), sea snail (*cerithium vulgatum*) (Gunduz et al. 2014), land snails (*helix aspersa*, *helix pomatia*) (Kel et al. 2012), sea snail (*rapana venosa*) (Ozyegin et al. 2011) and cuttlefish bone (*sepia officinalis*) (Faksawat et al. 2015; Ivankovic et al. 2009; Kim et al. 2014) were documented as a natural resource of HA synthesis for application the field of biomedical engineering. Cuttlefish bone having two verities of layers namely lamellar matrix and dorsal shield. The dorsal shield has dense morphology whereas the lamellar matrix consists of a porous structure (90% porosity) of aragonite; hence lamellar matrix is preferable to synthesize hydroxyapatite, because of its abundant availability and porous nature (Cadman et al. 2012).

Natural resources like sea shells based calcium phosphate, such as HA is suitable material for bone tissue repair and regeneration engineering. Ca-P based bioceramics are bioactive chemical compounds that can be employed as bone scaffolds since they generate ions during the interaction with the body fluid and can promote precipitation of apatite on the surface (Sahin et al. 2019).

2.4.3 Availability of marine benthos

Generally, benthos is the assemblage of organisms that inhabit on, in, or near the seabed. A rocky shore is an intertidal area where the land and sea meet, between the high and low tide zones. Worldwide these complex marine ecosystem is found along coastlines. It has an abundance of nutrients and oxygen which is home to a variety of organisms such as barnacles, periwinkle snail, sea anemone, isopods, sea star, mussels, hermit crabs, limpets and chitons (Figure 2.7).
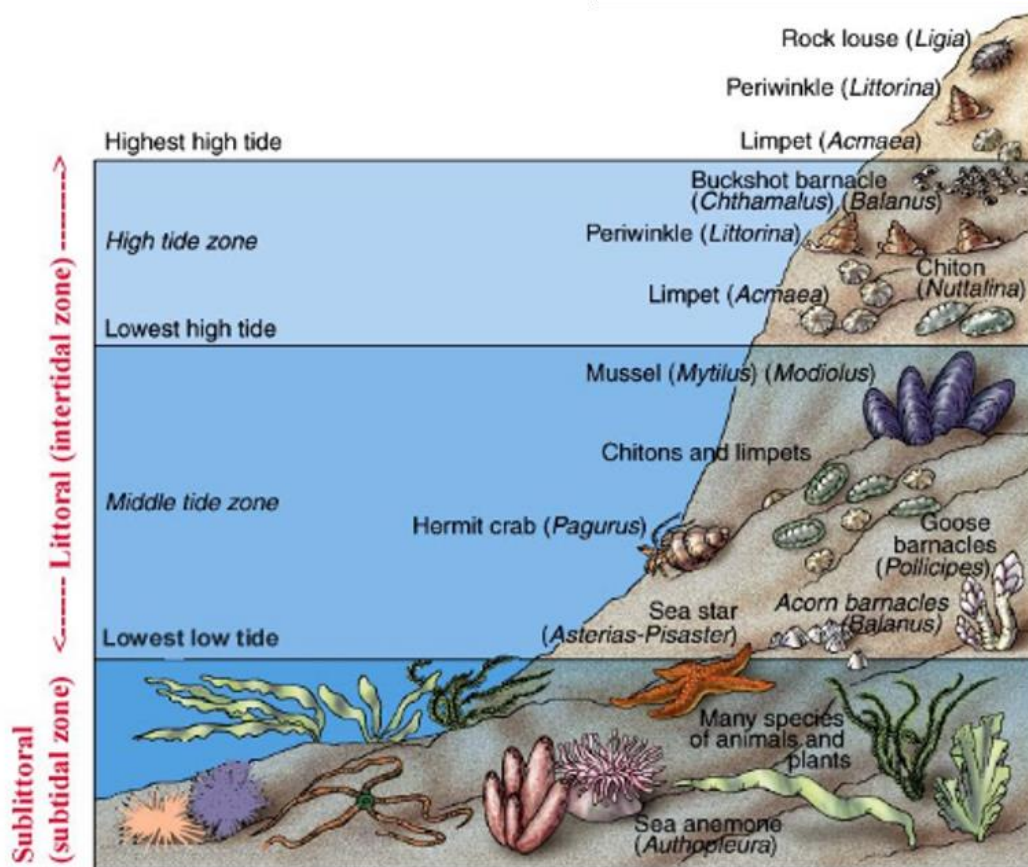
Figure 2.7: Rocky shore (Intertidal Zonation) zonation (https://www.pathwayz.org)

A rocky shore is an intertidal area that contains solid rocks. It includes many variety habitat types like steep rocky cliffs, rock pools, platforms and boulder fields that are biologically rich. Owing to the continuous action of the tides, it is distinguished by erosional features. Along with the sunlight, wind and other physical factors, a complex environment is created. Organisms that live in this area experience daily fluctuations in their environment. Benthos must be able to tolerate extreme changes in salinity,

temperature, moisture and wave action to survive. In Zonation, each region on the coast has a specific group of organisms that form distinct horizontal bands or zones on the rock. The intertidal zone can be classified as the following three zones.

- **High tide zone** is also called the high intertidal zone. This region is only flooded during high tides. Organisms found here are barnacles, anemones, crabs, chitons, isopods, mussels, sea stars, sea snails etc.
- **Mid tide zone** is also called a mid-littoral zone. This is a turbulent zone that is covered/uncovered twice a day. Common organisms are sponges, sea stars, snails, barnacles, mussels, crabs etc.
- **Low tide zone** is also called the lower littoral zone: This region is usually covered with water. It is only uncovered when the tide is extremely low. In contrast to the other zones, the organisms are not well adapted to long periods of dryness or extreme temperatures. The common organisms in this region are crabs, brown seaweed, sea cucumber, mussels, sea lettuce, sea urchins, shrimps, snails, tube worms etc.

Figure 2.8: Optical photograph of live cuttlefish (Deravi et al. 2014)

(http://tuttjaquatics.blogspot.com/2013/11/common-cuttlefish.html)

Figure 2.8 shows the optical photograph of live common cuttlefish (*Sepia officinalis*), which is the largest and best known. Cuttlefish like tropical water and are found on sandy sea floors as their habitat. (Deravi et al. 2014). Cuttlefish have an internal structure called the cuttlebone, which is porous and is made of aragonite (Cadman et al. 2012).

2.5 Synthesis of biocompatible calcium phosphates from marine resources

Many researchers have reported the potential use of marine benthos as precursors in the production of bioceramics for various biomedical applications. Table 2.1 contains a summary of the synthesis of calcium phosphates from different marine resources.

Table 2.1: A summary of synthesis of calcium phosphates from marine resources.

Sl No	Marine Species	Synthesis route	Calcium phosphate phase	Key points	Reference
1	*Strombus gigas* (conch) and *Tridacna gigas* (giant clam) shells	Hydrothermal	Dense HA	Enhanced mechanical properties of HA, Histological study reveals newly formed bone	(Vecchio et al. 2007)
2	*Cerithium vulgatum* sea snail	Chemical	Nano-hydroxyapatite and TCP	Structural, morphological analysis of biphasic bioceramic	(Gunduz et al. 2014)
3	*Rapana venosa* snail shell	Hydrothermal	HA	Structural, morphological analysis of HA	(Antoniac et al. 2015)
4	Abalone shell.	Hydrothermal solid-state conversion	Hydroxyapatite nano rods	Structural, thermal analysis of HA	(Chen et al. 2015)
5	*Mytilus sp* (brown mussel)	Wet chemical reaction	Electrospinning of HA on Ti-6Al-4V alloy	Structural, morphological analysis of coating of HA on Ti-6Al-4V	(Santhosh et al. 2012)
6	*Thunnus obesus* bone	Alkaline hydrolysis and thermal calcination	HA crystals	Biocompatibility of HA crystals with human osteoblast-like cell MG-63, no cytotoxicity and more cell proliferation	(Venkatesan et al. 2011)
7	Sea coral	Hydrothermal	Coralline hydroxyapatite for bone regeneration	HA with growth factors encourage ingrowth of osseous tissue, initiation of	(Nandi et al. 2015)

				bone healing and complete union between scaffolds and natural bone	
8	Sea Urchins (*brissus latecarinatus*)	Hot plate and ultrasonic method	Ca-phosphate powders; monetite and TCP,	Structural, morphological analysis of nano-size particles	(Ağaoğullari et al. 2012)
9	Indian sea coral genus (*Goniopora*)	Under hydrothermal conditions.	HA granules	Structural, thermal analysis of HA, apatite granules are more stable confirmed by *in vitro* solubility assay	(Sivakumar et al. 1996)
10	Sea shell (*Anandara Granosa*)	Hydrothermal	HA	Structural, morphological analysis of HA	(Fadli et al. 2014)
11	Atlantic cod fish bone	Calcination and $CaCl_2$ treatment	Single phase HA and biphasic HA/β-TCP;	bioactivity haemocompatibility, and no cytotoxicity, new crystal formation in SBF	(Piccirillo et al. 2015)
12	Snail shells (*rapana thomasiana)*	Chemical hot-plate stirring	HA/TCP	Structural, morphological analysis of biphasic bioceramic	(Ozyegin et al. 2012)
13	Cuttlefish bone	Hydrothermal	HA granules	Better biocompatibility in the *in vivo* rabbit calvaria and supported bone regeneration	(Kim et al. 2014)
14	Cuttlefish bone	Precipitation	HA	Crystallite size of HA increased with increase sintering temperature	(Faksawat et al. 2015)
15	Land snail shell (*helix pomatia* and *helix aspersa*)	Ultrasonic stirring and hotplate stirring	Monetite ($CaHPO_4$), florapatite (FA) $Ca_5(PO_4)_3F$	Structural, morphological analysis of different phases	(Kel et al. 2012)
16	Snail shell	Sol–gel	Nano crystalline pure HA and biphasic calcium phosphate (HA+ β-TCP)	In MTT, NIH-3T3 fibroblast cell lines which indicated that the viability was not affected in various concentrations of HA	(Anjaneyulu et al. 2016)

2.6 Porous hydroxyapatite in tissue engineering

Tissue engineering is a multidisciplinary subject that connects biology, engineering and medicine with immense potential healthcare solutions. Tissue engineering proceeds primarily on site–specific tissue architecture by manipulation of cells, scaffolds and biological cues. Particularly, a scaffold acts as the matrix that serves as a host for tissue formation. Scaffolds to enable tissue formation should have a few basic requirements, such as high porosity, sufficiently large pores and specific surface properties which enable the adhesion of the cell tissues, differentiation and proliferation; hence mechanical integrity is maintained by predetermined tissue structure and biocompatibility. The scaffold should ideally provide an environment for tissue engineering by evading hostile immunogenic response, when it degrades in a sustained manner, *in vivo.* The scaffolds for bone tissue engineering require materials to mimic the functional properties of natural bone while allowing the proliferation of bone cells to undergo osteogenesis. HA porous scaffolds have osteoconductive and resorbability properties which help in the fast ingrowth of bone. Scaffolds have porous morphology with high surface area exhibit strong bonding and mechanical interlock of scaffold and bone. Moreover, the interconnected pores allow the bone tissues to grow well hence the strength of bonding increases.

Porous HA has been widely used for artificial bone substitutes, different types of manufactured porous HA materials are as shown in Figure 2.9. The main purpose of tissue engineering is regeneration, repair, and reconstruction of damaged, lost or degenerative tissues. Although bone tissue itself shows an excellent ability of bone regeneration, in case of big bony defect or such situations bone healing process becomes difficult where bone grafts are required. At this point, it is very crucial to match the osteoconductive properties of porous HA scaffold on one side with the osteoinductive or osteogenic properties of living bone cells on the other side (Sopyan et al. 2007).

2.6.1 Fabrication of porous hydroxyapatite scaffolds

A wide range of methods has been adopted by various research groups for the development of HA based scaffold like the polymeric sponge method, the addition of

fugitives, starch consolidation method, foaming, freeze casting, multi pass extrusion, protein consolidation method, gel casting, etc (Dash et al. 2015).
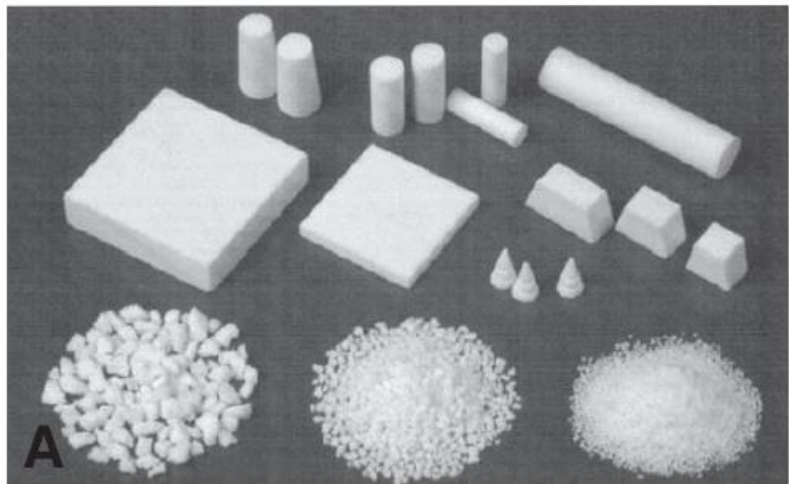
Figure 2.9: The different types of porous-ceramic hydroxyapatite products (Yoshikawa et al. 2005).

Fabrication of porous structure with pore-creating organic (volatile) particles is a standard practice, where pore formers burn away during sintering. Different kinds of pore making agents including flour, starch, paraffin, naphthalene, hydrogen peroxide, carbon or synthetic polymers such as polyvinyl butyral etc. are admixed to HA powders or slurries. After compaction, the organics burn away from the green compact during sintering. It allows direct control over the pore characteristics since their fraction, morphology, size and distribution is controlled by type, amount and properties of the added volatile phase. Removal of pore-forming organics can either be conducted by physical processes like evaporation, sublimation or chemical reactions like combustion etc (Sopyan et al. 2007).

Albayrak et al. 2016 carried out a study on commercial HA and urea as pore former. The two different amounts of urea (25 and 50 wt%) were processed using both calcined and uncalcined HA. To investigate the variation of density, hardness and compressive strength, cylindrical porous specimens were prepared. Figure 2.10 represents the variation of density and compressive strength as the function of the addition of pore former (urea with 0, 25, 50 wt.%). It was found that compressive strength and micro hardness of HA increased with increasing sintering temperature

from 1100 to 1200 ºC. Calcination of HA powder adversely affects the densification and reduces the sinterability of HA further resulted in the deterioration of mechanical properties.
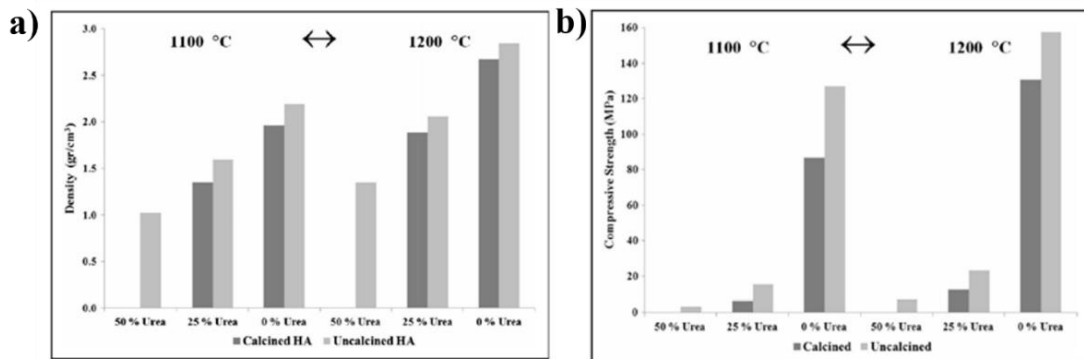
Figure 2.10: (a) Densities and (b) compressive strength of the sintered samples at 1100 ºC and 1200 ºC using calcined and uncalcined HA powders with varying content of urea (Albayrak et al. 2016).

Dash et al. 2015 reported HA scaffolds that were processed using varying content of naphthalene (10–40 vol%) as pore former through a combination of gel casting and fugitive addition. The highest compressive strength was 7.51 MPa reported for 22% porosity samples, and it was 0.75 MPa for 81% porosity samples. Scaffolds processed with lower solid loading had good pore interconnectivity. *In vitro* bioactivity assessment of the scaffolds showed dissolution of scaffold up to 3 weeks in SBF solution followed by deposition of calcium phosphate as apatite layer. MTT assay results revealed an acceptable limit of cell growth and proliferation.

Theoretically, a degradation rate of the scaffolds closer to the expected rate of tissue formation. Therefore, one of the important aspects in the development of bone and organ substitute materials is the fabrication of supporting matrices or scaffolds with an appropriate micro and macroscopic structural morphology including pore size, pore interconnectivity, biocompatibility, osteoconductivity, mechanical strength, and biodegradability.

Porous scaffolds with a large range of pore size are essential to reach all the activities involved in osseointegration. The pore size of 20–50 μm diameter may give a favorable function for physiological liquid exchange, while pores with a diameter of 100–350 μm are suitable for cell colonization and vascularization leads to bone

penetration into ceramics structure (Sopyan et al. 2007). A few researchers are following different procedure and pore formers to make the porous structure as tabulated in Table 2.2

2.7 Biomineralization of hydroxyapatite scaffolds

Biomineralization can be evaluated by new apatite generation on a material in simulated body fluid (SBF) to predict the *in vivo* bone bioactivity of a material. SBF solution can be prepared in the laboratory with appropriate quantities of ingredients like $NaCl$, $NaHCO_3$, KCl, $K_2HPO_4 \cdot 3H_2O$, $CaCl_2$, $MgCl_2 \cdot 6H_2O$, Na_2SO_4, and tris buffer added to one litre of double distilled water to have an ionic concentration of different inorganic ions similar to those of the human blood plasma. Porous scaffolds are dipped into the SBF solution as a function of days to observe new apatite layer formation (Kokubo and Takadama, 2006). Table 2.2 shows the brief information of various reports on porous HA scaffolds prepared from several pore formers in addition. In this comparative data, the values of porosity, compressive strength and modulus are tabulated. Also, few reports have demonstrated *in vitro* biomineralization in SBF, different time points of incubation result in the formation of a new apatite layer of HA on the porous surface as reported in Table 2.3. Chavan et al. 2010 reported the formation of a new apatite on HA surface with porous interlinked apatite layer when incubated at a period of 50 days in SBF solution (Figure 2.11). Porous apatite layers may enhance the osteoconduction and osteointegration properties.

During the period of incubation in SBF solution, the formation of a new apatite layer on the surface comes across a sequence of chemical reactions like spontaneous precipitation, nucleation and growth of calcium phosphates. The surface chemistry plays a principal role in the biomineralization process and the functional groups present in the materials have a predominant effect on the bone bonding property (Chavan et al. 2010). It is familiar that HA structure is made up of Ca^{2+}, PO_4^{3-}, and OH^- groups, which are closely packed together.

Table 2.2: Fabrication of porous HA scaffold with different pore formers and methods

Sl No	Hydroxyapatite	Pore formers	Pore forming method	Key points	Reference
1	Commercially available HA	Urea particles	Uniaxial pressing into cylindrical specimen with 8 KN	Urea 25% and 50 % addition to HA, density and compression strength variation study	(Albayrak et al. 2016)
2	Hydrothermally synthesized HA	Urea	Urea is incorporated during HA synthesis, isostatically pressed at 400 MPa	variation of pore size with respect to sintering temperature	(Veljović et al. 2011)
3	Commercially available HA	Polyurethane sponges as a template	Polymer replication method	pore diameters ranging from 100 - 400 µm were observed.	(Teixeira et al. 2009)
4	Hydrothermally synthesized HA	Silk sericin	silk sericin solution used to synthesize porous HA	Degradation study of $CaCO_3$ and HA	(Zhong et al., 2016)
5	HA synthesized by precipitation method.	Carbon powder as pore forming agent, ethylene vinyl acetate copolymer as thermoplastic binder, stearic acid as lubricating agent,	HA shell with 20 mm external diameter and 2 mm thickness was warm pressed in a cylindrical die at 100 °C	*In-vitro* MTT assay, *In vivo* study; material interaction and bone regenerating ability in a living system by implanting the scaffold in white New Zealand rabbit	(Jang et al. 2014)
6	HA synthesized via Precipitation route	Polyurethane sponges as a template	Scaffolds were prepared using polymeric sponges infiltrated with the ceramic slurry method	Homogeneous pore distribution and pore wall thickness; pore size varies between 100 µm and 300 µm, the pore wall thickness was 50 µm	(Tripathi and Basu, 2012)

The OH⁻ and PO₄³⁻ groups are responsible for the negativity of the HA surface and Ca^{2+} ions contribute as the positive groups. The process of apatite formation solely depends on negative groups that exist on the HA surface. When the material is incubated in SBF, the positive Ca^{2+} ions from SBF are attracted by the OH^- and PO_4^{3-} ions present on the surface of the HA scaffold. Therefore, the surface gains a positive charge with respect to the surrounding SBF and further attracts the negatively charged OH^- and PO_4^{3-} ions present in the SBF. It leads to the formation of the apatite layer.
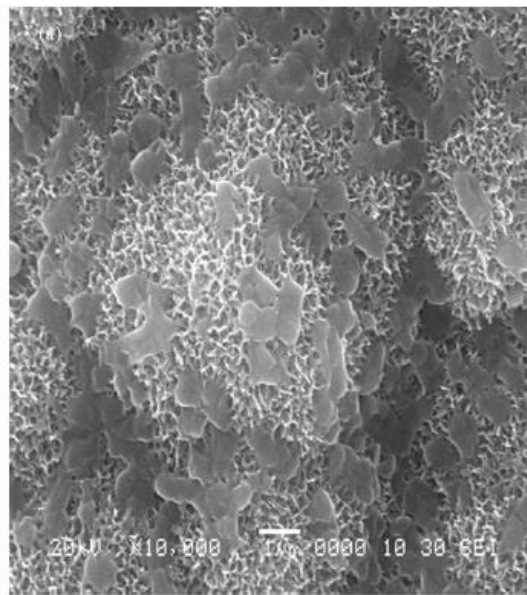
Figure 2.11: SEM image shows the growth of new apatite layer on porous HA scaffold incubated in SBF for 50 days (Chavan et al. 2010).

2.8 Biodegradation of hydroxyapatite scaffolds

Biodegradation is the process induced by the activity of living systems such as microorganisms, cells, when a material breaks down into its simpler constituents which wear away by erosion later, leads to dissolution. Cell-mediated degradation of HA scaffold is concerned with various activities related to cells. When bone cells adhere to the surface of the HA scaffold, can cause an increase in intracellular Ca^{2+} ion concentrations due to the partial dissolution of the Ca-P, resulted in enhancement of cell proliferation that can be established by increased mitogenesis and decrease in

alkaline phosphatase activity. Others suggested that the lower Ca/P ratio degraded faster than the sample with a higher Ca/P ratio. The degradation rate *in vivo* could be controlled to a certain extent by changing the Ca/P ratio of the sample. An ideal bone scaffold should have good mechanical properties and be degradable with the growth of cells and bone tissue (Basu 2017).

2.9 Biogenic hydroxyapatite

Biogenic hydroxyapatite can be defined as HA which is developed through the direct actions of a living organism, may provide a solution to these limitations, via intrinsic properties such as reduced solubility. The significance of extracting HA from natural resources gives future directions to the young scientific community so that HA extracted from biological resources can be used clinically as a valuable biomaterial.

2.10 Interaction of cells and hydroxyapatite scaffold surface

Interaction between cells and HA scaffold surface is mediated through adsorbed proteins on the surface of biomaterials. The protein adsorption kinetics generally depends on the biomaterial's surface properties. The characteristics of the adsorbed protein layer on the biomaterial surface are not static due to the competition among various proteins. Once the protein is adsorbed on the surface, it doesn't need to stick to the surface permanently. It can be desorbed off and other higher affinity proteins can be adsorbed at the same site. Phenomenologically, the first molecule to reach the scaffold surface is water molecules, it forms a water shell on the biomaterial surface. The preferably hydrophilic surface has more affinity towards water molecules, the stability and concentration of the protein layer depend on surface energy, wettability, functional groups present on the surface and texture of the surface (Basu 2017). The process of protein adsorption has been illustrated schematically in Figure 2.12.

Table 2.3: Comparison of mechanical properties and biomineralization study of hydroxyapatite scaffolds

Sources of HA and pore formers	Sintering condition	Porosity (%) and pore architecture	Compressive strength (MPa)	Elastic modulus (GPa)	Biomineralization in SBF	Reference
Commercial HA and poly vinyl butyral (PVB)	1200 °C, 1 h to 48 h	30-70 % and macropore size ranging from 0.093 to 0.42 mm	30-35	-	-	(Liu 1997)
Commercial HA and urea (25 wt%)	1100 °C, 2 h	49-57 % and nearly spherical and distributed homogenously	~ 6-12	-	-	(Albayrak et al. 2016)
	1200 °C, 2 h	35-40 %	~ 10-20	-		
Commercial HA and urea (50 wt%)	1100 °C, 2 h	67 %	~ 2	-		
	1200 °C, 2 h	57 %	~7	-		
Commercial HA and benzoyl peroxide	1350 °C	40 %	30 ± 8	1.4±0.4	-	(Tadic and Epple 2003)
$Ca(NO_3)_2 \cdot 4H_2O$ and $(NH_4)_2 \cdot HPO_4$	1000 °C, 2 h	-	-	-	Full coverage in 30 days, growth of apatite layer in	(Chavan et al. 2010)

					the form of interlinked hemispherical globules	
Cod fish bones	900-1250 °C, 2h	-	--	-	Full coverage in 7 days, clear network of apatite crystals	(Piccirillo et al. 2015)
Sol-gel method using P_2O_5 and $(Ca(NO_3)_2·4H_2O$ as a precursor with PVA and NaCl as pore former	1350 °C, 2 h	63 –76 %	1–1.7	0.15–0.22	Full coverage in 28 days, nucleation and growth of bone-like apatite layer on the bioactive composites	(Eilbagi et al. 2016)
Commercial HA and polyurethane foams	1200 °C, 3 h	85–89 % and interconnectivity of 55.8–79.2%	-	-	Full coverage in 21 days, formation of 3D network of apatite	(Ocampo et al. 2016)
Calcium hydroxide and ortho-phosphoric acid	1300 °C, 3 h	~ 70%	30.2	-	Full coverage in 7 days, cauliflower like morphology of apatite formed	(Oliveira et al. 2009)
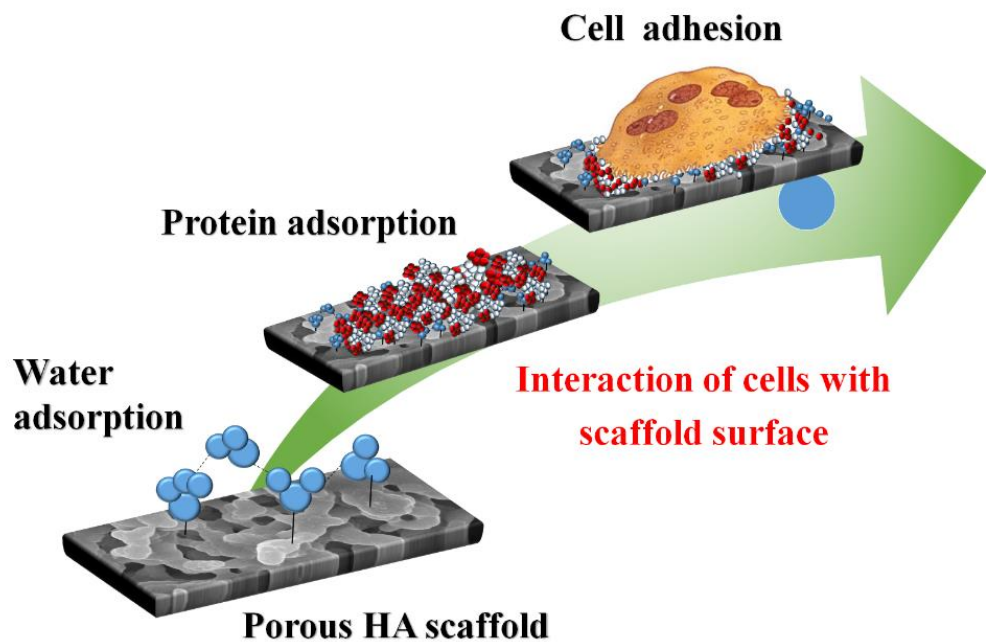
Figure 2.12: A schematic representation of the succession of events before or during the cell and scaffold surface interaction.

2.11 *In vitro* biocompatibility

To assess the biocompatibility of HA porous scaffolds, the *in vitro* approach is adopted by several researchers. The mouse osteoblast precursor cell line (MC3T3-E1), derived from *Musmusculus calvaria* is mostly used for *in vitro* cytotoxicity experiments. Importantly, MC3T3-E1 is a broadly used osteoblast cell line, with a list of additional advantages such as (a) simple maintenance procedure (b) a large number of cells due to their active replication, and (c) relative osteoblast phenotypic stability during the initial phase of culture (Bhaskar et al. 2018).

In summary, Figure 2.13 shows the schematic illustration of various necessary properties of biogenic HA scaffolds to be considered during developing the same. The biocompatible hydroxyapatite scaffolds have grabbed considerable scientific attention and results of which can be seen as the near exponential increase of Scopus indexed scientific articles between 2000 and 2019 (Figure 2.14).
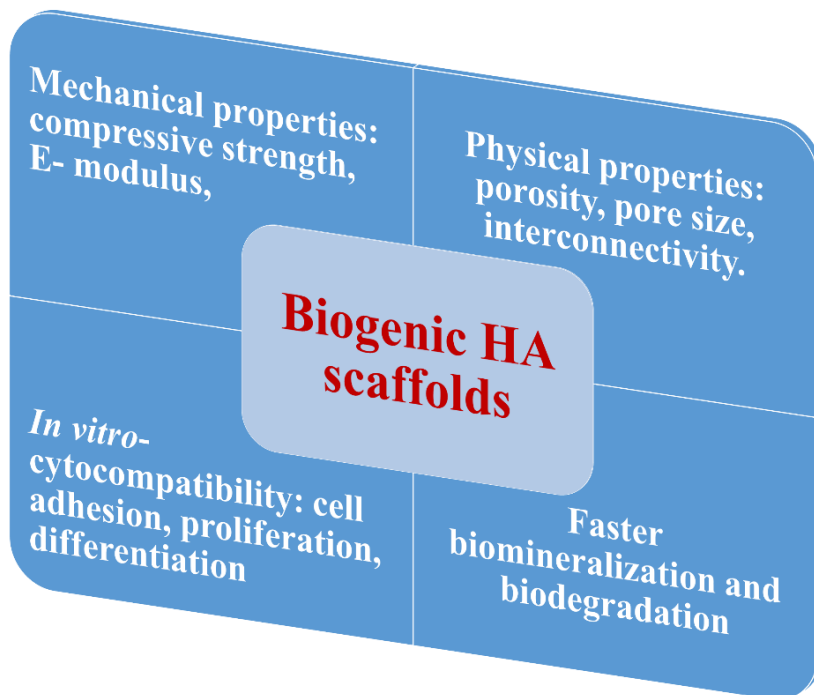
Figure 2.13: Schematic illustration of various necessary properties of biogenic HA scaffolds
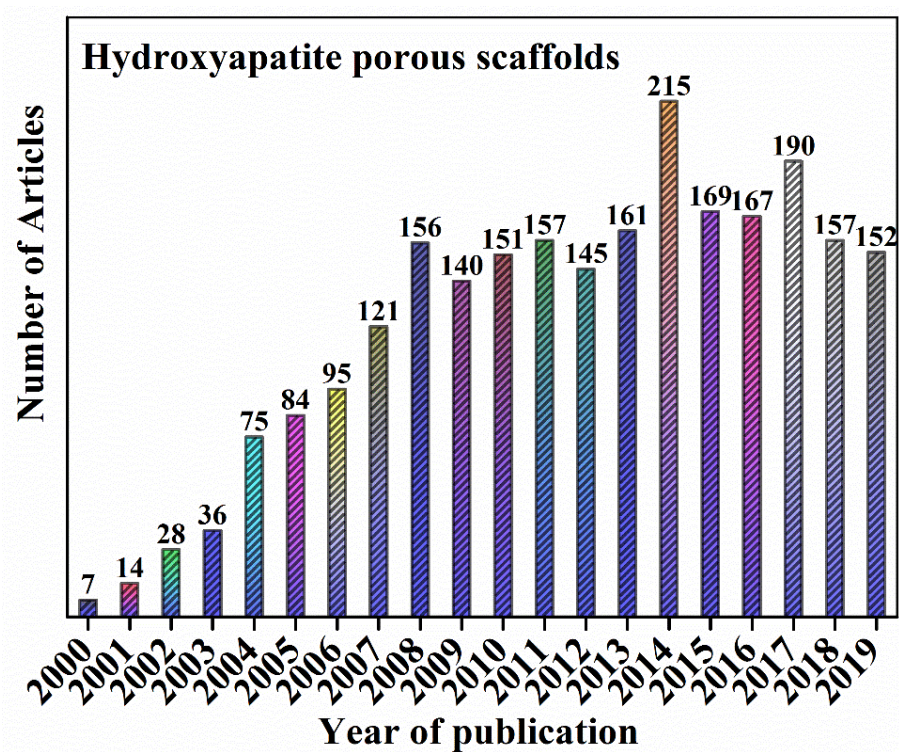
Figure 2.14: The number of Scopus indexed articles published on hydroxyapatite scaffolds for tissue engineering applications between the years 2000 and 2019.

2.12 UV absorbing materials in sunscreen filters

Ultraviolet (UV) irradiation from sunlight is increasing day by day on the earth with the depletion of the ozone layer in the stratosphere. The UV radiation catering into three parts, UV A (320 to 400 nm), UV B (280 to 320 nm), and UV C (200 to 280 nm). UV C does not reach the earth's surface as they are absorbed predominantly by the ozone layer (Oyamada et al. 2008). UV A and UV B are accountable for sunburn or erythema (redness in the skin) and skin disease (Jain and Jain, 2010). Long-time exposure of UV into the epidermis, dermis and hypodermis of the skin leads to wrinkles, roughening, smudge, basal cell cancer and other skin related irritations (Subramaniyan et al. 2013). The use of sunscreens as a protective barrier against skin damage and cancer, by absorbing harmful UVA and UVB rays, is becoming an increasingly important issue. Titanium dioxide (TiO_2) and zinc oxide (ZnO) are active sunscreen filter materials used in most of the sunscreen products available in the market. Although both of them are effective in absorbing the UV radiations, being photocatalytic they generate free radicals like reactive oxygen species (ROS) while irradiating; hence they become harmful to the skin. ROS contain oxygen which can easily reacts with other molecules in a cell. A buildup of reactive oxygen species in cells may cause damage to DNA, RNA, and proteins, and finally end with cell death. ROS are free radicals and highly reactive chemical molecules formed due to the electron acceptability of O_2. Examples of ROS include peroxides, superoxide, hydroxyl radical etc.

Many sunscreens penetrate the skin, which leads to photoallergies, phototoxic reactions and skin irritations. Therefore, there is an urgent need for the development of a safer sunscreen system. It can be achieved by formulations with little penetration into the skin and using biocompatible materials. HA is a calcium phosphate compound, it is a non-toxic material, being the main component of human and animal bones; it has high biocompatibility; because of this, HA is used to make bone and dental implants. Because of its non-toxicity, it would be a very suitable material as a base for sunscreen filters. Unmodified HA, however, does not absorb in the UV range, so it is necessary to modify its structure to obtain a UV-absorbing material.

TiO$_2$ and ZnO are popular inorganic sunscreen agents, their high refractive indices, however, can make the skin look unnaturally white when incorporated into the products. Additionally, their high photocatalytic activity facilitates the generation of reactive oxygen species, which can oxidize and degrade other ingredients in the formulation, raising safety concerns. Commercially available inorganic and organic sunscreen products have active ingredients to absorb UV radiation, namely ZnO and TiO$_2$ nanoparticles (Pal et al. 2020), dioxybenzone, avobenzone, mexoryl, tinosorb, etc. (Qian et al. 2015) Oxide nanoparticles have shortfalls (lack of efficiency) in terms of UV protection and eco-friendliness. ZnO and TiO$_2$ have photocatalytic activity, which results in the formation of free radicals, with prolonged UV irradiation, leads to the formation of harmful reactive oxygen species (ROS). In comparison with physical sunscreens, chemical sunscreens are simpler to use, but associated with demerit like long-term use may trigger unexpected side effects like allergenicity and sensitization (Pal et al. 2020).

According to the literature, TiO$_2$ and ZnO are used in commercial sunscreens, both oxides protect the entire UV range. Further, nanoparticles from TiO$_2$ and ZnO enhance their effectiveness, which leads to improved protection. In parallel, there is a concern about the possible toxicity of the nanoparticles. Both minerals are photo-chemically reactive compounds: "It means under irradiation, they can form free radicals and other reactive species that can cause some of the health problems associated with UV exposure. Fe$_2$O$_3$ and HA doped with metal ions are reported to be promising ultraviolet (UV) absorbing materials, Fe can be chosen as it is potentially less toxic than Mg and other metals (Piccirillo et al. 2014).

Organic filters are generally aromatic compounds with a carbonyl group, such as cinnamates, salicylates, anthranilates, benzophenones, and dibenzoylmethanes (Jain and Jain, 2010), (Antoniou et al. 2008). Organic filters do not protect from a large spectrum of UV radiation. Sunscreen filters with organic active ingredients when it is tested under UVA and UVB radiation experience photochemical changes; hence, in a short time, they will no longer remain as effective as earlier. Also, it has been reported that organic UV sunscreen filters are not photostable (Sayre et al. 2005).

2.13 Doped hydroxyapatite as sunscreen filters

HA is a principal mineral component of hard tissue (bone, teeth), is a highly stable, biocompatible and non-toxic material with its application as a bioceramics material. HA has excellent biocompatibility as it has a similar chemical composition as that of the mineral matrix of the bone, may show good potential as a UV sunscreen filter. It is necessary to invent a compatible sunscreen in all aspects. An effective sunscreen filter should possess two important features namely: (1) absorption of UV radiation and (2) compatibility with skin, no impact on the skin by the formation of reactive species.

In this regard, the processing of sunscreen filters using calcium phosphate can be of attentiveness as it has already shown various biomedical applications. The choice of HA as a sunscreen filter is owing to tuning its property of absorption in the UV region with aid of metal ion incorporation (Pal et al. 2020; Smijs and Pavel 2011). HA doped with Zn, Mn, Cr and Fe were investigated as an active constituent in sunscreen filters, where remarkable UV absorption was noticed with doping of the appropriate amount. Araujo et al. studied the influence of Zn, Fe, Mn and Cr doping on UV absorption of HA; Mn and Fe, in particular, were found to be the most effective (Araujo et al. 2010). Kramer et al. developed iron-substituted HA with no formation of a secondary phase by using an ion-exchange method (Kramer et al. 2013). The contraction in the lattice parameters of HA is attributed to the smaller ionic radius of Mn^{2+}, Fe^{2+}, and Co^{2+} compared to Ca^{2+} (Zilm et al. 2016). Ionic replacement of Ca^{2+} in HA is also associated with the change of crystallinity (Zilm et al. 2016). Further, the doping effect will extend to optical properties such as UV absorption along with tailoring of the bandgap, while an increase in doping concentration results in decreasing bandgap as it depends upon the energy level of dopants in comparison with Ca (Jiménez et al. 2017).

Fe-substituted HA and a minute quantity of hematite absorb the radiation over the entire UV range without releasing any harmful reactive oxygen species (Piccirillo et al. 2014). Iron is considered as a dopant in HA, because it is, potentially less toxic than Mn (Piccirillo et al. 2014) and other transition metals (Zilm et al. 2016). It is necessary to develop phase pure Fe- HA with proper quantification of Fe in order to produce suitable material for sunscreen filter applications with a facile method like ion exchange route. Teixeira et al. reported XRD data of Fe substituted HA together with the mixed

Table 2.4: A summary of different studies revealing the optical band gaps of doped HA

Materials	Doping proportion	Sample name	Optical band gap (eV)	Reference
Tb-doped hydroxyapatite	-	HA (undoped)	5.41	(Jiménez et al. 2017)
	12 weight % of Tb	TbW12	4.38	
Zn^{2+}/ Cu^{2+} doped hydroxyapatite	10 weight % of Zn+Cu	10% Zn/Cu-HA	3.77	(Mariappan et al. 2017)
	50 weight % of Zn+Cu	50% Zn/Cu-HA	3.30	
Ion-doped hydroxyapatite (La-L, Fe-F, Ba-B, Zn-Z) Atomic % (at.%)	La- 2 at.%, Zn- 2 at.%	LZ	5.10	(Helen and Kumar, 2019)
	Ba- 2 at.%, Zn- 2 at.%	BZ	3.88	
	Fe- 2 at.%, Zn- 2 at.%	FZ	3.00	
	La- 5 at.%, Zn- 5 at.%	LZ5	5.16	
	Ba- 5 at.%, Zn- 5 at.%	BZ5	4.89	
	Fe- 5 at.%, Zn- 5 at.%	FZ5	3.14	
Strontium - Erbium co-doping hydroxyapatite	Sr and Er in atomic %	0.35Sr-HA	5.1915	(Mahmood et al. 2020)
		0.35Sr-0.35 Er-HA	4.8835	
		0.35Sr-1.40 Er-HA	3.9084	
Sr-doped hydroxyapatite	Sr in 4.5 atomic %	Sr- HA	5.08	(Moradi and Alvani 2019)
Ti-substituted hydroxyapatite	-	HA (undoped)	> 6	(Tsukada et al. 2011)
	10 atomic % of Ti	Ti-HA	3.65	
$Ca_{9.5}M_{0.5}(PO_4)_6$ $(OH)_2$ where (M= Mn, Co, Ni, Cu)	-	HA (undoped)	5.26	(Eddya et al. 2018)
	M in 5 atomic %	HA-Ni	2.12	
		HA-Cu	2.5	
		HA-Mn	4.5	
		HA-Co	1.76	
Erbium-doped hydroxyapatite	2 atomic %	Er-HA (0.02 M)	4.02	(Alshemary et al. 2015)
	10 atomic %	Er-HA (0.1 M)	4.46	

calcium-iron phosphate; moreover, in all samples, α- Fe_2O_3 (hematite) was also detected. The UV absorption pattern must be from a collective contribution of $Ca_9FeH(PO_4)_7$ and α- Fe_2O_3 (hematite) (Teixeira et al. 2017).

The bandgap is a region in energy with no allowed states. The chemical composition of the materials decides the nature of the density of states versus the energy curve. Impurities can affect the chemical composition of the host material, especially known as dopants, which create allowed shallow states in the bandgap. Shallow states have minimum ionisation energies; and, when the doping concentration becomes high, the dopant states form a band. If the dopant induced band is near to either the conduction or valence band edge resulted in a reduction of the bandgap. Dopants always create more allowed states near the band, hence bandgap decreases. Table 2.4 displays the literature studies showing the reduction in the optical bandgap of doped HA with an increase in doping proportion.

2.14 Natural protection of UV radiation

Natural resources-based sunscreens are more effective than chemical and physical sunscreens as they won't produce free radicals. The outer shell of few marine species also possesses UV absorbing capability, which leads to the discovery of new material as a promising natural sunscreen filter. Therefore, natural sunscreens are getting more and more attention as they are free from adverse effects. Table 2.5 reveals the few natural sources which are explored for UV absorbing proteins.

Table 2.5: A few natural sources of UV absorbing proteins

Plant based (Qian et al. 2015)	Marine resources based (Fernandes et al. 2015)
Corn starch, Helichrysum arenarium (Everlasting flowers), Mulberry fruit extract, Lignin, Carica papaya extracts, Green coffee oil, etc	Mucus and fish lenses contain mycosporine-like amino acids.

A recent development on the UV protection by natural products such as corn starch, helichrysum, carica papaya extracts, arenarium, lignin, mulberry fruit extract, green coffee oil and rosa cardesii has been demonstrated as a replacement for the existing filters (Kim et al. 2017; Qian et al. 2015). Marine based mucus and fish lenses contain

mycosporine-like amino acids, which facilitate the absorption of UV radiations (Fernandes et al. 2015). Mycosporine-like amino acids, namely, porphyra-334, mycosporine-glycine, shinorine, tryptophan, phenylalanine and tyrosine absorb the entire UV range due to the presence of complex amino acid with the central aromatic ring (Hazra et al. 2014). Owing to these excellent properties, these new categories of amino acids can be utilized as essential ingredients in sunscreen products (Fernandes et al. 2015).

The presence of UV absorbing and non-UV absorbing proteins are listed in Table 6.4 from prawn shell/shrimp shell (Ibrahim et al. 1999; Scholz 1961; Hazra et al. 2014). The proteins present in prawn shells are primarily composed of amino acids such as arginine, isoleucine, lysine, histidine, cysteine, valine, threonine, methionine, leucine, phenylalanine, tyrosine, proline, alanine, glycine serine, glutamic acid, aspartic acid and tryptophan (Ibrahim et al. 1999; Scholz 1961). UV absorbing proteins extracted from prawn exoskeleton can be utilise in both polymer coating material as well as in cosmetics to inhibit UV irradiation. Prawn exoskeleton containing chitosan could be used as an effective ingredient in anti-aging skincare products because of its antimicrobial and skin regeneration properties (Hamed et al. 2016).

Table 2.6: Details of the presence of proteins in shrimp/prawn shells

Sources	Proteins	UV absorbance	Reference
Shrimp	Threonine ($C_4H_9NO_3$), Valine ($C_5H_{11}NO_2$), Methionine ($C_5H_{11}NO_2S$), Cystine ($C_6H_{12}N_2O_4S_2$), Leucine ($C_6H_{13}NO_2$), Isoleucine ($C_6H_{13}NO_2$), Lysine ($C_6H_{14}N_2O_2$), Phenylalanine ($C_9H_{11}NO_2$), Tyrosine ($C_9H_{11}NO_3$), Histidine ($C_6H_9N_3O_2$), Proline ($C_5H_9NO_2$), Alanine ($C_3H_7NO_2$), Glycine ($C_2H_5NO_2$), Arginine ($C_6H_{14}N_4O_2$), Serine ($C_3H_7NO_3$), Glutamic acid ($C_5H_9NO_4$), Aspartic acid ($C_4H_7NO_4$)	Phenylalanine Tyrosine,	Ibrahim et al. 1999; Hazra et al. 2014
Shrimp	Tryptophan ($C_{11}H_{12}N_2O_2$), Arginine ($C_6H_{14}N_4O_2$), Lysine ($C_6H_{14}N_2O_2$), Histidine ($C_6H_9N_3O_2$)	Tryptophan	Scholz 1961; Hazra et al. 2014

2.15 Structure of prawn exoskeleton

Prawn consisting of near 55-65 % by weight of edible and the remaining 35-45 % is the bio-waste, used as animal feed mix, fertilizer and source of chitin/chitosan (Hansen and Illanes 1994). Prawn exoskeleton/shells contain (a) calcite (30-50 %), (b) nitrogen-containing polysaccharide, named as α-chitin (20-30%), and (c) proteins (30-40 %) along with trace amounts of calcium phosphates, Mg and other elements (Hansen and Illanes 1994; Knorr 1984). The structure of prawn shells is composed of multilayer stacking of chitin–protein fibers, which are periodically arranged in the form of a twisted woven structure to build a composite of chitin-protein (Raabe et al. 2005). The spacing between the fibers is filled with microscopic bio-minerals and proteins. The biominerals are largely in the form of crystalline calcium carbonate (calcite/$CaCO_3$), but amorphous calcium carbonate may also exist depending on the molt cycle and species (Raabe et al. 2005).

2.16 Scope and objectives of the study

<u>Scope</u>:

In the tissue engineering field, it is required to design new biomaterials with suitable biological and mechanical properties and growth factors for actuating the bone regeneration process for the human body. Scaffolds based tissue engineering pivots on an efficient combination of viable cells, biomolecules and scaffold to promote repair and/or regeneration of bone tissues. Extraction/synthesis of nature-derived biomaterial especially hydroxyapatite from abundant dead marine resources offers new dimensions for the evolution of novel medical products that may be used for biomedical applications, including tissue engineering.

HA has its appropriate properties in multiple applications, which offers a new direction to invent its capability in biocompatible UV absorbing materials. Titanium dioxide and zinc oxide are recurrently used in sunscreens as physical sun blockers, but in the form of nanoparticles, these materials deliver skin-damaging effects by generating reactive oxygen species (ROS). Therefore, there is an urgent need of

developing a biocompatible sunscreen material. Fe-substituted hydroxyapatite can absorb the radiation over the entire UV range without releasing any harmful reactive oxygen species, could be a suitable material for sunscreen filter applications. Prawn exoskeleton/shell as a new class of naturally occurring composite contains UV absorbing proteins. UV absorbing proteins from prawn shells can be promising constituents in sunscreen filters for cosmetics, textiles, food, pharmaceuticals and biodegradable packaging products.

Objectives:

- Collection of different dead marine benthos bio-waste from the seashore of Dakshina Kannada as the sources of $CaCO_3$.

- To synthesize and characterize biogenic hydroxyapatite powder via a wet chemical precipitation method.

- To fabricate and characterize dense and porous hydroxyapatite scaffolds with tailoring mechanical and physical properties.

- To understand the bone-bonding ability of biogenic hydroxyapatite, biomineralization study in simulated body fluid and to quantify cyto-compatibility by *in vitro* study using mouse osteoblasts cells.

- To develop and characterize hydroxyapatite-based UV absorbable sunscreen filter material by Fe incorporation through the ion-exchange procedure.

- To explore the prawn shell as a natural impermeable layer of UV protection and identify the presence of constituents responsible for UV absorption.

CHAPTER 3

EXPERIMENTAL PROCEDURE

3. 1 Collection of calcium-rich marine benthos bio-waste

Marine benthos bio-waste was collected from Arabian seashore of Dakshina Kannada, Figure 3.1 shows the optical images of eight different marine benthos; a) *Austromegabalanus psittacus* (AMBP), b) star fish (SF) (*Asteroidea*), c) sea urchin (SU) (*Echinoidea*) d) cuttlefish bone (CF) (*Sepia officinalis*) e) goose barnacle (GB) (*Lepas anserifera*), f) sea crab (SC) (*Neptunus sanguinolentus*), g) prawn (PR) (*Fenneropenaeus indicus*) and h) sand dollar (SD) (*Clypeaster humilis*). Respective marine species names and their phylum with a form of $CaCO_3$ are listed in Table 3.1.

Table 3.1: Details of collected calcium rich marine benthos

Sl. No	Marine benthos	Phylum	Aragonite / Calcite ($CaCO_3$)
1	Cuttlefish bone	Mollusca	Aragonite
2	Starfish	Echinodermata	Calcite
3	Sea urchin	Echinodermata	Calcite
4	Prawn shell	Arthropoda	Calcite
5	AMBP	Arthropoda	Aragonite
6	Goose barnacle	Arthropoda	Aragonite
7	Crab	Arthropoda	Calcite
8	Sand dollar	Echinodermata	Calcite

3.2 Synthesis of hydroxyapatite

Collected marine benthos biowaste (shells/exoskeleton) were cleaned with hot water and dried properly, which was followed by manually grinding with agate mortar and pestle to obtain a fine powder of calcite/aragonite ($CaCO_3$). $CaCO_3$ was calcined at 900 °C for 12 hr to obtain a milky white coloured calcium oxide (CaO). A facile wet chemical precipitation method was adopted to synthesize HA (Figure 3.2 and equations 3.1-3.3). Calcium oxide was treated with distilled water in a beaker and stirred

continuously with a magnetic stirrer. Meanwhile, drop-wise addition of ortho-phosphoric acid (85 % H_3PO_4) was followed to advance the reaction. The hot plate was kept at 80 ºC for 2 hours to complete the chemical reaction. After completion of the process, a white thick solution of hydroxyapatite was precipitated; it was dried at 100 ºC in a hot air oven to obtain moisture free HA powder. To synthesize HA from calcite/aragonite, the reactions 3.1, 3.2 and 3.3 are involved (Santhosh et al. 2012).
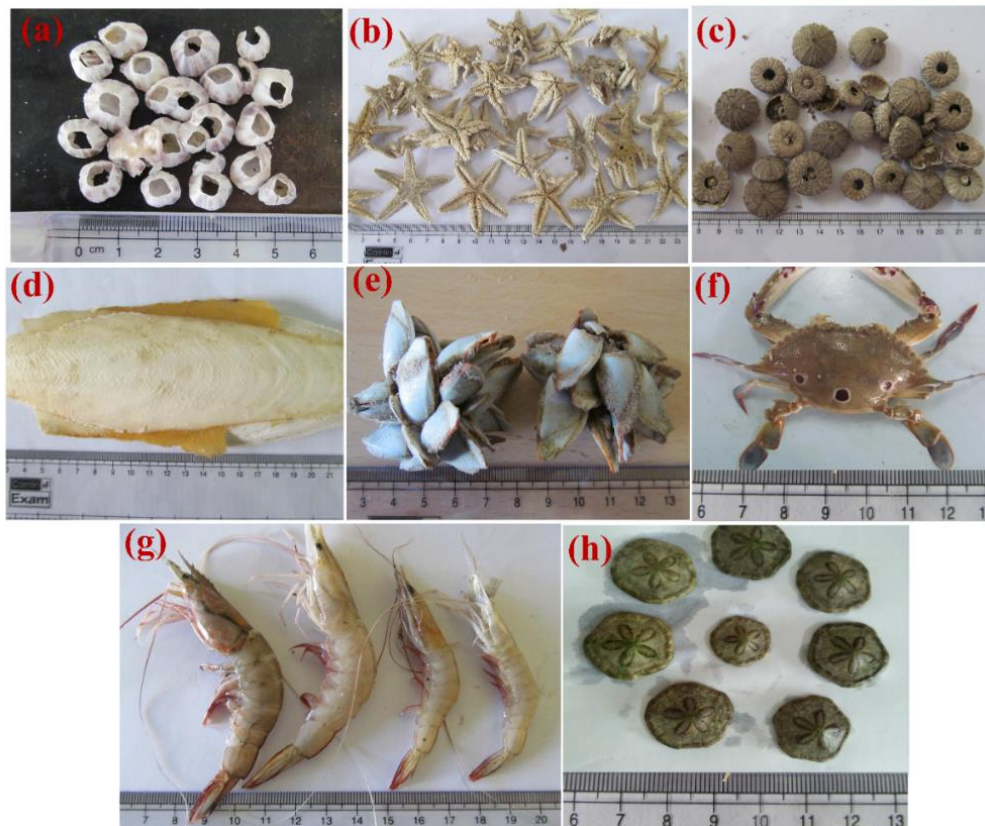
Figure 3.1: Optical images of calcium rich marine benthos namely a) *Austromegabalanus psittacus* (AMBP), b) star fish (*Asteroidea*), c) sea urchin (*Echinoidea*) d) cuttlefish bone (*Sepia officinalis*) e) goose barnacle (*Lepas anserifera*), f) sea crab (*Neptunus Sanguinolentus*), g) prawn (*Fenneropenaeus indicus*) and h) sand dollar (*Clypeaster humilis*).

$$CaCO_3 = CaO + CO_2 \ldots\ldots\ldots\ldots\ldots\ldots (3.1)$$

$$CaO + H_2O = Ca(OH)_2 \ldots\ldots\ldots\ldots\ldots (3.2)$$

$$10Ca(OH)_2 + 6H_3PO_4 = Ca_{10}(PO_4)_6(OH)_2 + 18H_2O\ldots\ldots\ldots\ldots (3.3)$$
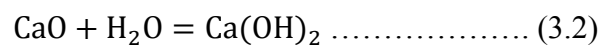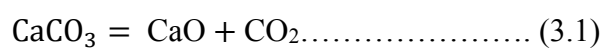
3.3 Development of dense and porous hydroxyapatite

Figure. 3.2 shows the schematic representation of processes involved in the development of dense and porous HA scaffolds from marine benthos. A weighed amount of dried HA powder was placed in the cleaned die and plunger, maintaining the cylindrical body of ratio of length/diameter (L/D) equal to 1.5. HA powder was compacted using uni-axial hydraulic pressing machine with a load of 8 KN and a holding time of 1 minute to get a green compact. The green compact was subjected to solid state sintering at 1100 °C with a 5 °C/min heating rate and holding for two hours in the high temperature programmable tubular furnace to get sintered dense HA pellets.
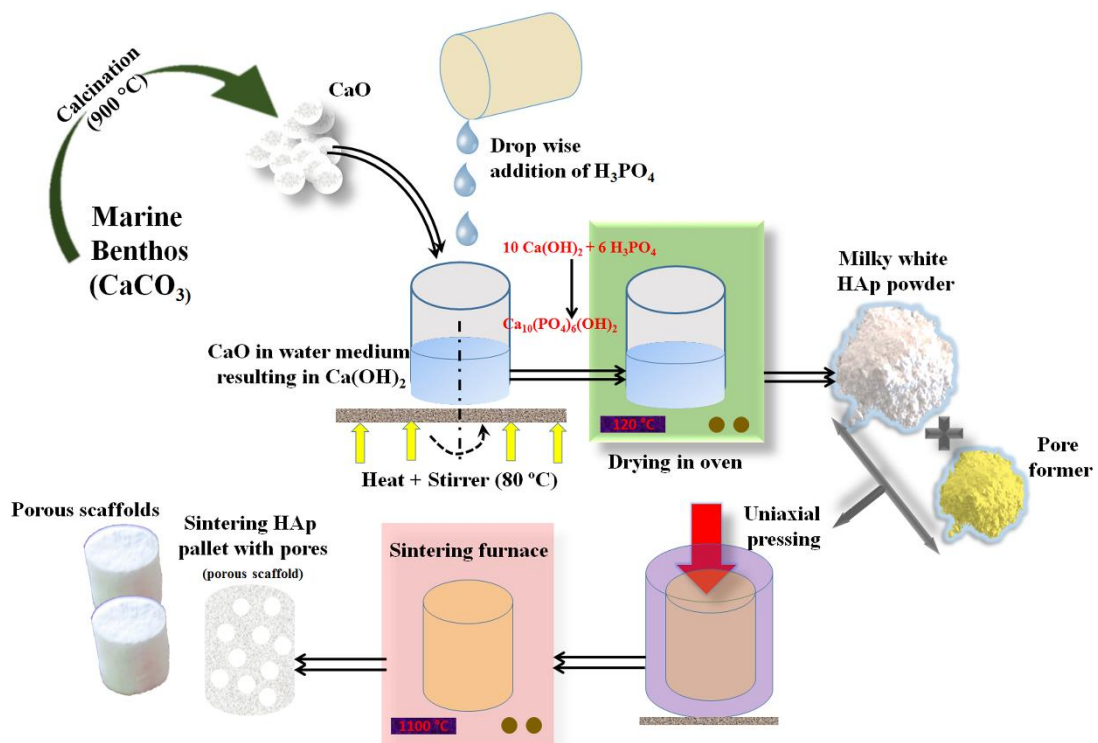
Figure 3.2: Schematic representing the development of biogenically synthesized hydroxyapatite scaffolds

To prepare porous scaffolds, HA powder was uniformly mixed with different weight percentages (10, 20, 30, 40 and 50 %) of organic pore formers like wax, wheat flour and milk powder using an agate mortar and pestle. Like dense HA, similar procedures of green compaction and solid-state sintering were followed to develop HA

porous scaffolds. During sintering at high temperature (1100 °C), all organic pore formers were vaporised and left behind the interconnected pore architecture of HA scaffolds (Figure 3.2).

3.4 Characterization of hydroxyapatite powder

The raw aragonite ($CaCO_3$) powder was analysed using differential scanning calorimetry (DSC, NETZSCH DSC 404 F1, Germany) to determine suitable calcination temperature. The crystalline phases present in aragonite, calcined aragonite and hydroxyapatite powder (before and after sintering) were investigated by using X-ray diffraction (XRD, RIGAKU Miniflex 600, Japan). XRD data were collected at room temperature over the 2θ range of 10°- 90° with a scan rate of 1 °/min. The calculation of crystallite size from Scherrer's method is a well-known method that uses X-ray diffraction patterns to predict the size of crystallites based on the width of the diffraction peak. But Scherrer's formula under- estimates or provides only a lower bound to the crystallite size because it has not taken account of peak broadening resulting from other important factors such as inhomogeneous strain and instrumental effects. Generally, the X-ray diffraction peak broadening is due to the instrumental broadening, broadening due to crystallite size and lattice strain present in the material. The contributions of each of these effects are convoluted causing an overall broadening of the diffraction peaks. Before estimating the crystallite size, it is necessary to correct the instrumental effect. The instrumental corrected broadening β $_{hkl}$ corresponding to the diffraction peak of HA was estimated using the equation

$$\beta_{hkl} = [(\beta_{hkl\,(meaured)})^2 - (\beta_{hkl\,(Instrumental)})^2]^{1/2} \ldots\ldots\ldots(3.4)$$

Fourier transform infrared spectrometry (FTIR, JASCO FTIR -4200, Japan) was carried out to determine the presence of chemical bonds in hydroxyapatite. Raman spectroscopy (HORIBA JOBIN YVON) was used to identify the presence of vibrational modes in hydroxyapatite from laser light of wavelength 530 nm. Transmission electron microscope (TEM, JEOL, JEM-2100, Japan) and scanning electron microscopy (SEM, JEOL model JSM 6380, Japan) were used to analyse surface morphology and microstructure. To determine the chemical state of elements

and their composition present in hydroxyapatite, X-ray photoelectron spectroscopy (XPS; PHI 5000 VersaprobeII, Philippines) was performed.

3.5 Characterization of porous hydroxyapatite scaffold

3.5.1 Thermal analysis

Thermal behaviour of hydroxyapatite blended with three different pore formers like wax, wheat flour and milk powder was subjected to thermo-gravimetric analysis (TGA) (PerkinElmer, Thermo-gravimetric Analyzer 4000, New Jersey). TGA was performed in a nitrogen atmosphere at a heating rate of 10 $^{\circ}$C/min with a scanning temperature of 30 $^{\circ}$C to 900 $^{\circ}$C.

3.5.2 Physical and mechanical properties

The physical and mechanical properties of porous sintered hydroxyapatite scaffolds were studied. The density measurement kit (CONTECH, India) was used to measure apparent density (A.D.), bulk density (B.D.) and apparent porosity (% of the open pore) (A.P.) by using equations 3.5, 3.6 and 3.7 respectively. The A.D. of hydroxyapatite scaffold was accurately measured with the help of He gas Pycnometer (QUANTACHROME CORPORATION Ultrapyc 1200e, USA), based on the Archimedes principle of gas displacement. Before measurement, the porous samples were kept in a desiccator for at least a period of 6 hrs. The density measurements in the pycnometer container cell were performed after purging He gas for 10 min with a controlled flow rate. The percentage of closed porosity was estimated from the measured bulk density and theoretical density. The percentage of closed porosity present in the material was determined from equation 3.8. Mechanical properties, like compression strength and compressive modulus, were determined by a compression test conducted with a universal testing machine (UTM, SHIMADZU AG- X plus 100 KN, Japan).

Physical properties calculation formulas:

$$\text{Apparent density} \quad A.D. = D/(D - I) \ldots\ldots\ldots\ldots\ldots.(3.5)$$

$$\text{Bulk density} \quad B.D. = D(S - I) \ldots\ldots\ldots\ldots\ldots (3.6)$$

$$\text{Apparent porosity} \quad A.P. = \left(\frac{S-D}{S-I}\right) \times 100 \ldots\ldots\ldots\ldots...(3.7)$$

$$\text{Closed porosity} (\%) = \left(1 - \frac{Bulk\ density}{Theoretical\ density}\right) \times 100 \ldots\ldots\ldots(3.8)$$

Where D= Dry weight, I= Immersed weight, S= Submerged weight.

3.5.3 Micro-computed tomography (micro-CT)

Micro-computed tomography (micro-CT) of sintered hydroxyapatite scaffolds were carried out using Versa XRM-500 (Xradia, Zeiss, Jena, Germany). The energy of the X-ray source was fixed at 120 kV for each measurement. The 4X objective with 1.2 s to 1.4 s exposure time was used for image acquisition and keeping the voxel size was set ~2.5. LE5 filter was employed to get the ideal transmission range of at least 25–35 %. A total 2501 number of 2D projection images were acquired with 360° rotation of the sample. The 3D tomogram was reconstructed from the 2D projections using XMReconstructor software (Xradia, Zeiss, Jena, Germany). Image processing and analysis of the tomogram were performed with Avizo Fire 9.4, FEI, France. First, the histogram equalisation of 3D images was carried out using the 'match contrast' module. A median filter was used for noise reduction of the scanned tomogram. The binarization of images was performed using the watershed module in segmentation tools. Subsequently, the interactive threshold was applied to the binary image. The threshold value was adjusted to create a mask manually to cover the region of interest (ROI). Pore volume fraction was obtained by subtracting the selected pore material from the mask. Then, label analysis was carried out to analyse the distribution and size of connected and separated objects.

3.6 *In vitro* biomineralization, biodegradation and biocompatibility

3.6.1 Biomineralization

The steps to prepare the SBF are as follows:

- 500 ml of distilled water was taken into a one litter polyethylene bottle, and the bottle was covered with a watch glass.
- The bottle was stirred with a magnetic stirrer and one by one reagent in the order as listed in Table 3.2 were dissolved (One after the former reagent was completely dissolved).
- The temperature of the solution was adjusted to 36.5 $^\circ$C with a water bath and a pH of the solution at pH 7.4. The solution was stirred continuously and 1 N HCl solution was titrated to maintain pH.
- The total volume of the solution was adjusted to one liter by adding distilled water and stored the prepared SBF in a refrigerator at 5-10℃.

Table 3.2: List of SBF solution reagents (pH 7.40, 1L), (Kokubo and Takadama 2006)

Order	Reagent	Amount
1	NaCl	7.996 g
2	$NaHCO_3$	0.350 g
3	KCl	0.224 g
4	$K_2HPO_4\ 3H_2O$	0.228 g
5	$MgCl_2\ 6H_2O$	0.305 g
6	1M- HCl	40 mL
7	$CaCl_2$	0.278 g
8	Na_2SO_4	0.071 g
9	$(CH_2OH)_3CNH_2$	6.057 g

In order to carry out the biomineralization study, porous HA scaffolds from cuttlefish bone with wheat flour and milk powder as pore formers were chosen. The reason to select both of them was their better physical and mechanical properties. The study of apatite nucleation on the sintered porous scaffold was observed with respect to incubation time in the SBF medium, which was kept in an incubator experimental chamber with a controlled atmosphere. SBF solution was prepared at a pH level of 7.4.

The porous scaffold was kept in SBF for 1 h, 6 h, 12 h, 24 h, 72 h and 168 h at 37 °C to observe the formation of apatite on its surface with continuous monitoring pH of the SBF solution. The growth of new apatite on the porous scaffold was then studied by SEM. Further, the crystalline phase of new apatite on the porous scaffold was also studied by XRD analysis.

3.6.2 Biodegradation

The biodegradability behaviour of porous HA scaffolds in a Tris-HCl buffer solution with respect to incubation time was investigated. 0.05 M Tris-HCl buffer solution was prepared from tris(hydroxymethyl)aminomethane (Tris) and distilled water. The pH of the solution was maintained ~ 7.4 at 37 °C by adding 1 M HCl. After different time points 1 h, 6 h, 12 h, 1 day, 3 days, 5 days and 7 days, scaffolds were removed and dried. The weight loss of scaffolds was calculated from equation 3.9. Biodegradability was correlated with the weight loss of the scaffolds.

$$\text{weight loss (\%)} = \left(\frac{(w_0 - w_t)}{w_0} \right) * 100 \ldots\ldots\ldots\ldots(3.9)$$

w_0 – Scaffold's initial weight,

w_t – Scaffold's final weight after soaking in Tris-HCl solution at different time points.

3.6.3 Wettability test

Wettability (DI water) of the scaffold surface was determined by the pendant drop (PD) method in a contact angle goniometer (OCA 15EC, Dataphysics®, Germany). Four samples were chosen for this study namely non-biogenic HA without pore former, biogenic HA without pore former, HA with wheat flour and HA with milk powder as pore formers. Here, synthetic HA was purchased from Nano Tech. Lab and named as non-biogenic HA.

3.6.4 *In vitro* cytocompatibility

The *in vitro* cytocompatibility of hydroxyapatite scaffolds with and without pore formers were analysed using the mouse osteoblast precursor cell line (MC3T3-E1), derived from Mus musculus calvaria. MC3T3-E1 cell line was selected due to its behavior similar to the primary calvarial osteoblasts. The cell line is widely used to check the primary cytocompatibility of a material. Five samples were chosen for the study namely glass coverslips (control), non-biogenic HA without pore former, biogenic HA without pore former, HA with wheat flour and HA with milk powder pore former. On samples, the cells were revived from cryo-preserved stock in tissue culture graded T-25 flask (Eppendorf, Germany) with complete growth media. The composition of growth media is made of α-Modified Eagle's medium (α-MEM; Sigma Aldrich, India), 15% (v/v) fetal bovine serum (FBS; Gibco), 100 mg/l each of streptomycin sulphate and penicillin G sodium salt (HiMedia). The osteoblast cells were incubated in an incubator maintained with a temperature of 37 °C, 95 % humidity and 5 % CO_2 atmosphere in an incubator (Sanyo, MCO-18AC, USA). The cells were fed with new culture media every 3 days (Bhaskar et al. 2018). After reaching 80-90 % confluency, the cells were taken out from the T-75 flask using 0.05 % trypsin-EDTA (Gibco, India). The cells were seeded onto the samples at 3×10^3 cells/ml to perform cell culture experiments (Bhaskar et al. 2018).

3.6.5 Cell proliferation

The osteoblast viability at 3, 5 and 7 days of culture was examined using the MTT assay (3(4,5-dimethylthiazol-2-yl)-2,5- diphenyltetrazolium bromide, Sigma-Aldrich, India). 24 well plates were used to culture the cells at a density of nearly 3×10^3 osteoblast cells/well. On the experiment day, the culture media from each well was aspirated and the glass coverslips (control), non-biogenic HA without pore former, biogenic HA without pore former, HA with wheat flour and HA with milk powder pore former were washed two times with phosphate buffer solution (PBS). Freshly prepared 10 % MTT solution was added at different time points 3, 5 and 7 days. The osteoblast cells on samples were incubated with 10 % MTT solution for 4 hours at 37 °C. The formazan crystals were then solubilised in 200 µL dimethyl sulfoxide (DMSO) after

the unreacted MTT was removed. The optical density (OD) of solubilised formazan was measured spectrophotometrically in an ELISA microplate reader (iMark, Biorad laboratories) at 595 nm. The percentage viability was computed as per the following equation 3.10.

$$\% \text{ cell viability} = \frac{OD \text{ of the sample}}{OD \text{ of the control}} \times 100 \ldots\ldots\ldots\ldots (3.10)$$

3.6.6 Cell morphology

To examine the cell morphology on HA scaffolds, mouse osteoblast cells (MC3T3-E1) were plated in 24 well plates (5×10^3 cells/well) for 24 h of incubation time. Glass coverslip was taken as a control for all cell culture experiments. At 3, 5 and 7 days of culture, the cells were washed three times with PBS to eliminate unattached cells. A subsequent fixation was done using 4 % paraformaldehyde (PFA; SD Fine-Chem Limited, India) in PBS for 30 min at ambient temperature. The cells were washed with 1X PBS and permeabilized with 0.1 % Triton-X in PBS for 5−10 min. To prevent non-specific binding of dye, the cells were blocked with 1 % bovine serum albumin (BSA) for one hour after a two-time wash with PBS. Cells were immunostained for 30 min with Hoechst stain 33342 (Life technologies, India) and Rhodamine Phalloidin (Life technologies, India) to observe nuclei and actin filaments, respectively. The morphological and phenotypical behaviour of cells were observed in the fluorescence microscope (Nikon LV 100D, Japan). ImageJ software was used to determine the number of cells from microscopic fields as quantitative analysis.

The comparison of cell viability on each time point on non-biogenic HA without pore former, biogenic HA without pore former, HA with wheat flour and HA with milk powder pore former were carried out using SPSS-16.0 (IBM, USA). In order to perform statistical analysis, each experiment was conducted 3 times. Cell viability analysis and cell counts on specimens were carried out using one-way ANOVA, which was followed by a post hoc Tukey test. A value of $P < 0.05$ was considered statistically significant. In cell counts, "*" denotes the statistically significant difference ($P < 0.05$) from the control at different points 3, 5 and 7 days of culture.

3.7 Fe incorporated HA

A facile ion exchange procedure (Kramer et al. 2013) was adopted for Fe incorporation, while an equal amount of cuttlefish bone based hydroxyapatite was treated with 0.01, 0.02, 0.03, 0.04 and 0.05 M of $FeCl_3$ solution. Primarily $FeCl_3$ solution was prepared with the respective quantity ranging from 0.01 M to 0.05 M in 200 ml of distilled water and an equal amount of hydroxyapatite (1 g) was added in continuous stirring conditions for 1 hour at room temperature. It was then filtered and washed by distilled water, which was followed by oven drying for 24 hours to obtain brownish Fe incorporated HA powder (Figure 3.3). The intensity of color increases as $FeCl_3$ concentration in solution increases (Figure 5. 1(a)). The obtained Fe-HA powders are labeled as 0.01 M, 0.02 M, 0.03 M, 0.04 M and 0.05 M Fe-HA according to the concentration of $FeCl_3$ solutions (Kramer et al. 2013).

Figure 3.3: Schematic representation of the procedure for the Fe incorporation in hydroxyapatite

The crystalline phase of Fe-HA powder was investigated using an X-ray diffractometer (XRD, RIGAKU Miniflex 600). The Fourier transform infrared spectrometry (FTIR) (JASCO FTIR -4200, JAPAN), spectra were taken at an average

of 32 scans and a resolution of 2 cm^{-1} in the wavenumber range 400 - 4000 cm^{-1}. To examine the vibrational mode of characteristic bond present in doped HA, Raman spectroscopy (Labram HR800 Evolution, Japan) was performed in the wavenumber range of 400-1200 cm^{-1}. Scanning electron microscopy (SEM, JEOL model JSM 6380 system) was used to reveal the morphological changes of Fe-HA powders. Elemental analysis using the energy-dispersive X-ray spectroscopy (EDS) and X-ray photoelectron spectroscopy (XPS; PHI 5000 VersaprobeII, Philippines) were carried out to identify the elemental composition and their chemical states. The surface area of undoped HA and Fe doped HA powders were measured by Brunauer-Emmett-Teller analyser (BET, SMART SORB 92/93). Average particle size was calculated using the following equation 3.11 by assuming particles are spherical shaped

$$D_{BET} = \frac{6000}{(S_{BET}) \times d_{th}} \dots\dots\dots\dots\dots\dots\dots (3.11)$$

where D_{BET} is average particle size, S_{BET} is surface area and d_{th} is the theoretical density (Tok et al. 2004). The absorption spectrum data was obtained by UV-vis spectroscopy (UV-vis, Cary 5000) in the wavelength range of 350 to 800 nm with a step size of 1 nm. The absorption data of HA and Fe-HA were compared to recognise the effect of doping and its suitability as a UV-absorbing sunscreen filter. The optical band gap was calculated using Tauc's plot.

To study the electronic structure of hydroxyapatite (HA) and Fe doped hydroxyapatite (Fe-HA), density functional theory (DFT) calculations using Vienna Ab-initio Simulation Package (VASP) was employed (Kresse and Furthmüller 1996). Generalized Gradient Approximation (GGA) of Perdew-Burke-Ernzerhof (PBE) parameterization was used to evaluate the electronic exchange and correlation potential (Perdew and Wang 1992). GGA of the exchange-correlation functional was augmented by a Hund exchange (J) term and a Hubbard Coulomb (U) term for the Fe atom, considering J = 1 eV and U = 4 (Perdew et al. 1996). A large cut-off (400 eV) for the plane-wave basis has been considered to obtain an accurate result. The Monkhorst-Pack scheme k-points of 2X2X2 were used to sample the Brillouin zone in all the calculations. The Hellmann-Feynman method was used to estimate the forces on atoms and subsequently, a conjugate-gradient method was used to relax the atomic position as

well as the shape and volume of the unit cells self consistently until the force on each atom reduced to 0.01 eV/Å.

3.8 Exploration of prawn exoskeleton

The Arabian sea inhabitant prawn (*Fenneropenaeus indicus)* shell was collected from the market, as an abundantly accessible inedible material. Prawn shells were cleaned with hot water and dried overnight in a hot air oven at 100 $^{\circ}$C. Cleaned shells were subjected to a sequence of analyses to identify the structural and elemental features of inorganic and organic constituents present in prawn shells. Scanning electron microscopy (SEM, JEOL model JSM 6380 system) was used for morphological assessment and elemental investigations using energy-dispersive X-ray spectroscopy (EDS). The crystalline phase of calcite and α-chitin were investigated using X-ray diffractometer (XRD, RIGAKU Miniflex 600). Fourier transform infrared spectrometry (FTIR, JASCO FTIR -4200, JAPAN) was carried out under the classic ATR technique to identify characteristic bands of organic and inorganic molecules. The thermal behaviour of prawn shells was subjected to thermogravimetric analysis (Perkin Elmer, Thermo-gravimetric Analyser TGA 4000, New Jersey) to understand the weight loss behaviour as a function of temperature. X-ray photoelectron spectroscopic analysis (XPS; PHI 5000 Versaprobe II, Philippines) was used to determine the chemical state of elements and their composition. As the prawn shell is a natural composite made of multiple components, the complex XPS spectra of individual elements are fitted into a possible number of peaks. The UV visible spectroscopic analysis (UV-vis, Cary 5000) of as-collected and annealed shells at 500, 600 and 900 $^{\circ}$C in a muffle furnace for 4 hours was performed with covering the range of 200 to 800 nm with a step size of 1 nm.

Page left intentionally blank

CHAPTER 4

Biogenic synthesis approach of hydroxyapatite from marine benthos biowaste

Aragonite/calcite ($CaCO_3$) was collected from 8 marine benthos namely, *Austromegabalanus psittacus* (AMBP), star fish (*Asteroidea*), sea urchin (*Echinoidea*), cuttlefish bone (*Sepia officinalis*), goose barnacle (*Lepas anserifera*), sea crab (*Neptunus Sanguinolentus*), prawn (*Fenneropenaeus indicus*) and sand dollar (*Clypeaster humilis*). Biogenic HA was synthesized by using the wet chemical precipitation method. Porous HA scaffolds were prepared by using organic pore formers namely wheat flour, milk powder and wax. Structural, morphological, elemental analysis was carried out to examine the HA. The study of physical and mechanical properties HA scaffolds followed by biomineralization, biodegradation and cytocompatibility of biogenic HA scaffold was described.

4.1 Biogenic synthesis approach

4.1.1 Structural, morphological, physical and mechanical assessment of hydroxyapatite

The X-ray diffraction (XRD) pattern of $CaCO_3$ and CaO from *Austromegabalanus psittacus* (AMBP), star fish (*Asteroidea*), sea urchin (*Echinoidea*), cuttlefish bone (*Sepia officinalis*), goose barnacle (*Lepas anserifera*), sea crab (*Neptunus Sanguinolentus*), prawn (*Fenneropenaeus indicus*) and sand dollar (*Clypeaster humilis*) is shown in Figure 4.1. In Figure 4.1(a), intense peaks were indexed, which were well matched to $CaCO_3$. XRD pattern of cuttlefish (CF) bone based raw powder confirmed the $CaCO_3$, which is in the form of aragonite with reference to ICDD: 00-041-1475. The remaining 7 samples namely AMBP, SF, SU, GB, SC, PR and SD were found to be calcite form of $CaCO_3$ with reference to ICDD: 00-047-1743. Interestingly, the prawn shell and sea crab's raw powders XRD pattern reveals the existence of α-chitin along with calcite. Peak positions of α-chitin with their corresponding planes are 19.4° (110), 21.2° (120) and 23.7° (130) (Jang et al. 2004). Similarly, in sea crab also α-chitin phase was identified. Aragonite/calcite from all 8

samples was converted to pure calcium oxide (CaO) through calcination at 900 °C. The calcination temperature is obtained from DSC analysis (Figure A-I, (Appendix)) of aragonite/ calcite present in all 8 samples. XRD pattern of CaO from 8 samples is shown in Figure 4.1(b) with ICDD: 00-037-1497.
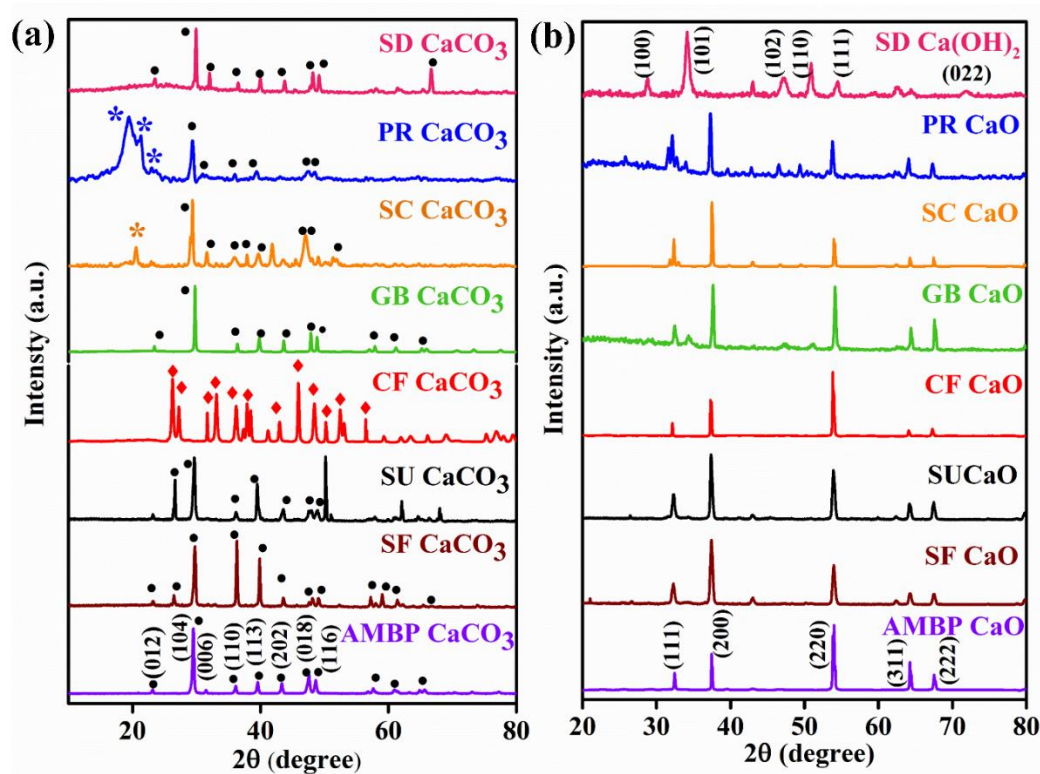
Figure 4.1: XRD pattern of (a) aragonite/calcite ($CaCO_3$) (●: calcite, ♦: aragonite, *: α-chitin) and (b) CaO (calcination at 900 °C)

X-ray diffraction patterns of the as-synthesised and sintered HA are shown in Figure 4.2. Crystalline phases in XRD pattern are indexed (ICDD: 01-074-0565), peaks of as-synthesised HA (Figure 4.2 (a)) and sintered HA (Figure 4.2 (b)) are well matched with standard ICDD peaks. In as-synthesised HA, there was a coexistence of secondary phase $CaHPO_4$ (ICDD:01-070-1425) along with HA. No secondary phase (after sintering at 1100 °C) was formed, and all peaks in the obtained pattern solely corresponded to the HA phase. Peaks were sharp and distinct, which indicated that the sintered HA was pure and highly crystalline. The average crystallite size estimated with the Debye−Scherrer method and equation 3.4 was found to be ~ 60 -70 nm. The lattice parameters were found to be, a = 9.278 Å and c = 6.226 Å (Table A-I, Appendix). XRD

pattern of cuttlefish-bone-derived HA powder sintered at 1100 $^\circ$C is clearly shown with all planes in Figure A-II (Appendix). These values are close to the standard values of HA (Shih et al. 2004). The average crystallite size of sintered hydroxyapatite from different HA sources are listed in table 4.1

Table 4.1: Average crystallite sizes of sintered hydroxyapatite from different HA sources

HA from different source	Crystallite size (nm)
AMBP	62 ± 6.3
SF	46.5 ± 0.7
SU	52.1 ± 2.3
CF	65 ± 4.1
GB	60.7 ± 13.2
SC	46.1 ± 5.4
PR	66.5 ± 2.4
SD	46.2 ± 3.4

FTIR spectra of as-synthesised and sintered HA from 8 samples are plotted in Figure 4.3(a) and (b) respectively. Infrared (IR) bands at wavenumbers ~ 445, 540−613, 960, 1035, and 1100 cm^{-1} are due to the presence of a PO_4^{3-} group in the HA (Varma and Babu 2005). Additionally, IR bands at 540−613 and 445 cm^{-1} are due to phosphate bending vibrations, and those at 960, 1035, and 1100 cm^{-1} are due to characteristic phosphate stretching vibrations (Eslami et al. 2008). In addition, CO_3^{2-} peaks, traces of carbonate ions, were found at ~1424 cm^{-1}, which was due to the environmental reactions with atmospheric CO_2. A peak found at ~3649 cm^{-1} corresponds to the stretching of the structural OH$^-$ band (Sagadevan and Dakshnamoorthy 2013). Raman spectra of as synthesised and sintered HA are shown in Figure 4.4. The band at 960 cm^{-1} corresponds to the υ_1 (stretching mode) symmetric vibrational mode of P–O, which was the most intense one. The bands located near 429 cm^{-1} and 590 cm^{-1} were υ_2 (doubly bending mode) and υ_4 (triply degenerate bending

mode) PO$_4$ vibrational mode. υ_3 (triply generate antisymmetric stretching mode) vibrational mode of PO$_4$ was located at 1084.4 cm^{-1}.
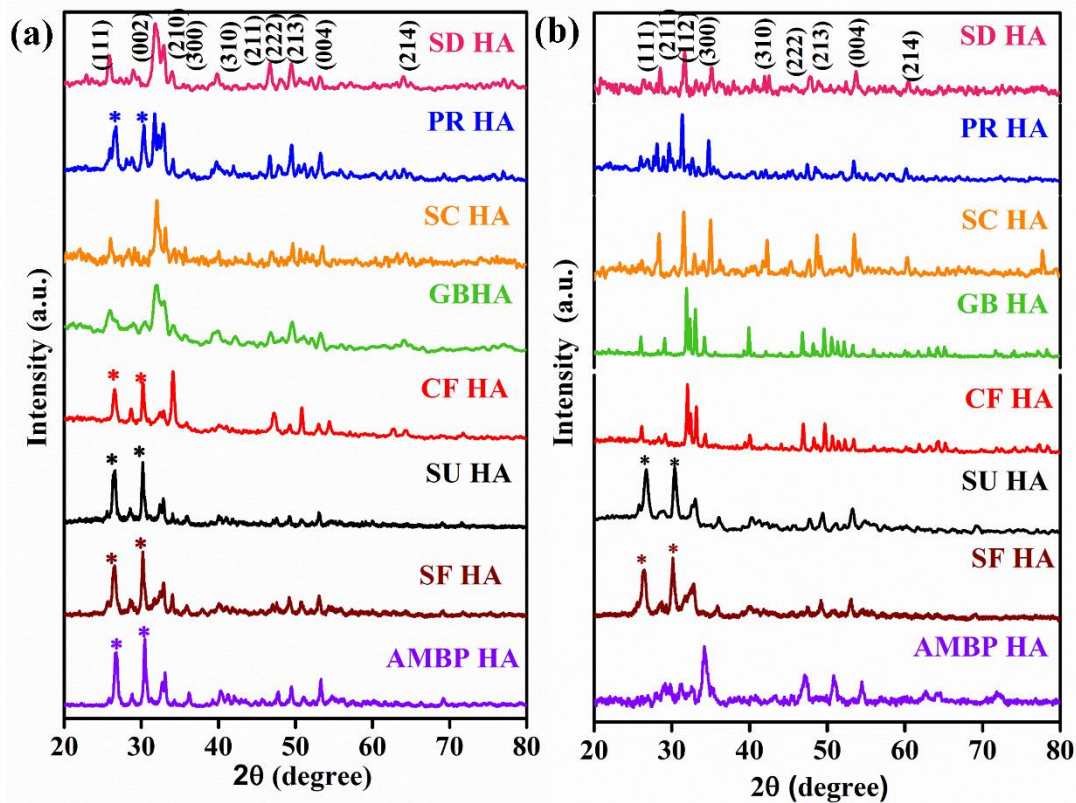
Figure 4.2: XRD pattern of (a) as-synthesised and (b) sintered HA (1100 °C), *: CaHPO$_4$

SEM micrographs of the as-synthesized HA powder from 8 samples are shown in Figure 4.5 (a-h). It revealed the presence of smaller and greater agglomerated particles with different dimensions, whereas particles were elongated needle shaped and irregular shaped. Figure 4.6 (a) shows the transmission electron microscopy image of as-synthesized nano-hydroxyapatite powder. An average width in the range of 25 ± 3.9 nm and length in the range of 102.7 ± 7.4 nm was calculated through transmission electron microscopy. Particles with an elongated rod like structure showed lattice fringe pattern with a d spacing of 3.53 Å between certain planes; nano sized rod-like particles were reported to be the best morphology for bioactivity (Khandan, Karamian, & Bonakdarchian, 2014). Figure 4.6 (b) shows the selected area diffraction pattern, the distinctive hydroxyapatite crystalline planes are observed, which are consistent with the earlier reports (Venkateswarlu et al. 2010).
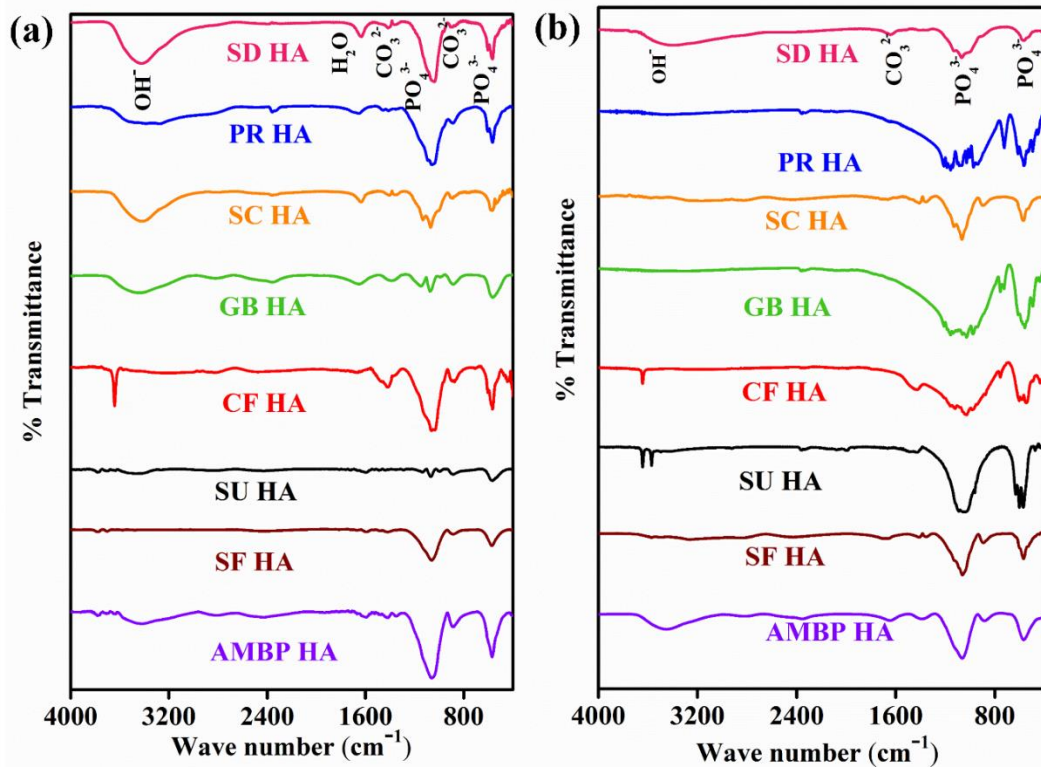
Figure 4.3: FTIR spectra of (a) as-synthesised and (b) sintered HA (1100 ^{o}C)
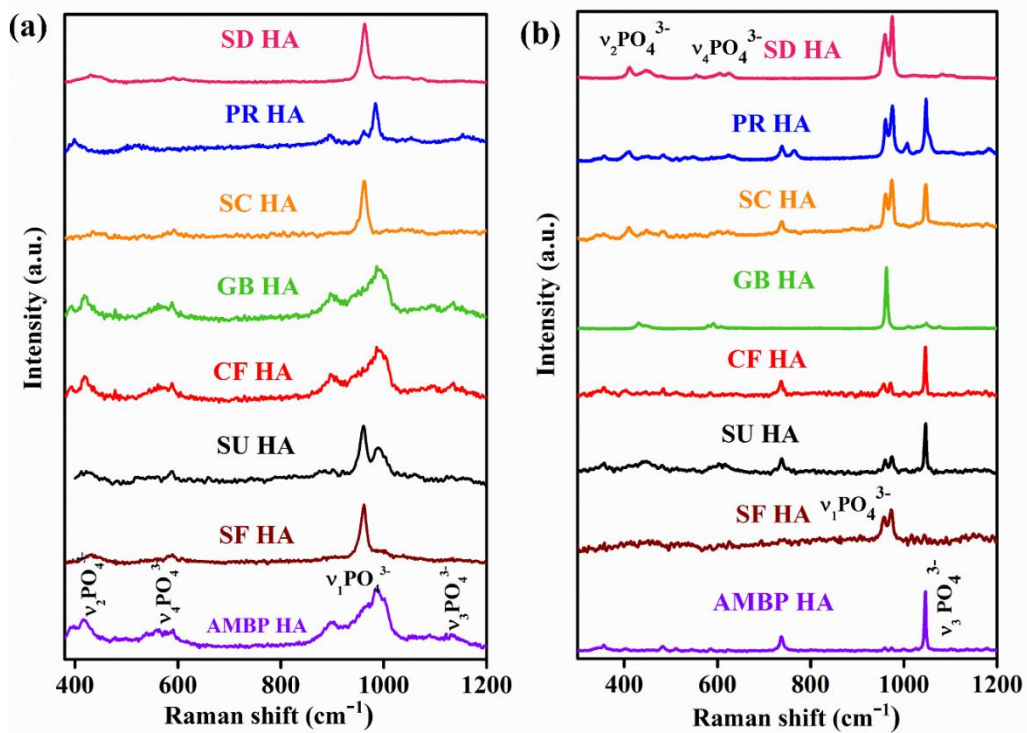
Figure 4.4: Raman spectra of (a) as-synthesised and (b) sintered HA (1100 °C)
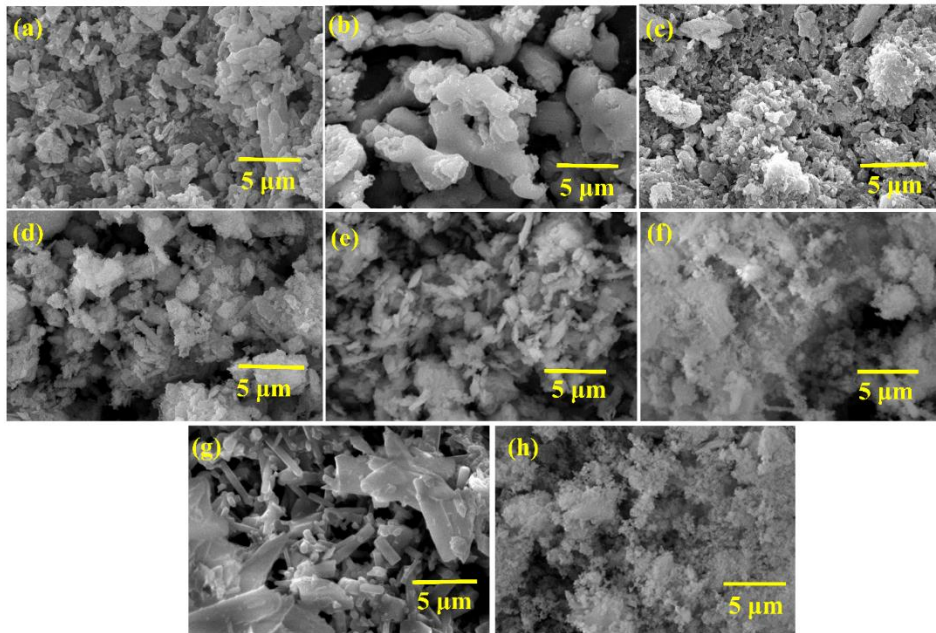
Figure 4.5: SEM images of as-synthesised HA powder
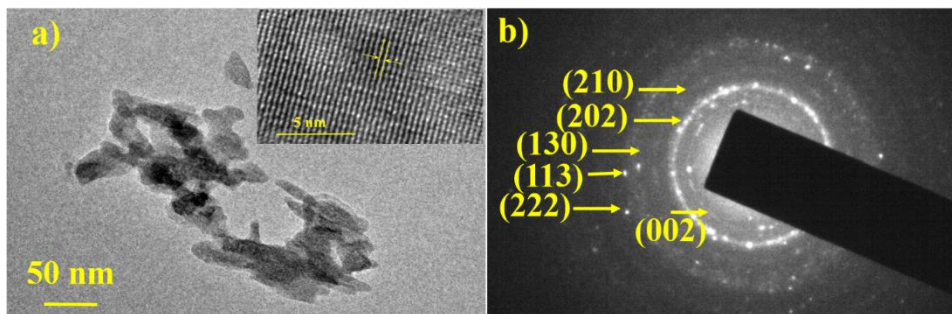
Figure 4.6. (a)Transmission electron microscopic micrograph (inset lattice fringe pattern) and (b) selected area diffraction pattern of as-synthesised HA from cuttlefish bone.

Figure 4.7 (a-h) shows the scanning electron microscopic images of the sintered HA scaffold surface from 8 samples. An equiaxed grain structure with an average size of 2.8 ± 0.8 μm was observed in SEM. Table 4.2 shows the results of EDS analysis of sintered HA from 8 samples. It confirms the presence of constituent elements of HA Ca, P, and O. Interestingly, the presence of trace elements like Na, Fe, Mg, Si was observed in as-synthesised as well as sintered HA (Table 4.2), which is because of natural origin (marine benthos) as source material to synthesis HA. Figure 4.8 shows the EDS analysis of sintered hydroxyapatite from cuttlefish bone, where Ca/P ~ 1.66

was confirmed. Trace elements are beneficial during biomineralization and other bioactivities. The presence of ions can play a key role as they directly enhance the various biochemical reactions linked to bone metabolism in bone repair and regeneration (Akram et al. 2014).
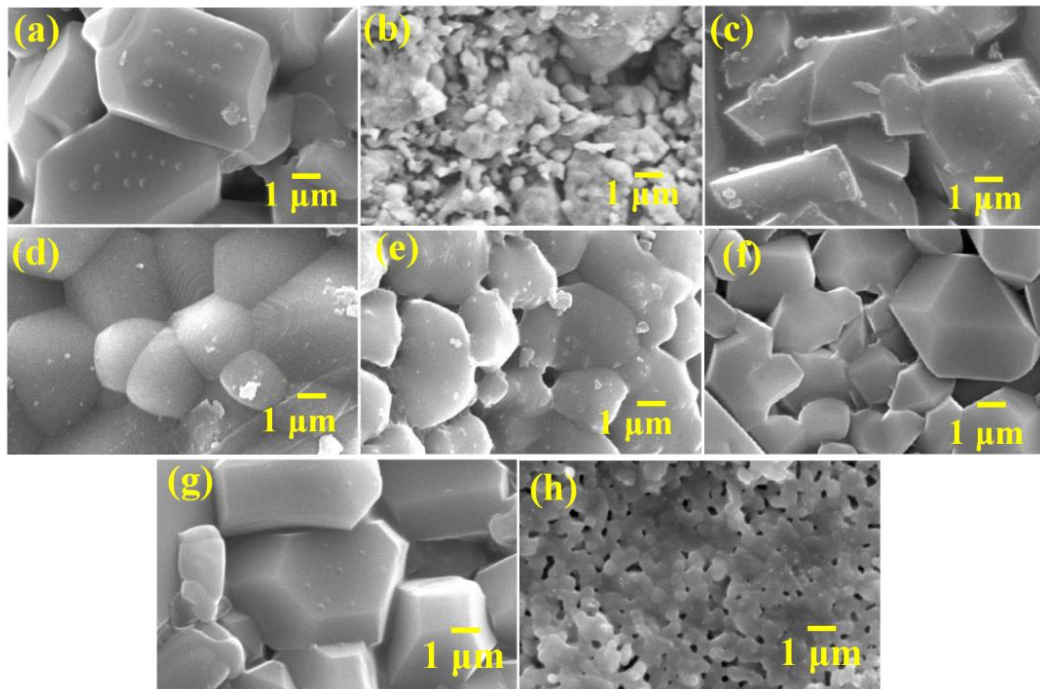
Figure 4.7: SEM images of sintered HA (1100 °C) from a) *Austromegabalanus psittacus* (AMBP), b) Star fish (*Asteroidea*), c) Sea urchin (*Echinoidea*) d) Cuttlefish bone (*Sepia Officinalis*) e) Goose barnacle (*Lepas Anserifera*), f) Sea Crab (*Neptunus Sanguinolentus*), g) Prawn shell (*Fenneropenaeus indicus*) and h) Sand Dollar (*Clypeaster humilis*).
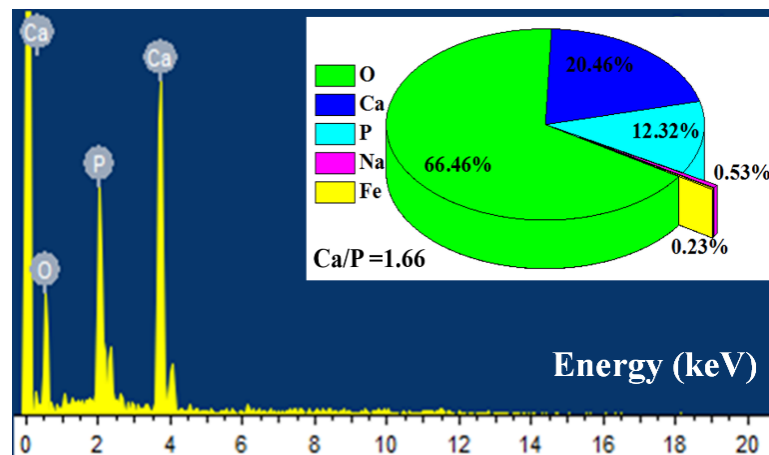
Figure 4.8: EDS analysis of sintered hydroxyapatite (1100 °C) from cuttlefish bone

Table 4.2: Presence of trace elements in biogenic hydroxyapatite

Sl no.	Marine benthos	Trace elements	
		As synthesised HA	Sintered HA
1	AMBP	Na, Fe, Mg	Na, Fe, Mg
2	Starfish	Na, Fe, Mg	Na, Fe, Mg
3	Sea urchin	Na, Fe, Mg	Na, Fe, Mg
4	Cuttlefish bone	Na, Fe	Na, Fe
5	Goose barnacle	Na, Fe, Mg	Na, Fe, Mg
6	Sea Crab	Mg	Mg
7	Prawn shell	Mg, Si, Na, Fe	Mg, Si, Na, Fe
8	Sand dollar	Mg	Mg

Table 4.3: Physical and mechanical properties of sintered hydroxyapatite

Sl no	Marine benthos	Bulk density (g/cc)	Apparent density (g/cc)	Open porosity (%)	Compression strength MPa	Compression modulus GPa
1	AMBP	2.3 ±0.08	2.65 ±0.04	15.8±2.1	44 ± 13.23	3 ± 1.05
2	Star Fish	2.3±0.27	2.58±0.08	10.6 ±1.3	34 ± 4.5	1.2 ± 0.8
3	Sea Urchin	2.3±.03	2.48±0.26	13.6 ±1.2	30.3 ± 12.7	2.03±0.74
4	Cuttlefish bone	2.6±0.13	2.61 ±0.14	5.7 ± 1.5	40.75 ±9.05	4 ±1.35
5	Goose Barnacle	2.4±0.09	2.74 ±0.08	14.4 ±0.8	29 ± 4.7	2.13 ± 0.8
6	Sea Crab	2.5 ± 0.1	2.84 ±0.07	11.8 ±1.7	20.33 ± 6.5	1.4 ± 0.6
7	Prawn shell	2.2±0.39	2.2 ± 0.38	1.3 ±0.92	65.5 ± 21.7	4.15± 0.2
8	Sand Dollar	1.9±0.18	2.78 ± .16	29.9 ±6.7	28.25 ± 9.21	2.15 ± 1.04

The values of bulk density, apparent density, open porosity, compressive strength and compressive modulus values of sintered HA prepared from 8 different marine benthos are tabulated in Table 4.3. Sintered HA from AMBP, cuttlefish bone

and prawn exhibit high compressive strength and modulus comparatively. Especially, HA from prawns has the lowest porosity (~ 1.3%) and the highest strength of 65.5 ± 21.7 MPa. HA from goose barnacle expresses moderate values of compressive strength and modulus. Unlike other samples, sand dollar HA shows high porosity of ~ 30% with a compressive strength of 28.3 ± 9.2 MPa. By considering compressive strength and modulus values of sintered HA from AMBP, cuttlefish bone, goose barnacle, prawn and sand dollar samples were selected to construct porous HA scaffolds. It is important to mention that porous scaffolds should have considerable porosity with retained strength for bone regeneration and compressive modulus is a well-considered parameter in bioceramics for bone regeneration applications. Based on the consistency and repeatability of data, mentioned 5 kinds of HA were chosen for porous HA scaffold construction. Porous scaffolds of these samples were prepared by adding 10 wt. % organic pore former such as wheat flour.

4.1.2 Porous hydroxyapatite

Figure 4.9 (a-e) reveals the SEM images of surface and pore-morphology of sintered porous HA scaffolds from AMBP, CF, GB, PR and SD with 10 wt.% wheat flour as pore former. The porous structure comprising of limited aggregates and fully interconnected pores, irrespective of pore formers. Spherical intra-agglomerate pores and inter-agglomerate pores along with structural continuity and domain formation were observed in AMBP, CF, GB with good structural homogeneity and interconnectivity. But in the case of HA scaffolds from prawns, a minimum porous structure and denser grain are observed. Finally, the HA scaffold from SD shows the much small grains with large porosity (Table 4.3).

The bulk density, apparent density, open porosity, compressive strength and compressive modulus of porous HA scaffolds where wheat four (10 wt %) is used as pore former are tabulated in Table 4.4. Porous HA scaffolds from cuttlefish bone exhibit compressive strength of 14 ± 0.3 MPa with open porosity of 34 ± 0.5 % which can be recognized as a suitable scaffold. Meanwhile, prawn HA exhibit significantly high strength with minimal porosity can be considered as a promising material where fully dense HA is required.
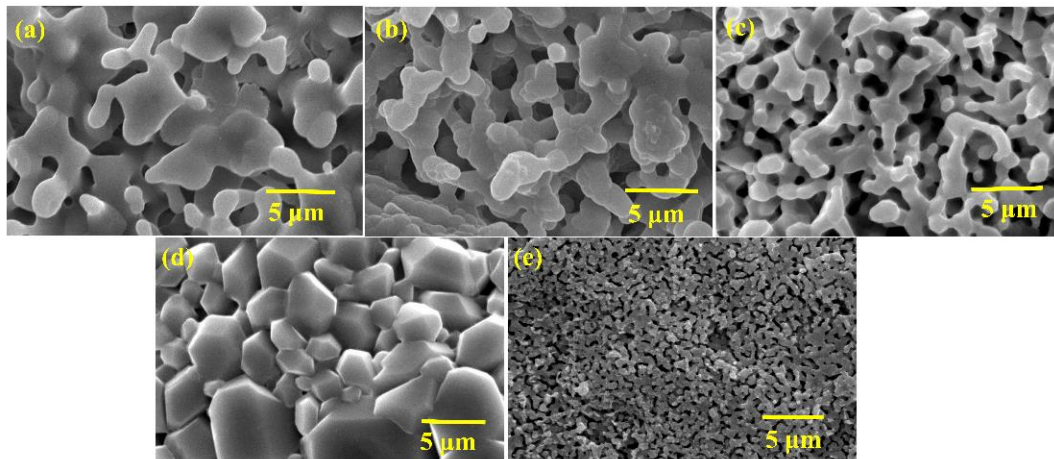
Figure 4.9: SEM images of porous HA scaffolds from (a) AMBP, (b) CF, (c) GB, (d) PR and (e) SD, where 10 wt.% wheat flour used as pore former in all cases.

Table 4.4: Physical and mechanical properties of porous hydroxyapatite (10 wt.% wheat flour as pore former)

Marine benthos	Bulk density (g/cc)	Apparent density (g/cc)	Open porosity (%)	Compression strength (MPa)	Compression modulus (GPa)
AMBP	1.34 ± 0.05	2.5 ± 0.1	46.5 ± 1.2	8.02 ± 1.05	1.13 ± 0.166
Cuttlefish	1.5 ± 0.015	2.3 ± 0.1	34 ± 0.5	14 ± 0.32	1.56 ± 0.05
GB	1.6 ± 0.05	2.4 ± 0.1	35 ± 2	7 ± 1.00	0.4 ± 0.1
Prawn	2.42 ± 0.07	2.5 ± 0.4	2.5 ± 1.34	50 ± 18.67	4 ± 1.72
Sand dollar	1.39 ± 0.06	2.4 ± 0.2	40.7 ± 6.1	4.2 ± 1.3	$0.233 \pm .15$

4.2 Cuttlefish bone based porous hydroxyapatite scaffolds

The development of a porous HA scaffold from cuttlefish bone is highly reproducible and scalable. XRD analysis of sintered cuttlefish HA confirms the no secondary phases (after sintering) are formed and all peaks in the obtained pattern solely correspond to the HA phase (ICDD: 01-074-0565) (Figure 4.2(b). The energy-dispersive X-ray spectroscopic (EDS) analysis confirmed the stoichiometric ratio of

calcium and phosphate (Ca/P = 1.66). The existence of trace amounts of Na and Fe was also detected as shown in Table 4.1 and Figure 4.8.

4.2.1 XPS investigation of sintered hydroxyapatite from cuttlefish bone
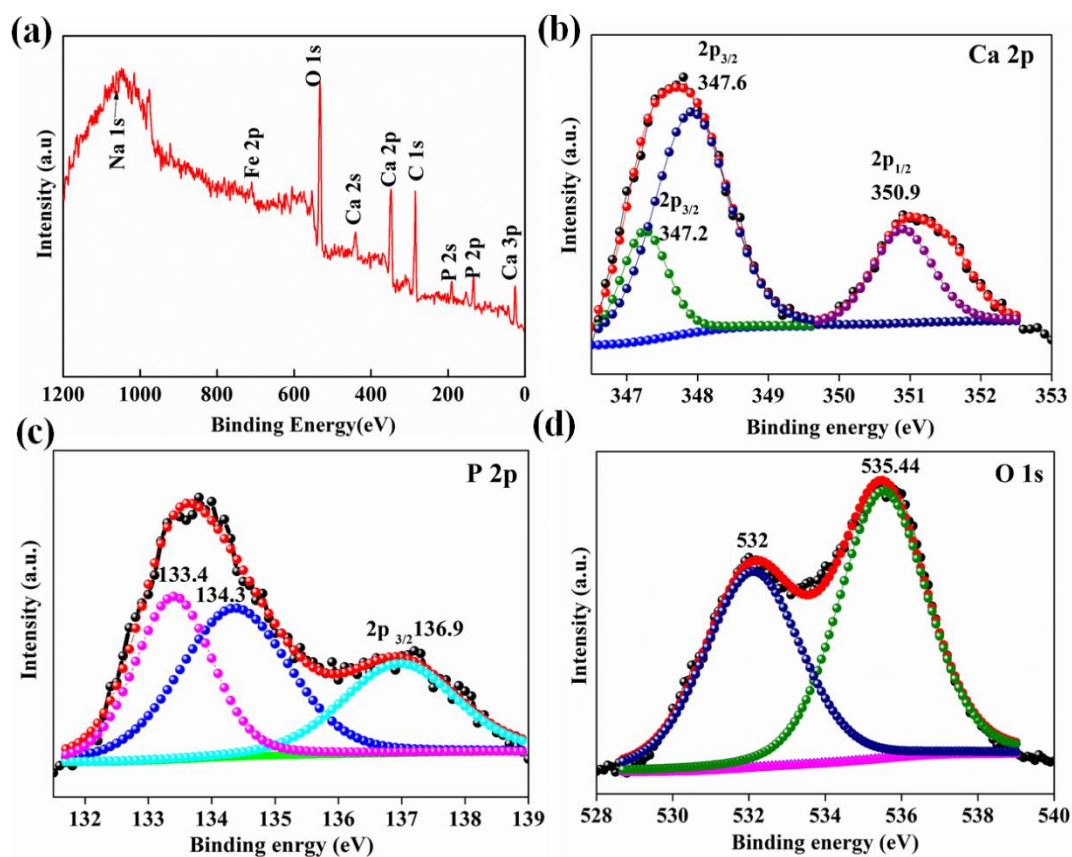
Figure 4.10: XPS investigation confirms the formation of phase-pure hydroxyapatite sintered from cuttlefish-bone-derived powder with no pore former at 1100 °C. (a) Survey spectrum and high-resolution spectra of (b) Ca 2p, (c) P 2p, and (d) O 1s.

The surface composition of as-synthesized HA powder from cuttlefish bone is shown in Figure A-III (Appendix). The surface composition of sintered HA was investigated by X-ray photoelectron spectroscopic (XPS) analysis (Figure 4.10). The survey peaks at individual binding energies reveal the existence of particular elements in the specimen under inspection and an analysis of the peak intensities contributes toward the quantitative assessment of the composition of the surface region. Figure 4.10 (a) shows the XPS survey spectrum in a wide range for the sintered HA phase. C 1s, Ca 2p, P 2p, O 1s, Fe 2p, and Na 1s peaks were identified at binding energies of 284.8,

348.4, 134.5, 532.3, 710, and 1070 eV, respectively. XPS spectra of Ca, P, and O are depicted in Figure 4.10 (b−d). In Figure 4.10 (b), XPS spectra of Ca 2p peaks are located at 347.2 ($2p_{3/2}$), 347.6 ($2p_{3/2}$), and 350.9 eV ($2p_{1/2}$), which are assigned to the calcium in $Ca_{10}(PO_4)_6(OH)_2$. Likewise, P 2p bands are located at 133.4 (2p), 134.3 (2p), and 136.9 ($2p_{3/2}$), which corresponds to the phosphate group of HA (Figure 4.10(c)). Figure 4.10(d) describes the deconvoluted spectra of O 1s at 532 and 535.44 eV of $Ca_{10}(PO_4)_6(OH)_2$, which are assigned to the phosphate group and hydroxyl group, respectively (Anwar et al. 2017).

4.2.2 Thermal analysis

To realize the thermal behavior during sintering, blended HA (with 10 wt % pore former) is subjected to TGA. Figure 4.11 shows the TGA curves of HA powder with all three pore formers, namely, wax, wheat flour, and milk powder. The TGA curve shows three main regions of weight loss, named stages I, II, and III. Figure A-IV (Appendix) shows the TGA of HA powder without pore former, exhibits only 8 % weight loss in the temperature interval of 300−650 °C which is because of the removal of lattice water. Figure 4.11(a) represents TGA curves for HA with wax as the pore former; where a total weight loss is found to be ∼ 23 %. Stage I is attributed to the loss of adsorbed water and the initial burning of wax in the temperature range of 90−350 °C. Further weight loss in the range of 350−415 and 415−670 °C is assigned to the combustion of the pore former and the elimination of lattice water, respectively (Bogdanoviciene et al. 2006; Poinern et al. 2014; Varma and Babu 2005). Figure 4.11 (b) reveals the weight loss of 21 %, with wheat flour as a pore former. Stage I with a temperature range of 80−330 °C corresponds to the evaporation of adsorbed water and the burning of the pore former. Stage II with 330−450 °C and stage III with 450−680 °C are due to the burning of the pore former and the removal of lattice water respectively. Finally, 24 % of weight loss in the case of milk powder as a pore former is observed in Figure 4.11 (c). Stage I in the temperature range of 100−270 °C and stage II at 270−450 °C attributed to the removal of moisture and the burning of milk powder respectively. Stage III in the temperature interval of 450−720 °C is associated with the loss of lattice water (Bogdanoviciene et al. 2006; D. Mehta et al. 2017).
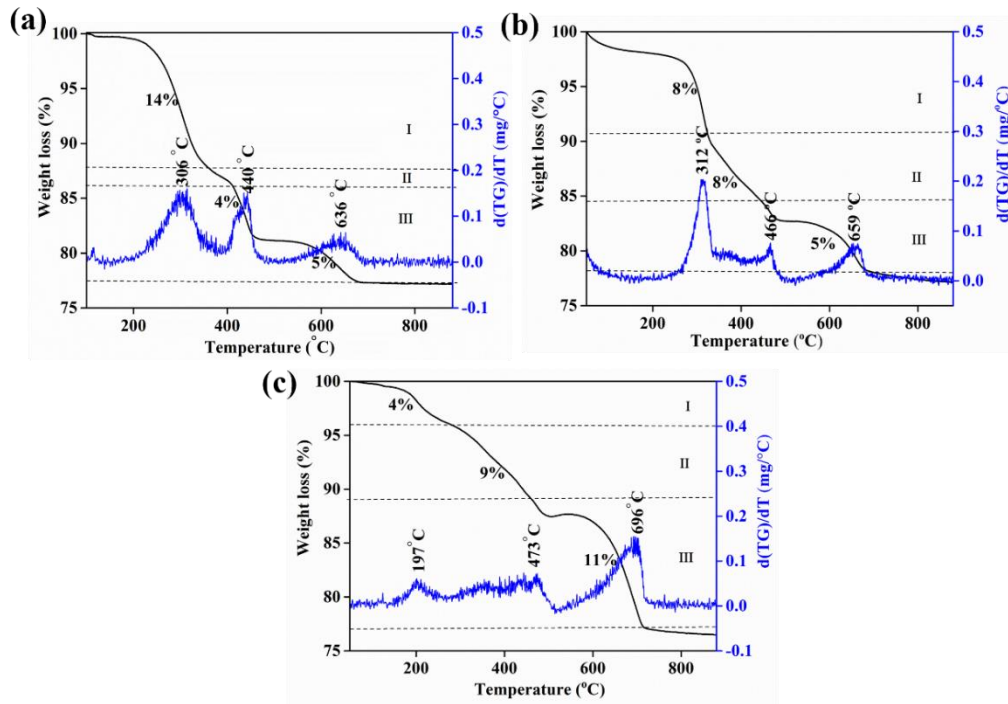
Figure 4.11: Thermogravimetric assessment provides the signature of thermophysical events as a function of temperature. TGA plots of the green compact of hydroxyapatite with (a) wax, (b) wheat flour, and (c) milk powder. Weight loss at different stages I, II, and III is indicated in each plot.

4.2.3 Physical and mechanical properties of porous hydroxyapatite scaffolds

The physical properties of the HA scaffold are determined by open and closed porosity, originated from the escape of pore formers during sintering. The escape of pore formers differs according to the burning/decomposition temperature of pore formers. A comparative study of physical and mechanical properties of porous HA scaffold with wax, wheat flour and milk powder as pore formers are represented in Table 4.5 and Figure 4.12. It is necessary to retain the compressive strength with maintained high porosity to perform a specific function as scaffolds. In that concern, a considerably high compressive strength of 14 ± 0.32 MPa and 14.8 ± 0.05 MPa was observed in wheat flour and milk powder pore formers based scaffolds with open porosity of 34 ± 0.5 and 39.3 ± 0.2 % respectively. But wax based scaffolds show the lowest compressive strength of 3.9 ± 0.3 MPa with an almost similar open porosity ~ 29.48 ± 0.15 %. The porous architecture (both open and closed) was found to have ~

91 ± 5, ∼ 98 ± 0.3, and ∼ 94 ± 5.3 % interconnectivity for HA sintered with wax, wheat flour, and milk powder, respectively. The dense HA without pore former had mostly non-interconnected pores with 5.6 ± 2.2 % interconnectivity.
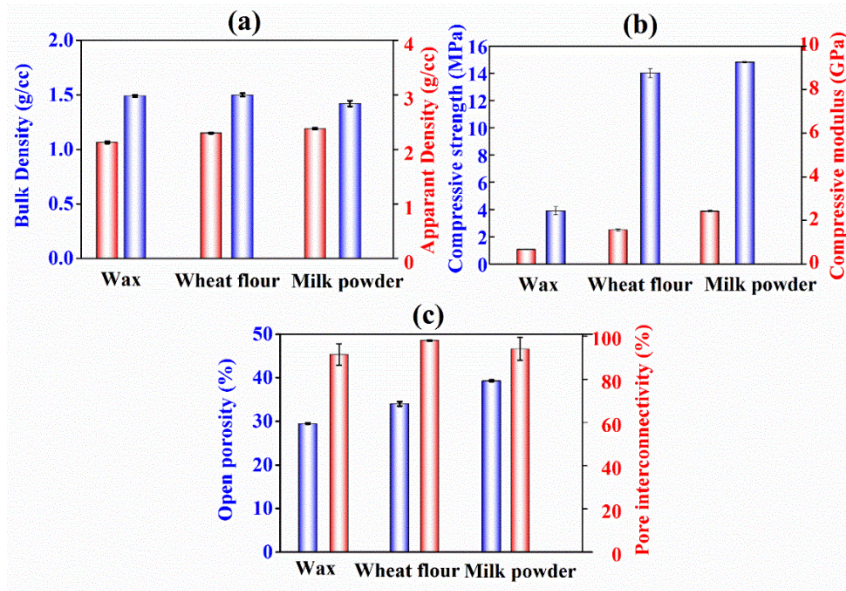
Figure 4.12: (a) Bulk and apparent density, (b) compressive strength and modulus, (c) open porosity and pore interconnectivity of porous HA scaffolds with three different pore formers (10 wt.%)

Table 4.5: Physical mechanical properties of porous hydroxyapatite scaffolds (from cuttlefish bone) with three different pore formers (10 wt.%).

Sl no.	Pore former	Bulk density (g/cc)	Apparent density (g/cc)	Open porosity (%)	Pore interconnectivity (%)	Compression strength MPa	Compression modulus GPa
1	Wax	1.49 ±0.01	2.13 ± 0.02	29.48 ± 0.15	91 ± 5	3.9 ± 0.3	0.66 ±0.012
2	Wheat flour	1.50 ± 0.015	2.3 ± 0.013	34 ± 0.5	98 ± 0.3	14 ± 0.32	1.56 ±0.05
3	Milk powder	1.42 ±0.026	2.38 ±0.015	39.3 ± 0.2	94 ± 5.3	14.8 ± 0.05	2.42 ±0.04
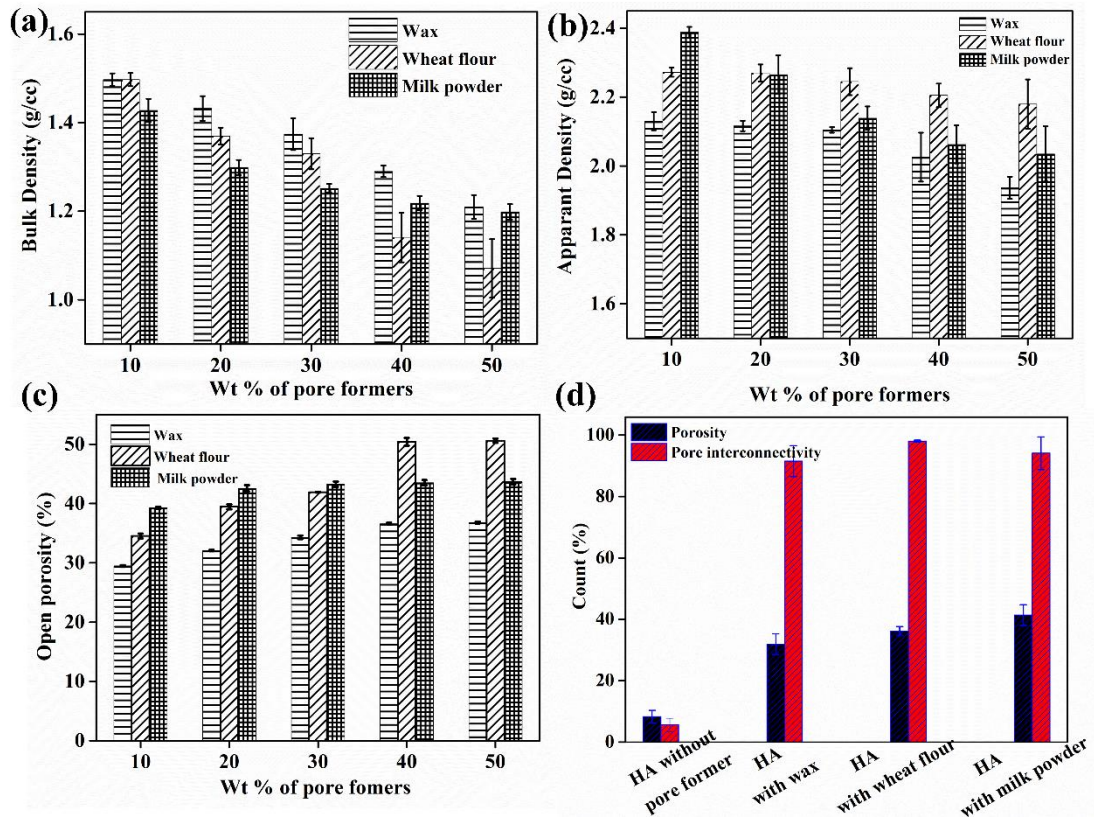
Figure 4.13: Quantitative assessment of density (both bulk and apparent), porosity, and pore interconnectivity using complementary techniques, like the conventional Archimedes' principle and microcomputed tomography, reveals the influence of different pore formers on the development of porous HA. (a) Bulk density, (b) apparent density, and (c) % open pore of sintered hydroxyapatite as a function of the addition of pore former. (d) Quantitative analysis of microporosity of computed tomograms with total porosity and interconnectivity obtained from micro-CT.

Figure 4.13 (a-c) represents the variation of bulk density, apparent density, apparent porosity as a function of the incorporation of pore formers. Figure 4.13(d) reveals the total porosity and interconnectivity of dense HA and porous HA with three different pore formers (10 wt%). The apparent density and bulk density gradually decreases as the weight percentage of the pore former increases. Bulk density was found to be 1.5 ± 0.014 g/cc in wax, 1.5 ± 0.015 g/cc in wheat flour and 1.43 ± 0.026 g/cc in milk powder of 10 wt.% addition in each case. In the case of milk powder as a pore former (10 wt.%), the scaffolds exhibit the lowest bulk density (1.43 ± 0.026 g/cc) and the highest apparent density (2.4 ± 0.015 g/cc), which signify a higher amount of

interconnected open pore (39 %). Similarly, 34 % of open porosity was achieved with wheat flour with a bulk and apparent density of 1.5 ± 0.015 g/cc and 2.3 ± 0.013 g/cc, respectively. The porosity of ~ 30 % was obtained in the wax (10 wt.%) as pore former. A total porosity, considering open and closed pore, was estimated from micro-CT analysis found to be 8.3 ± 2 % for HA without pore former and 32 ± 3.3 %, 36.1 ± 1.4, and 41.3 ± 3.34 % HA with wax, white flour and milk powder, respectively (Figure 4.13(d)).

The volume fraction of pores in HA scaffolds, which was inaccessible to Helium gas, was calculated from apparent density using He-gas pycnometry (Chang 1988). 10.8 % closed porosity was measured with milk powder as pore former, whereas it was 6.2 % for wheat flour. The apparent density of dense hydroxyapatite using pycnometry (3.14 g/cc) is more accurate compared to the Archimedes principle with water displacement (2.85 ± 0.05 g/cc). The closed porosity of 0.6 % was found in HA without pore former. This could be due to the easier penetration of He-gas to the open pores (micron and nanosized) in pycnometry than water in Archimedes method due to larger molecular size. A similar trend was observed with the porous scaffold also.

Wheat flour and milk powder contribute towards the larger amount of open porosity in comparison to wax, because of the nature of pore former and its decomposition temperature. The higher decomposition temperature of the pore former contributes towards a high range of open porosity. Although open porosity was significantly high in wheat flour and milk powder, compressive strength and compressive modulus were found to be on the higher side due to highly interconnected porous structure.

With reference to mechanical properties, Figures 4.14 (a) and (b) show the variation of compressive strength and compressive modulus with respect to the addition of pore former. A relatively higher compressive strength was observed in the case of milk powder (14.8 ± 0.05 MPa), whereas those sintered with wheat flour exhibited a slightly lower strength of 13.7 ± 0.32 MPa. The least compressive strength (3.9 ± 0.3 MPa) was observed in the case of wax as a pore former (10 wt.%). In parallel, the compressive modulus of porous hydroxyapatite was found to be 2.42 ± 0.04, 1.56 ± 0.05, 0.66 ± 0.01 GPa with 10 wt.% of milk powder, wheat flour and wax, respectively.

Both, compressive strength and compressive modulus decreased as the weight percentages of pore former increased. Interestingly, the retention of high strength while maintaining high porosity (% of the open pore) was observed with milk powder and wheat flour as pore formers. Whereas, sintered dense hydroxyapatite (bulk density and apparent density of 2.5 ± 0.05 g/cc and 2.85 ± 0.05 g/cc with an open porosity of 5.5 ± 0.15 %) also exhibit a very high compressive strength and compressive modulus of 40 ± 2 MPa and 3.9 ± 0.15 GPa, respectively.

The variation in compressive strength and compressive modulus with fractional open porosities of HA with and without pore formers are shown in Figure 4.14(c-h) as a log-log coordinate plot. The analytical relationship of compression strength (σ) using Power's model (P. K. Mehta and Monteiro 2017) is as follows,

$$\sigma = \sigma_o \, (1 - p)^m \dots\dots\dots\dots\dots\dots\dots\dots\dots\dots\dots\dots\dots\dots\dots\dots\dots \quad (4.1)$$

where, σ_o is the compressive strength of fully dense ceramic, p signifies the fractional porosity (open porosity) and m denotes the power-law exponent. The above power-law model is valid up to a certain value of open porosity; approximately up to 50 %. Figure 4.13(c) shows the relationship of compressive strength as a function of porosity for scaffold with wax as pore former. The relationship between the compressive strength σ (MPa) and the porosity p (%) can be approximated by a statistically reliable ($R^2 = 0.99$) equation, $\sigma = 61 \, (1 - p)^{8.3}$. Figure 4.14 (d) shows the relationship of compressive strength as a function of porosity for scaffold with wheat flour. The relationship between the compressive strength and the porosity can be defined by a statistically reliable ($R^2 = 0.97$) equation, $\sigma = 49 \, (1 - p)^{3.8}$. Similarly, Figure 4.14 (e) shows the variation of compressive strength as a function of porosity with milk powder as pore former with relation $\sigma = 48 \, (1 - p)^{3.6}$, where ($R^2 = 0.91$). Power's model equation has been fitted with a particular range of σ_o ($48 < \sigma_o < 61$) and power-law exponent ($3.6 < m < 8.3$) of HA for wax, wheat flour and milk powder pore formers with a good coefficient of determination of fitted regression factor (R^2). Like compressive strength, Figure 4.14((f)-(h)) shows the relationship of compressive modulus as a function of the open porosity, which follows the relation (Luo and Stevens 1999)
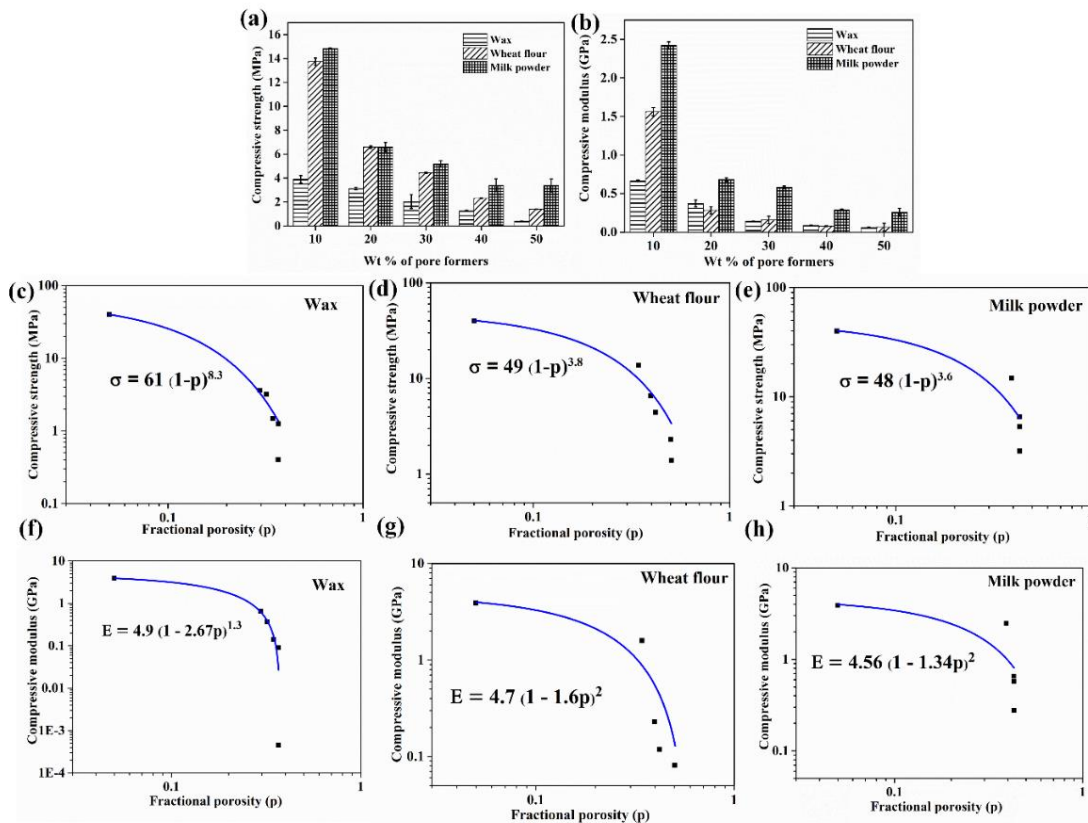
Figure 4.14: The use of different pore formers results in porous microstructure, which influences the strength and modulus properties of HA. An attempt to establish a functional relation between mechanical properties and fractional porosities. Changes of (a) compressive strength and (b) compressive modulus of porous hydroxyapatite scaffold as a function of the addition of pore former. (c-e) Compressive strength and (f-h) compressive modulus of the porous scaffold as a function of the fractional porosity of wax, wheat flour, and milk powder, respectively, represented in log-log coordinates.

$$E = E_o \, (1 - ap)^m \dots\dots\dots\dots\dots\dots\dots\dots\dots\dots\dots\dots\dots\dots\dots\dots.(4.2)$$

where E and p are the compressive modulus and fractional porosity, respectively. E_o is the compressive modulus of dense ceramic (without porosity), a and m are empirical constants (Phani & Niyogi, 1987). A reliable relationship ($R^2 = 0.99$) as $E = 4.9 \, (1 - 2.67p)^{1.3}$ was established in the case of wax as pore former (Figure 4.13 (f)). R is defined as the coefficient of determination of the fitted regression line. Figure

4.14(g) shows the relationship of compressive modulus and porosity for wheat flour with a statistically reliable relationship ($R^2 = 0.92$) as $E = 4.7\,(1 - 1.6p)^2$. Scaffold with milk powder follows a relation, $E = 4.56\,(1 - 1.34p)^2$ with $R^2 = 0.7$ (Figure 4.14(h)). In case of modulus, the values of E_o and empirical constants lies as follows, $(4.56 < E_o < 4.9)$, $(1.3 < a < 2.6)$, $(1.3 < m < 2)$. A small deviation between the fitted curve and experimental values of compressive modulus as a function of porosities was found (Figure 4.14 (g-h) with wheat flour and milk powder, because of the inhomogeneous distribution of fractional porosity points.

4.2.4 SEM and μ-CT based 2D/3D microstructural analysis

Both scanning electron microscopy (SEM) and micro-CT were extensively used to analyse the porous architecture in the HA scaffolds qualitatively and quantitatively. In particular, the 2D surface morphology of porous hydroxyapatite scaffolds was examined by SEM. SEM images are shown in Figure 4.15 (a-d) for hydroxyapatite scaffold without pore former and with different pore formers (10 wt.% of wax, wheat flour, milk powder). Figure 4.15 (a) shows the scanning electron microscopic image of sintered dense hydroxyapatite scaffold surface, exhibit an equiaxed grain structure with a size of 2.8 ± 0.8 μm. The porous structure consists of limited aggregates with fully interconnected pores, irrespective of pore formers. Spherical intra-agglomerate pores and inter-agglomerate pores along with structural continuity and domain formation were observed in all three cases with good structural homogeneity and interconnectivity (Figure 4.15 (b-d).

3D microstructure analysis of hydroxyapatite scaffold using micro-CT revealed the material and pore phase on the phase contrast image with different grey levels. The effect of organic pore former during sintering on the pore architecture and porosity of cuttlefish derived hydroxyapatite was analysed by label analysis of threshold images. The enhancement in pore interconnectivity with organic pore former can be observed in 2D orthoslices and 3D volume rendered images (Figure 4.15 (e-l). The interconnected pore phase is counted as a single object and is labeled in the same colour, unlike the non-connected pores labeled with a different colour. The naturally derived porous hydroxyapatite scaffold has mostly interconnected pore space labeled with blue

colour, except the dense hydroxyapatite one. The non-connected pores throughout the sample are labeled in the arbitrary colour code. The porous architecture, (both open and closed), was found to have, ~ 91 ± 5%, ~ 98 ± 0.3 % and ~ 94 ± 5.3 % interconnectivity for hydroxyapatite sintered with wax, wheat flour and milk powder, respectively (Figure 4.13 (d)). The dense hydroxyapatite without pore former had mostly non-interconnected pores with 5.6 ± 2.2 % interconnectivity.

The representative 3D volume rendered images show the homogenous distribution of pores throughout the porous hydroxyapatite scaffold, sintered with milk powder. The pore interconnectivity is higher in hydroxyapatite sintered with wheat flour having homogenous pore distribution. The volume fraction of the pore phase, considering open and closed pores, in dense hydroxyapatite without pore former was found to be ~ 8.3 %. The micro-CT analysis revealed that the total porosity increased to ~ 32 % hydroxyapatite/wax, in ~36.1 % in hydroxyapatite/wheat flour and ~ 41.3 % in hydroxyapatite/milk powder scaffold. Using Archimedes' principle (water displacement), the percentage of open porosity in hydroxyapatite sintered with wax, wheat flour and milk powder was measured as 30 %, 34 % and 39 %, respectively. Again, an amount of closed pore was found to be 5.7 %, 6.3 % and 10.8 % in the case of hydroxyapatite/wax, hydroxyapatite/wheat flour and hydroxyapatite/milk powder using pycnometry. So, there is an overestimation in the total pore volume compared to micro-CT scan values, which could be due to the open porosity measurement by Archimedes' principle (water displacement). The distribution of equivalent pore diameter was determined for all the samples, which follows a narrow range for dense one (Figure 4.15 (m)), but a wide range in the case of porous scaffold (Figure 4.15 (n), (o) and (p)). Figure 4.13(d) shows the total porosity and interconnectivity of dense HA and porous HA with three different pore formers (10 wt%). The porous architecture, (both open and closed), was found to have, ~ 91 ± 5%, ~ 98 ± 0.3 % and ~ 94 ± 5.3 % interconnectivity for hydroxyapatite sintered with wax, wheat flour and milk powder, respectively. The wide range of porosity up to 50 μm in porous scaffolds, is expected to facilitate biological functions, such as protein interaction, bioactivity and cell attachment in bone tissue formation (Tripathi and Basu 2012). The higher void space and interconnected pores can be attributed to the degradation of the organic pore former

during sintering at 1100 °C. The faster rate of degradation of wheat flour observed in TGA can be the reason for higher interconnectivity of pore than milk powder-based hydroxyapatite scaffold.
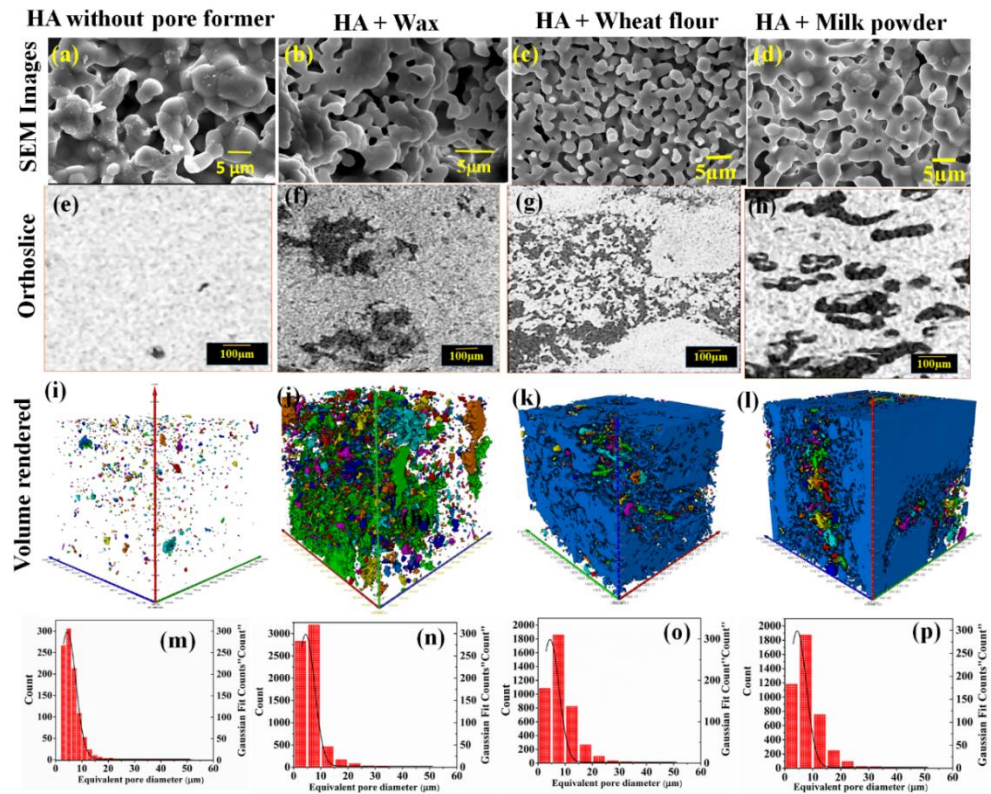
Figure 4.15: 2D and 3D microstructure analysis using SEM and microcomputed tomography, respectively, provides more insights into the porous architecture of HA scaffolds. SEM image of porous hydroxyapatite scaffold with (10 wt %) of pore formers: (a) HA without pore former, (b) HA with wax, (c) HA with wheat flour, and (d) HA with milk powder. 2D orthoslices and 3D volume-rendered images of (e, i) sintered dense HA without pore former and porous HA sintered with (f, j) wax, (g, k) wheat flour, and (h, l) milk powder as pore formers. The pores and materials can be identified in orthoslices as dark and bright gray levels, respectively. The same color codes in the volume-rendered 3D sections are labeled with pore volume with interconnectivity. The pore distribution as a function of the equivalent pore diameter plot showing the pore distribution with a narrow spectrum of size in HA (m) without pore former and a wide spectrum with the application of (n) wax, (o) wheat flour, and (p) milk powder as organic pore formers.

4.3 *In vitro* biomineralization and biodegradation

4.3.1 Biomineralization of porous scaffolds

One of the major determinants for the biological application of HA scaffolds is biomineralization. It is investigated by incubating the porous scaffolds in simulated body fluid for different time points to understand the temporal growth of new apatite formation. In particular, the soaked samples were removed from SBF after 1 hour, 6 hours, 12 hours, 1 day, 3 days and 7 days. Representative SEM images reveal the growth of apatite on porous hydroxyapatite scaffold, sintered with wheat flour and milk powder as pore formers (Figure 4.16).

A clear look at Figure 4.16 (a-l) reveals that nucleation and growth of apatite are more in the case of wheat flour as a pore former than in the case of milk powder. It may be attributed to the exchange of calcium and phosphate ions and a variation of pH level in SBF. Also, the pore interconnectivity is more in the case of scaffolds with wheat flour as pore former. After incubation of the scaffold in SBF solution, ionic dissolutions and precipitation effectively occur through several chemical reactions on the porous structure with inter and intra agglomerated interconnectivity (Chavan et al. 2010). Those reactions result in spontaneous nucleation and growth of calcium phosphate with maintaining stoichiometry (Figure 4.17 and 4.18); as the interconnected structure acts as heterogeneous nucleation sites for new apatite formation. The X-ray diffraction pattern of new apatite crystals on HA scaffold surface confirms the major phase of HA with $CaHPO_4$ as secondary phase (Figure A-V (Appendix). The composition and surface chemistry play vital roles in the biomineralization process along with material functional groups. In SBF solution, $NaHCO_3$ can dissociate into Na^+ and HCO_3^-. Also, CO_2 is released from the dissolution of HCO_3^- ions resulted in the enhancement of a large number of OH^- ions in the solution. At the interface of hydroxyapatite and SBF, the migration of calcium, hydroxyl and phosphate ions leads to the formation of new apatite crystals until the surface is fully covered with the biomineralised layer. It is known that hydroxyapatite structure consists of Ca^{2+}, PO_4^{3-} and OH^- ions with hexagonal close packing. The negative surface charges play important roles in the formation of apatite on the material surface. During soaking in SBF, positive ions, like

70
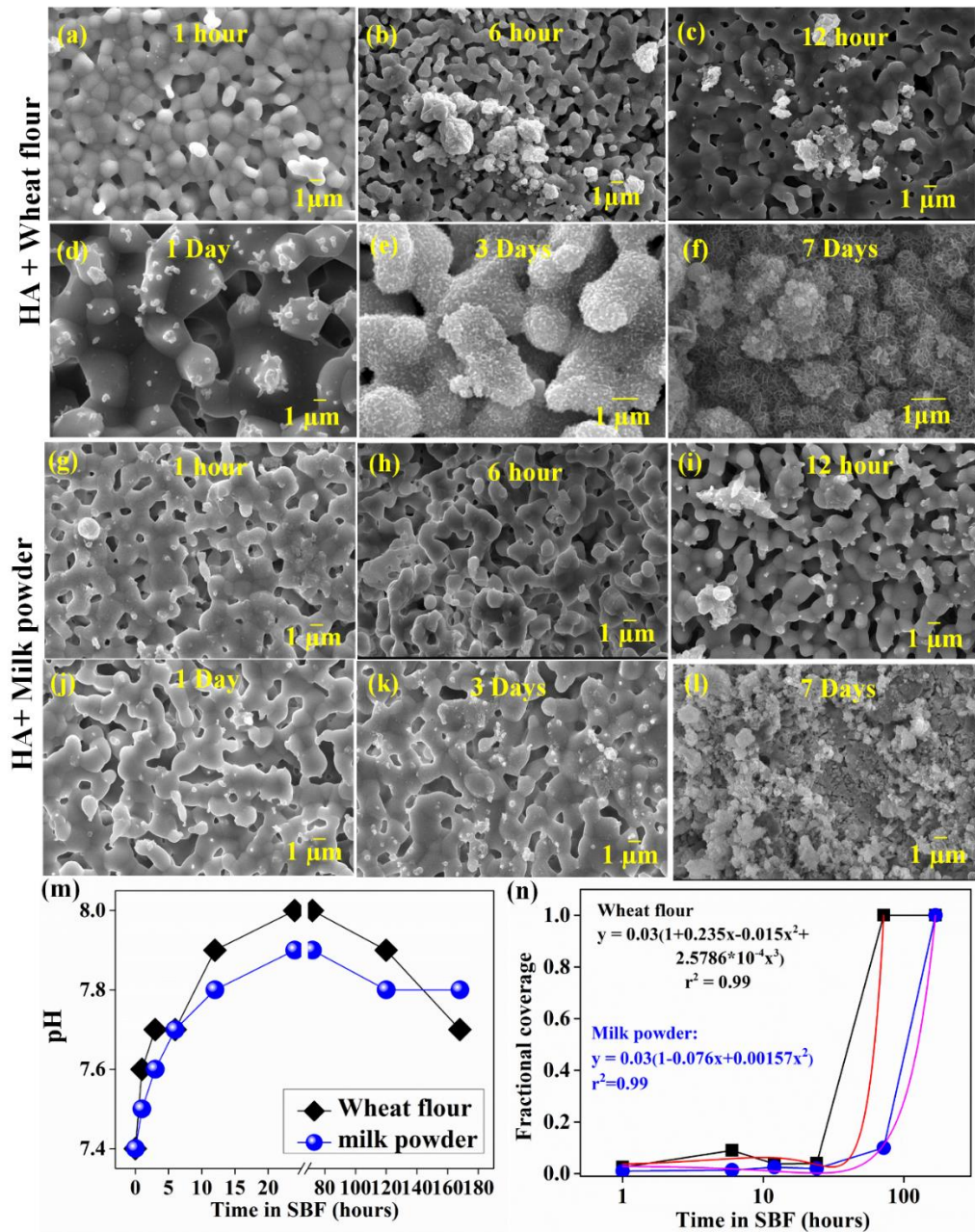
Figure 4.16: 2D surface analysis of apatite crystals and quantitate analysis of pH and fractional coverage of the apatite layer with time in SBF reveal the biomineralization behavior of HA scaffolds. SEM image shows apatite formation in SBF on the porous hydroxyapatite scaffold surface. Wheat flour as pore former: scaffold soaking time (a) 1 h, (b) 6 h, (c) 12 h, (d) 1 day, (e) 3 days and (f) 7 days. Similarly, milk powder as pore former: scaffold soaking time (g) 1 h, (h) 6 h, (i) 12 h, (j) 1 day, (k) 3 days, and (l) 7 days. (m) Variation of pH and (n) fractional coverage of apatite on the surface of scaffolds as a function of soaking time in SBF solution.

Ca^{2+} in SBF together with negative ions (PO_4^{3-} and OH^-) form new apatite (Chavan et al. 2010).

In the present context, hydroxyapatite derived from cuttlefish bone contains a trace amount of Fe^{2+} and Na^+. At the initial stage, the exchange of Fe^{2+} for Ca^{2+} ions with H^+ or H_3O^+ from SBF solution promotes more nucleation sites on the scaffold surface. It leads to faster biomineralization with quicker coverage of scaffold surface by new apatite layer. As Figure 4.16 (m) shows the pH variation with soaking time in SBF, an increase in pH level due to the dissociation of HCO_3^- in the SBF solution results in the availability of more OH^- ions. Also, the pH of the solution may increase at the initial stage due to the creation of the tri(hydroxymethyl) methylammonium cation.

Later, pH decreases gradually with the growth of apatite, as OH^- ions from the SBF solution are absorbed by the HA scaffold's surface. The variation of pH (7.4 to 8) is higher in the case of hydroxyapatite/wheat flour compared to hydroxyapatite/milk powder after one day of immersion. Hence, there is a faster growth of apatite in the case of hydroxyapatite/wheat flour. Figure 4.16 (n) shows the fractional coverage of apatite crystals as a function of soaking time in SBF. It also reveals that HA scaffold with wheat flour as pore former can support faster surface coverage compared to hydroxyapatite/milk powder, where complete coverage is observed in three days in the case of hydroxyapatite/wheat flour. The analytical equation has been fitted as $y = 0.03 (1+ 0.235x - 0.015x^2 + 2.5786\times10^{-4}x^3)$ with $R^2 = 0.99$ in case of wheat flour and $y = 0.013 (1- 0.009x + 0.00114x^2)$ with $R^2 = 0.96$, for milk powder, where x and y are time in hours and fractional coverage respectively. A similar extent of biomineralization takes seven days for hydroxyapatite/milk powder. The presence of Na^+ and Fe^{2+} ions can play a vital role as they may directly influence various biochemical reactions linked with bone metabolism in bone regeneration and repair (Akram et al. 2014).
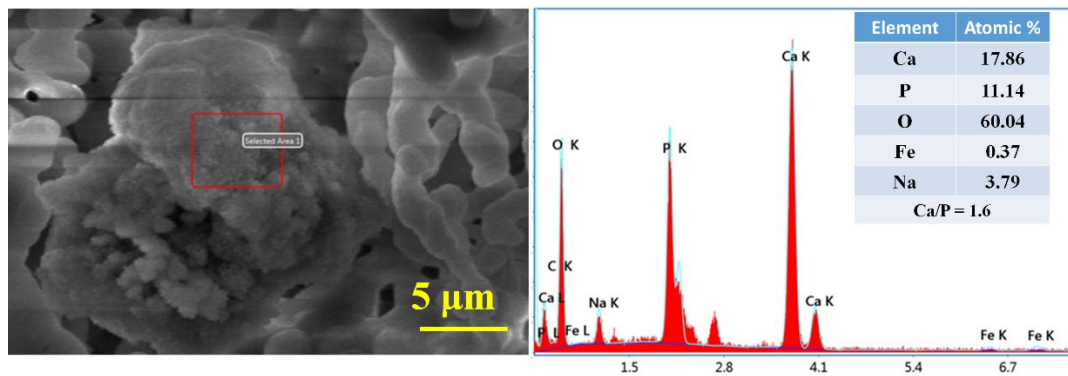
Figure 4.17: EDS analysis of porous scaffold with wheat flour as pore former incubated in SBF for 1 day.
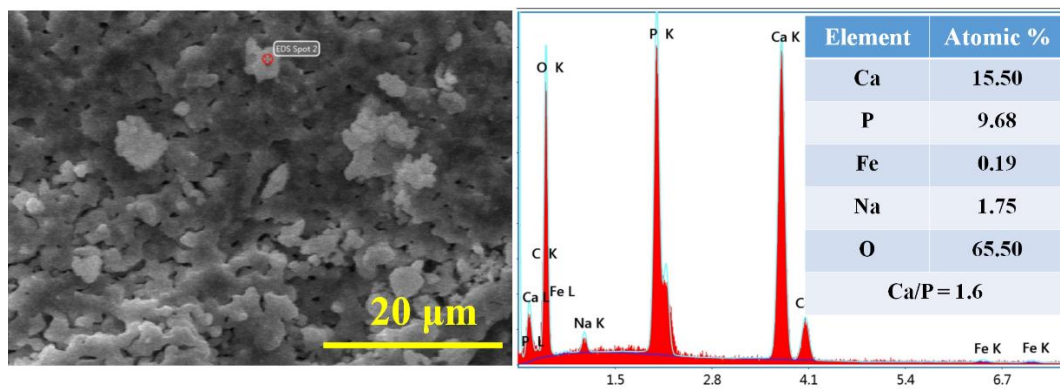
Figure 4.18: EDS analysis of porous scaffold with milk powder as pore former incubated in SBF for 1 day.

4.3.2 Biodegradation of porous scaffolds

In order to study the degradation of cuttlefish HA scaffolds, samples were soaked in 0.05 M Tris–HCl buffer solution (pH 7.4) at 37 ºC with different time points 1 h, 6 h, 12 h, 1 day, 3 days, 5 days and 7days. To measure bioresorbability, the weight loss of the scaffolds was calculated using equation 3.8, which was 1.2 and 1.6 % in wheat flour and milk powder pore former based HA scaffolds respectively as shown in Figure 4.19. The initial profile exhibits a very slow rate of degradation for up to 3 days, which increases further and measures up to 7 days. The weight loss of HA scaffolds in the tris-buffer solution can be correlated with bioresorbability, as it is an important property of scaffolds to be necessary for bioactivity (Basu et al. 2013).

4.4 *In vitro* cytocompatibility

The cytocompatibility of a biomaterial is principally governed by several parameters including elastic modulus, surface wettability, porosity etc. The water contact angle specifies the wettability of the material surface, i.e. hydrophilic/hydrophobic characteristics. The surfaces of non-biogenic HA and cuttlefish derived HA (without pore formers) exhibit the contact angle of 54.8 ± 7°, with 50.5 ± 14°, respectively. Porous HA, with wheat flour and milk powder as pore formers show the contact angle of 34.7 ± 4° and 37.4 ± 2° respectively (Figure 4.20 (a). Majority of the cells adhered mostly to the hydrophilic surfaces. Hence, more osteoblast cells were adhered to biogenic porous HA scaffold surface because of its hydrophilic nature in comparison to non-biogenic HA.
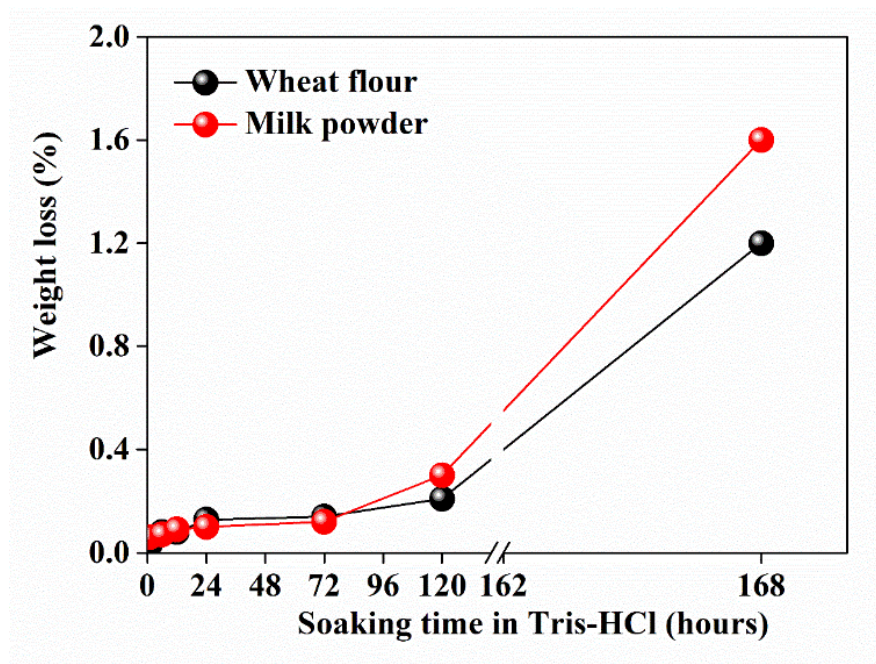
Figure 4.19: Degradation study of porous hydroxyapatite scaffolds
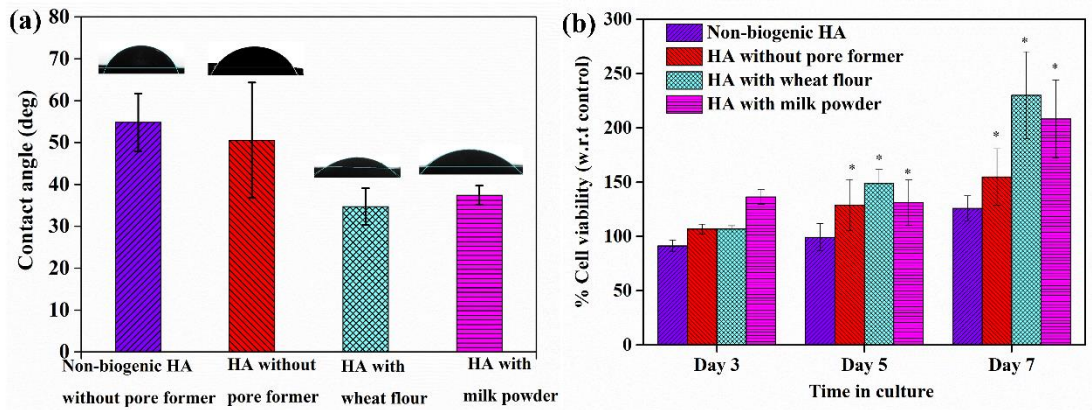
Figure 4.20: Surface wettability influences cell adhesion and proliferation. (a) Water contact-angle plot of all scaffold surfaces. (b) MTT-assay measured cell viability of mouse osteoblast cells (MC3T3-E1) at 3, 5, and 7 days of culture for HA without pore former, HA/wheat flour, HA/milk powder, and nonbiogenic HA. * denotes the statistically significant difference ($P < 0.05$) from the control at each day.

Cell viability is strongly affected by cell-material interactions, which are largely dependent on the physicochemical properties of scaffold surface. In order to assess the cell viability on cuttlefish-derived HA scaffolds, an MTT assay was performed for 3 days 5 days and 7days. The viability of osteoblast cell growth on HA scaffolds was analysed for HA scaffolds with wheat flour and milk powder as pore formers in comparison to cuttlefish HA and non-biogenic HA, without pore formers (Figure 4.20 (b)).

The reduction of MTT by the mitochondrial succinate dehydrogenase enzyme present in mitochondria leads to the formation of violet colored formazan crystals (Bhaskar et al. 2018). The percentage of cell viability was increased in the case of porous HA scaffold with respect to scaffolds without pore formers. Such observations show the efficacy of the porous scaffolds for better osteoblast adhesion and proliferation. It is therefore clear that good pore interconnectivity (98 % and 94 % respectively with wheat flour and milk powder pore formers) which has a direct effect on cell-material interaction (Basu 2017). Also, HA from biogenic precursors, containing trace elements like Na^+ and Fe^{2+} are expected to take part in biological activity (Akram et al. 2014). The faster biomineralization of HA with wheat flour pore

former is another governing factor for high cell viability. The osteoblast cell viability was significantly decreased on HA without pore former. In comparison with non-biogenic precursors HA, cellular viability was high on cuttlefish bone derived HA (Kim et al. 2014) (Figure 4.20 (b)).

The percentage of cell viability increased from day 3 to day 5 by ~ 0.4 fold and day 5 to day 7 by ~ 0.5 fold in the case of wheat flour pore former. In milk powder pore-former-based-HA scaffold, the enhancement of cell viability from day 5 to day 7 was ~ 0.58 fold. Significantly, there was less difference in cell viability on non-biogenic precursors HA with an increment from day 5 to day 7 was ~ 0.3 fold.

4.4.1 Cell morphological analysis

Figure 4.21 shows the fluorescence microscopy images of mouse osteoblast cells (MC3T3-E1), which are stained with Rhodamine Phalloidin (cytoskeleton, red) / Hoechst (33342) DAPI (nucleus, blue) after 7 days of culture. The proliferation of osteoblasts was higher on the HA scaffold with wheat flour and milk powder pore formers than on the control. HA without pore former and non-biogenic HA show a decreased cell adhesion than HA with organic pore former (Figure 4.21(a- e). The numbers of cells in each study group were calculated using ImageJ software and plotted in Figure 4.21(f). These results are in good agreement with the MTT assay; a significant number of cells adhere to HA porous scaffold after 7 days of culture. Figure 4.21(g) shows the schematic depiction of the succession of events during the interaction of cells with porous scaffold surface.

The preferably hydrophilic surface has more affinity towards attracting water molecules with the formation of a water shell, which interacts with the hydration of the shell of the biomolecule. Also, the water layer regulates the protein adsorption, which is followed by cellular adhesion on material surface (Kasemo 2002).
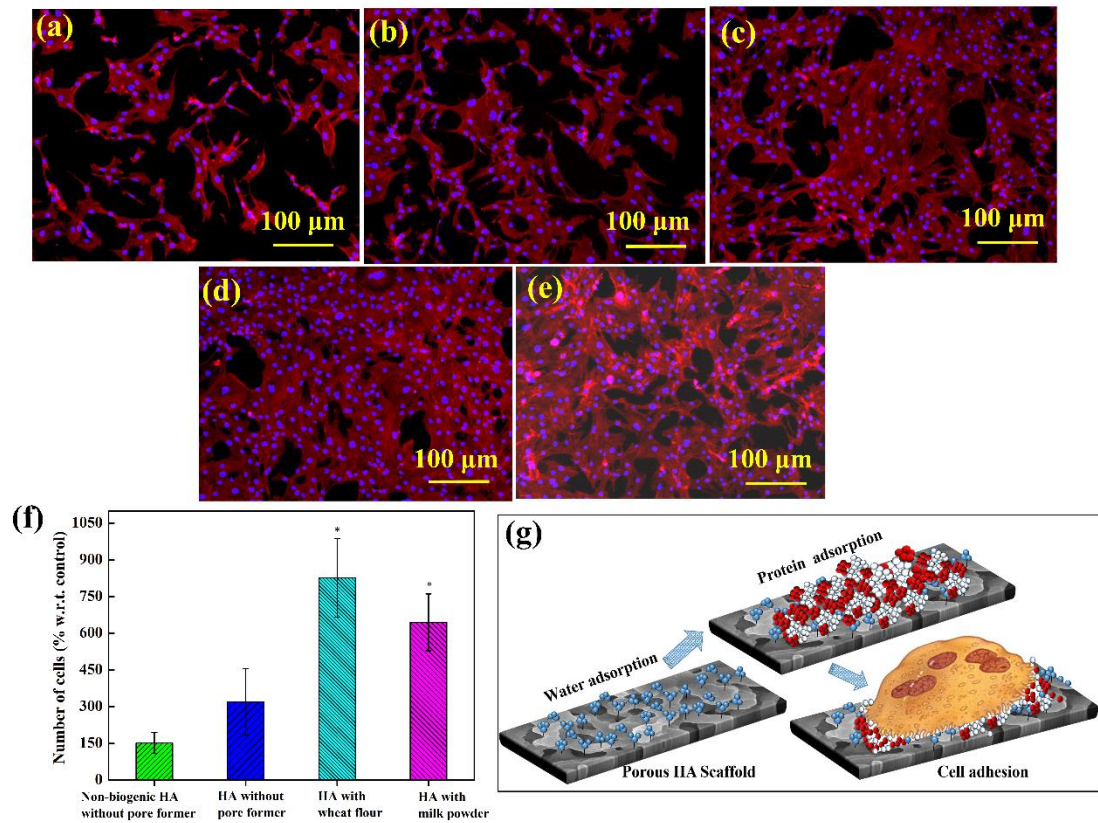
Figure 4.21: Cell morphological changes and quantitative analysis of cultured cells provide more information on cytocompatibility. Fluorescence microscopy images of rhodamine phalloidin (cytoskeleton, red)/Hoechst (33342) DAPI (nucleus, blue) staining of mouse osteoblast cells (MC3T3-E1) after 7 days of culture for each study group: (a) control, (b) nonbiogenic HA without pore former, (c) HA without pore former, (d) HA with wheat flour pore former, and (e) HA with milk powder pore former. (f) the number of cells (% w.r.t. control) on each sample surface (counted using ImageJ software). (g) Schematic depiction of the succession of events during the interaction of the cell with the porous scaffold surface.

4.5 Conclusions

Abundantly available marine benthos namely, benthos biowaste *Austromegabalanus psittacus* (AMBP), star fish (*Asteroidea*), sea urchin (*Echinoidea*) cuttlefish bone (*Sepia officinalis*), Goose barnacle (*Lepas anserifera*), Sea crab (*Neptunus sanguinolentus*), prawn (*Fenneropenaeus indicus*) and sand dollar (*Clypeaster humilis*) based calcite/aragonite was used to synthesis of biogenic HA through wet chemical precipitation method. The scalable synthesis of biogenic phase-pure HA and a tailored porous architecture from cuttlefish bone based HA scaffolds were established with aid of organic pore formers namely wax, wheat flour and milk powder. A combination of moderate compressive strength (12−15 MPa) with elastic modulus up to 1.6 GPa was achieved with ∼98 % interconnected porosity and 34 % open porosity using cuttlefish bone HA with wheat flour as the pore former.

During soaking in SBF, positive ions, like Ca^{2+} in SBF together with negative ions (PO_4^{3-} and OH^-) form new apatite. Faster biomineralization with full coverage of apatite on porous HA was achieved within 3 days of incubation in SBF. The presence of Na^+ and Fe^{2+} ions can play a vital role in a sequence of chemical reactions like spontaneous precipitation, nucleation and growth of calcium phosphate. The surface chemistry and functional groups of materials play a key role and have a large effect on the bone bonding property. Increase in osteoblast (MC3T3-E1) cell viability on HA/wheat flour and HA/milk powder scaffold surface in comparison with biogenic dense HA and nonbiogenic HA without pore formers for 7 days.

CHAPTER 5

Fe incorporated hydroxyapatite for UV protection

The effects of Fe^{3+} ionic substitution in hydroxyapatite ($Ca_{10-x}Fe_x(PO_4)_6(OH)_2$) was investigated with a series of structural analysis. It is also correlated with the UV absorbing properties of HA through a tailored band gap both experimentally and theoretically. An ion exchange procedure was used to synthesis the Fe-HA with five different concentrations. To understand the effect of Fe incorporation into HA, crystal structures, morphology, elemental composition and ionic substitution were investigated experimentally by using XRD, FTIR, XPS SEM and EDS. BET analysis was carried out for the determination of surface area and particle size of Fe-HA powders. UV absorption of Fe-HA was assessed using UV visible spectroscopy; experimentally measured optical bandgap was verified with theoretically calculated band gap using density functional theory (DFT).

5.1 Structural, morphological and elemental assessment of Fe-hydroxyapatite

XRD patterns of HA treated with 0.01-0.05 M $FeCl_3$ solution, respectively were compared with the standard HA pattern (ICDD-00-009-0432) as shown in Figure 5.1(b). The characteristic peaks of undoped HA (90°) obtained at a 2θ value of 25.83°, 28.6°, 31.8°, 32.2°, 39.7° and 46.9° are corresponding to (002), (210), (211), (112), (130) and (222) planes respectively. Figure 5.1(b) also reveals the co-existence of secondary phase $CaHPO_4$ at 2θ value of 30.24° (ICDD: 01-070-1425) along with HA which is also a class of biocompatible calcium phosphate compound. From XRD patterns it is observed that the differences in Fe-HA with a variation of Fe concentration, a peak shift towards left is observed in the exaggerated view of Fe-HA XRD pattern (Figure 5.1(c)). These results are consistent with the earlier reports. The shift may be due to a change in the lattice parameter of the Fe-HA, upon the incorporation of Fe^{3+} (0.64 Å) in the place of Ca^{2+} (0.99 Å) site in HA and its electronegative nature (Zilm et al 2016). It is expected that there may be a decrease in peak intensity and peak broadening with an increase in doping concentration. But the decrease in peak intensity is not observed in the XRD pattern in the present study.

Cohen's method is adopted to estimate the lattice parameters of the 0.01 M −
0.05 M Fe-HA more precisely (Cullity 1956). The methods accompanied in the
calculation of the precise lattice parameter of doped HA powder are shown in Table A-
VI (Appendix). Lattice parameters a (9.549 Å), c (6.994 Å) and unit cell volume V
(637.7 Å^3) of undoped HA, are obtained from Table A-I, Appendix. Lattice parameters
of doped HA are determined by applying the following relations

$$a = \frac{\lambda}{(3A)^{1/2}}$$ .... (5.1)

$$c = \frac{\lambda}{(4B)^{1/2}}$$ .... (5.2)

$$V = \frac{\sqrt{3}\,a^2 c}{2}$$ .... (5.3)

where λ is the X-ray wavelength (Cu-Kα=1.54 Å), A and B are attained by
solving the equations mentioned in Table A-VI (appendix) for doped HA (0.1 M Fe-
HA). A similar procedure has been followed to calculate the lattice parameters of
various other Fe doped HA. Lattice parameters, a and c of Fe-HA decrease successively
as the concentration of Fe^{3+} increases as shown in Figure 5.1(d) and results are
summarized in Table 5.1. It is observed that unit cell volume of undoped HA decreases
from 637.7 Å^3 to 622, 633, 625.05, 616.3, 633.9 Å^3 for 0.01, 0.02, 0.03, 0.04 and 0.05
M Fe-HA respectively. Debye-Scherrer's equation, $D = \frac{0.9\,\lambda}{\beta\cos\theta}$ is used to estimate the
crystallite size, where θ and β are the diffraction angle (°) and full width at half
maximum (in rad) respectively. Figure 5.1(e) indicates the increase in Fe incorporation
leads to a decrease in crystallite size. Upon the incorporation of Fe dopant, the
crystallite of HA decreased from 13.7 nm (undoped HA) to 12.2, 12.7, 11.8, 11.9, and
12.0 nm for 0.01, 0.02, 0.03, 0.04 and 0.05 M Fe-HA respectively. It is due to the
distortion caused by differences in the ionic radius of dopant (Fe^{3+}) and replaced
elements (Ca^{2+}). A very similar trend has been found in the theoretical study. It is
observed that a significant volume reduction from 2 % to 6 % of the system occurs due
to a replacement of 10 % to 20 % of Ca in the unit cell.
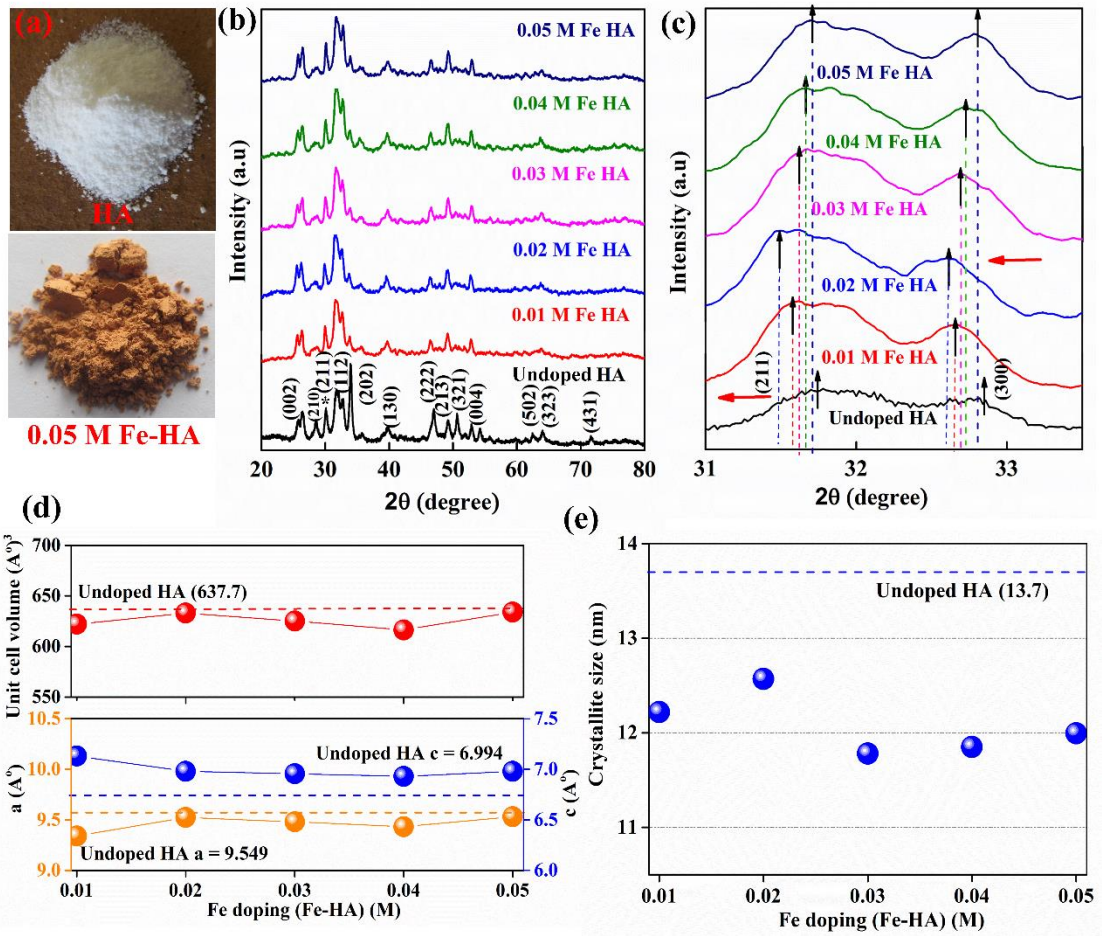
Figure 5.1: (a) Optical images of HA (white) and 0.05 M Fe-HA (brown) powders (b) XRD pattern of 0.01, 0.02, 0.03, 0.04 and 0.05 M Fe-HA (*: $CaHPO_4$), (c) exaggerated view of XRD peaks (211), (112) and (300). (d) Change in lattice parameters, lattice volume and (e) crystallite size as a function of Fe doping. Dash lines represent the undoped HA.

The FTIR and Raman spectra of undoped HA and Fe-HA with five different doping concentrations are shown in Figure 5.2. The FTIR spectra in Figure 5.2 (a) shows negligible difference between undoped 0.01, 0.02, 0.03, 0.04 and 0.05 M Fe-HA. The significance of the FT-IR spectra is to detect PO_4^{3-} and OH^- adsorption bands present in hydroxyapatite structure.

Table 5.1. X-ray diffraction parameters of undoped and doped hydroxyapatite

Sample	Values of A	Values of B	Lattice parameter 'a' (Å)	Lattice parameter 'c' (Å)	c/a	Volume (Å)³
Undoped HA	0.0086	0.0122	9.549	6.994	0.73243	637.736
0.01 M Fe-HA	0.0090	0.0116	9.343	7.13	0.76332	621.989
0.02 M Fe-HA	0.0086	0.0121	9.523	6.98	0.73296	632.998
0.03 M Fe-HA	0.0087	0.0120	9.48	6.955	0.73365	625.048
0.04 M Fe-HA	0.0088	0.0123	9.453	6.925	0.7347	616.335
0.05 M Fe-HA	0.0086	0.0121	9.53	6.98	0.73242	633.95

The intense characteristic peaks at 585 and 1055 cm^{-1} are ascribed to phosphate groups (PO_4^{3-}). Similarly, peaks between 1389 and 1426 cm^{-1} are due to carbonate groups (CO_3^{2-}) and broad peaks at 3454 cm^{-1} and 1587 cm^{-1} are attributed to OH$^-$ stretching and OH bending respectively. Raman spectra of undoped 0.01, 0.02, 0.03, 0.04 and 0.05 M Fe-HA are shown in Figure 5.2 (b) and Table 5.2. The P-O active modes at 430 cm^{-1} (v_2 PO_4^{3-}), 585 cm^{-1} (v_4 PO_4^{3-}) and 953 cm^{-1} (v_1 PO_4^{3-}) are observed in Fe-HA samples. Fe^{3+} (ionic radius = 0.64 Å) substitutes the Ca (II) (ionic radius = 0.99 Å) sites (Araujo et al. 2010), which has its bonding position surrounded by PO_4^{3-} and OH$^-$. Undoped HA has a peak at 1084.4 cm^{-1} (v_3 PO_4^{3-}) whereas, the peak shifts to 1033 cm^{-1} for Fe-HA (Table 5.2). The Raman spectrum agrees with the study that the phosphate bonding increases at 1033 cm^{-1} (v_3 PO_4^{3-}) with Fe concentration in HA. Fe incorporation in HA causes a perturbation in the hexagonal structure. Kim et al. observed a similar trend of increasing intensity and peak shifts in Zn^{2+} substitution in hydroxyapatite (Kim et al. 2018).

The specific surface area of undoped HA and Fe-HA were measured using the BET method with nitrogen adsorption/desorption and tabulated in Table 5.3. The average particle sizes are estimated using the formula (assuming spherically shaped) reported in the experimental section.

Table 5.2: A summary of Raman spectroscopic analysis of undoped HA and Fe-HA

Functional/ Vibrational groups	Raman shifts (cm⁻¹)		Assignment
	As-synthesised HA	Fe-HA	
υ_1 PO_4^{3-}	960	953	(Stretching mode) symmetric vibrational mode of P–O
υ_2 PO_4^{3-}	429	430	doubly bending mode
υ_3 PO_4^{3-}	1084.4	1033	triply generate antisymmetric Stretching mode
υ_4 PO_4^{3-}	590	585	triply degenerate bending mode
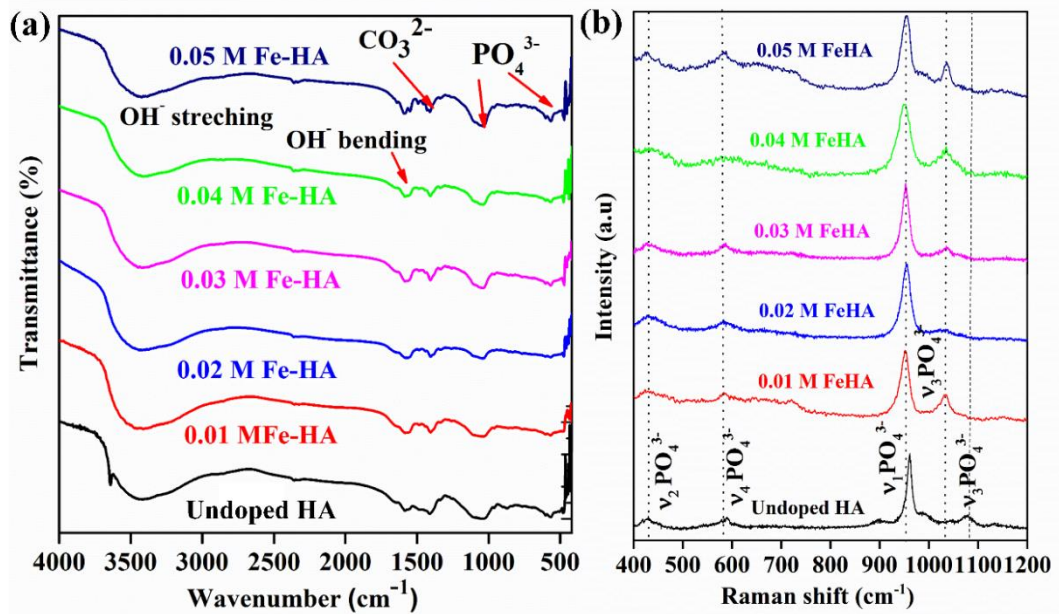
Figure 5.2: Spectral comparison between undoped and doped HA powders. (a) FTIR and (b) Raman spectra of undoped, 0.01, 0.02, 0.03, 0.04 and 0.05 M Fe-HA.

It is observed that surface area varied from ~21.34 - 49.80 m^2/gm and particle size from 37.9 – 88.4 nm as the Fe concentration increases (Table 5.3). With the increase in Fe concentration crystallite size reduces, but particle size increases which may be due to the agglomeration of Fe- HA nanosized particles.

Table 5.3: A details of BET specific surface area, average particles size of undoped HA and Fe-HA powder

Sample name	BET surface area (m^2/gm)	Avg. particle size (nm)
Undoped HA	37.5	50.3
0.01 M Fe-HA	49.8	37.9
0.02 M Fe-HA	47.2	40.0
0.03 M Fe-HA	33.4	56.5
0.04 M Fe-HA	23.1	81.5
0.05 M Fe-HA	21.3	88.4

Figure 5.3 shows the SEM images of undoped, 0.01, 0.02, 0.03, 0.04 and 0.05 M Fe-HA powders. The morphology of Fe-HA powder is agglomerated as well; one can observe the more appearance of needle-like particles in all samples as shown (by the yellow-coloured arrows) in Figure 5.3 (a-e). Needle-like nanostructure and cluster of tiny particles with agglomeration are found in undoped hydroxyapatite analysis from TEM (Figure 4.6). Figure 5.3 also shows the EDX patterns with a consistent increment in iron content of 2.23 % in the 0.01 M Fe-HA to 3.88 % atomic percent in 0.05 M Fe-HA powder. Due to the incorporation of Fe, the Ca/P ratio changes from 1.53 to 1.4, whereas undoped hydroxyapatite exhibits a ratio of 1.67. The formation of calcium-deficient hydroxyapatite indicates a partial replacement of Ca^{2+} with Fe^{3+}, which is consistent with Kaygili et al (Kaygili et al. 2014). Undoped HA contains a trace amount of Na and Fe, because of its natural origin i.e. cuttlefish bone, which is confirmed through EDS and XPS.
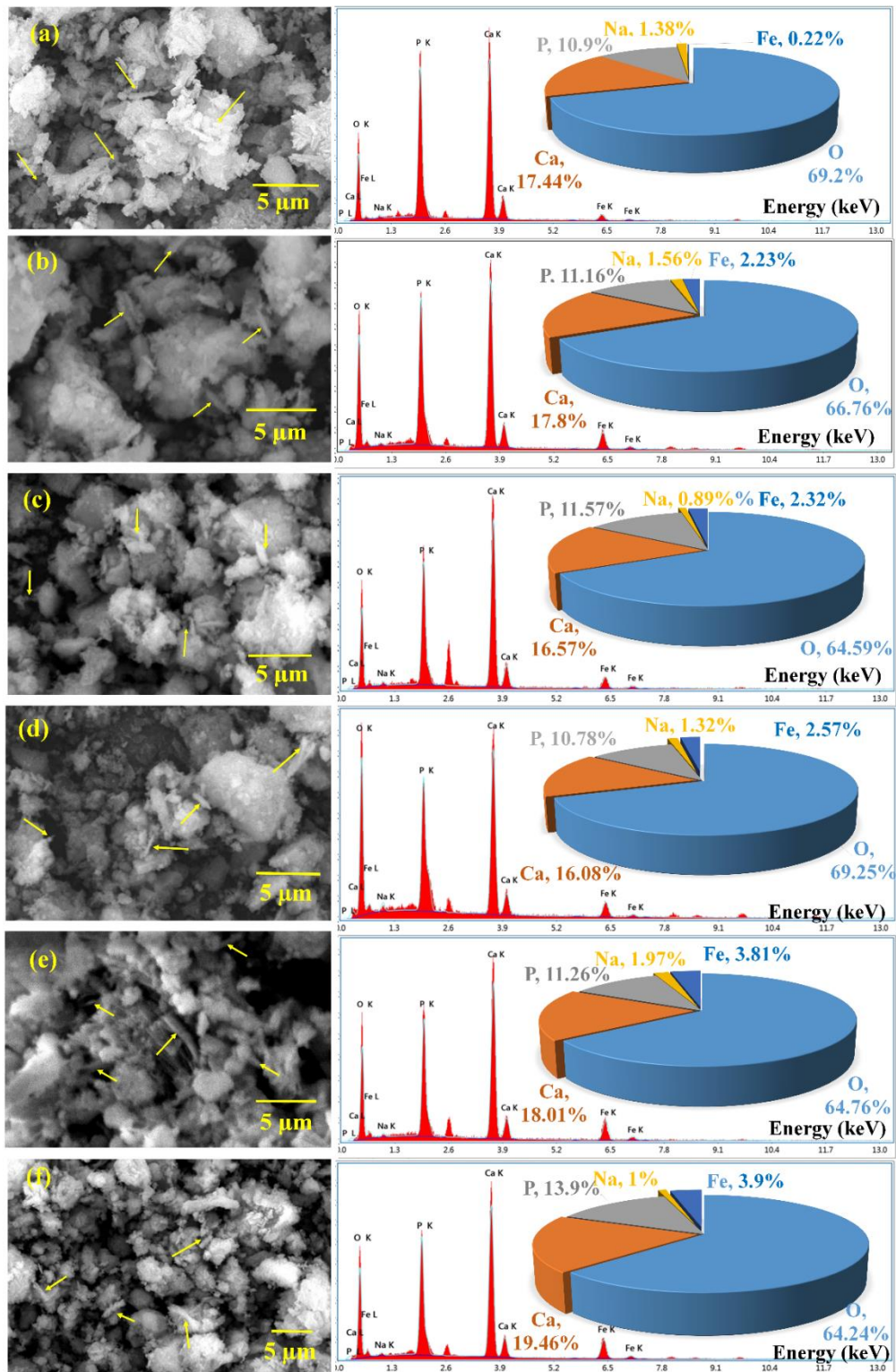
Figure 5.3: SEM images and corresponding area EDX analysis of (a) undoped (b) 0.01 M, (c) 0.02 M, (d) 0.03 M, (e) 0.04 M and (f) 0.05 M Fe-HA.

5.1.1 XPS analysis of Fe incorporated hydroxyapatite
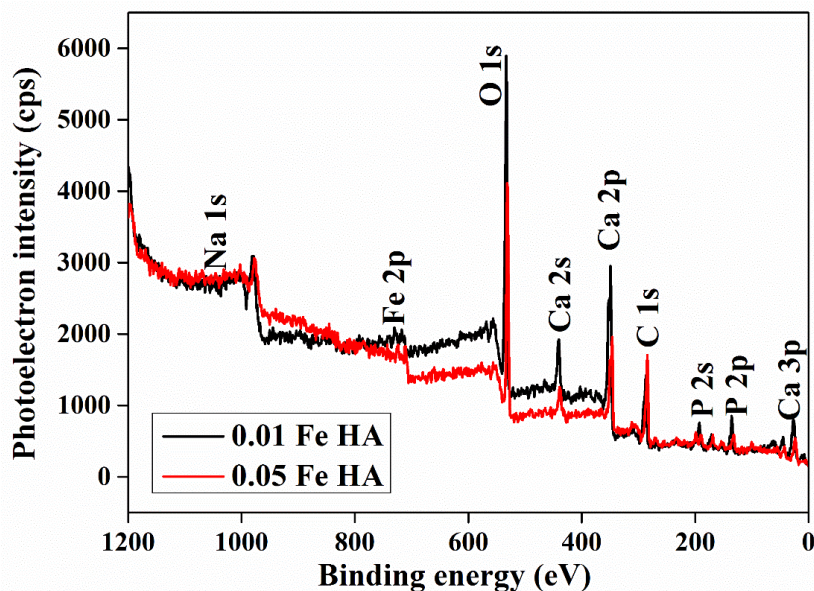
Figure 5.4. XPS survey spectra of 0.01 M Fe-HA and 0.05 M Fe-HA

XPS is used to analyse the elemental composition and their chemical states of Fe-HA. XPS survey spectrum of 0.01 M Fe-HA and 0.05 M Fe-HA exhibits C 1s, Ca 2p, P 2p, O 1s, Fe 2p, and Na 1s peaks as shown in Figure 5.4. XPS deconvolution spectra of Ca 2p, P 2p, O 1s and Fe 2p are depicted in Figure 5.5 and Figure 5.6 for 0.01 M Fe-HA and 0.05 M Fe-HA respectively. Figure 5.7 shows the high-resolution spectra of individual elements namely Ca, P, O and Fe with a comparison between 0.01 M and 0.05 M Fe-HA. The peak fit parameters of C 1s are reported in Table A-VII (Appendix).

In case of 0.01 M Fe-HA, binding energies of Ca 2p are 349.87 (2p $_{3/2}$), 351.42 (2p $_{1/2}$), 353.39 (2p $_{1/2}$) and 354.77 eV (2p $_{1/2}$) (Figure 5.5 (a)), whereas P 2p are designated with 133.96 (2p) and 137.23 eV (2p $_{3/2}$) (Figure 5.5 (b)). These specified elements (Ca 2p and P 2p) with binding energies are corresponding to $Ca_{10}(PO_4)_6(OH)_2$. O 1s with 533.85 eV (O 1s) is attributed to a phosphate group (P-O), 536.26 (O 1s) is related to P-O-P present in HA and high binding energy peak at 538.37 eV (O 1s) is a shake-up peak (Figure 5.5 (c)). Fe 2p with 713.08 eV (2p $_{3/2}$) is attributed to $FePO_4$, where Ca^{2+} is replaced by Fe^{3+} in HA structure which confirms the doping of Fe in HA. The peak at 717.20 eV (2p $_{3/2}$) is considered as shake-up peaks, which is a characteristic

86

of Fe^{3+} in Fe_2O_3. Peak at 727.22 eV (2p $_{1/2}$) is attributed to α- Fe_2O_3, and 733.80 eV (2p $_{1/2}$) is again shake-up peak (Figure 5.5 (d)).
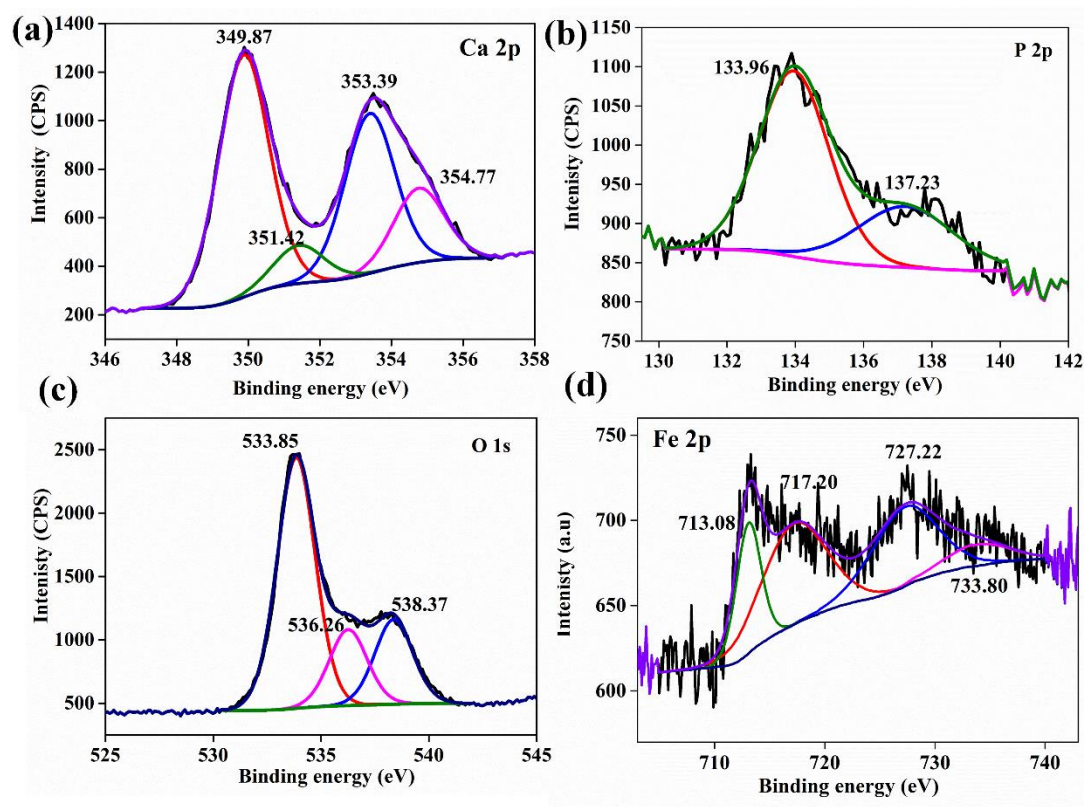
Figure 5.5: (a) Ca 2p, (b) P 2p, (c) O 1s and (d) Fe 2p XPS deconvolution spectra of 0.01 M Fe-HA

Similarly, in case of 0.05 M Fe-HA, binding energies of Ca 2p at 347.22 (2p $_{3/2}$), 348.70 (2p $_{3/2}$), 351.76 (2p $_{1/2}$), 350.62 (2p $_{1/2}$) eV and P 2p at 131.69 (2p), 132.76 (2p), 134.29 eV (2p) are attributed to calcium phase (Figure 5.6 (a)) and phosphate (Figure 5.6 (b)) group present in HA respectively. Peak at 531.25 (O 1s) eV, which is the contribution of a hydroxyl group (OH) present in $Ca_{10}(PO_4)_6(OH)_2$ (Figure 5.6 (c)). Binding energy at 533.47 eV corresponds to O 1s, which is attributed to P-O and 535.71 eV of O 1s is signifying to P-O-P bond of phosphate group present in HA. Likewise, Fe 2p found at binding energy 710.91 eV (2p $_{3/2}$) is in agreement with Fe_2O_3, which is not observed in 0.01 M Fe-HA due to less concentration of Fe. Again, Fe 2p at 714.02 eV (2p $_{3/2}$) is corresponding to $FePO_4$ in Fe HA (Figure 5.6 (d)). Considering the possible superposition of the main peak with a binding energy of 719.02 eV (2p $_{1/2}$) is

87

a shake-up peak of Fe 2p. Fe 2p with binding energy at 724.36 eV (2p $_{1/2}$) is corresponding to α- Fe_2O_3 and 730.15 eV (2p $_{1/2}$) is again a shake-up peak of Fe 2p (Figure 5.6 (d)). XPS spectral peak shift towards the left side due to a decrease in binding energies is observed with an increase in doping concentration (Figure 5.7). A decrease in binding energy is related to the chemical shifts due to the presence or absence of the chemical states of the element. Also, the difference in Fe^{3+} and Ca^{2+} electronegativities could be a cause for a reduction in the binding energies values (Abazović et al. 2009). A detailed XPS analysis of binding energies from survey scan and high-resolution deconvoluted spectra of elements of 0.01 M and 0.05 M Fe-HA is tabulated in Table 5.3.
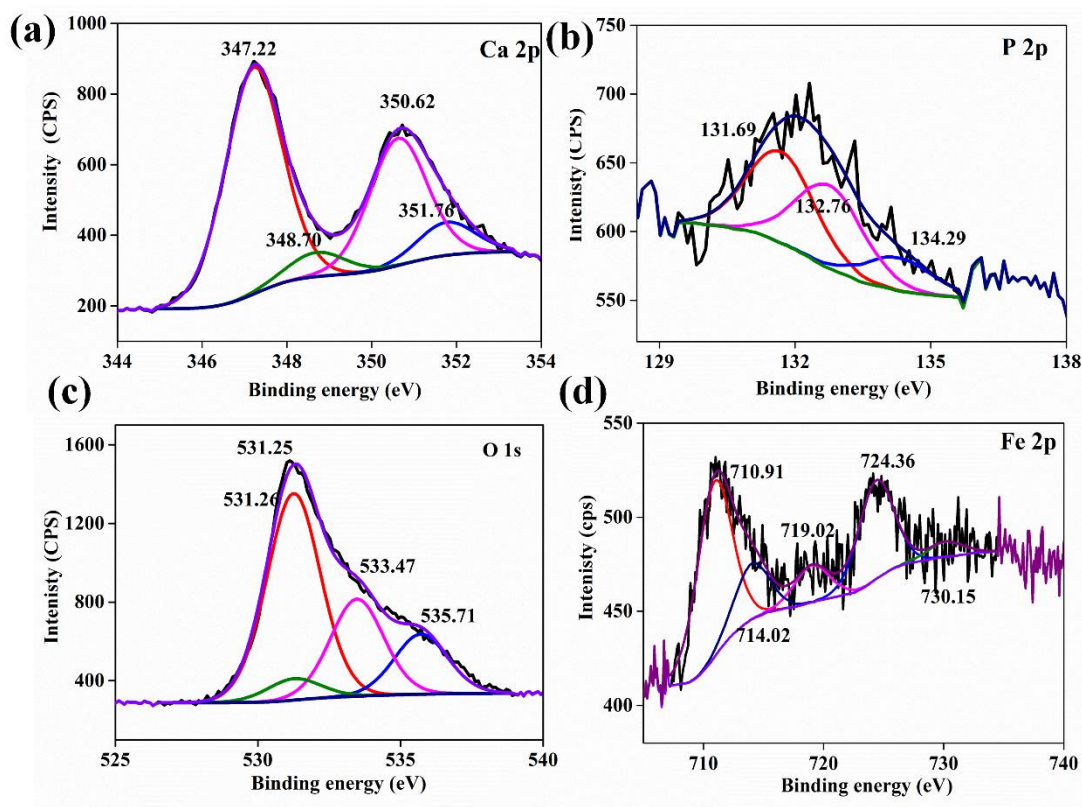
Figure 5.6: (a) Ca 2p, (b) P 2p, (c) O 1s and (d) Fe 2p XPS deconvolution spectra of 0.05 M Fe-HA
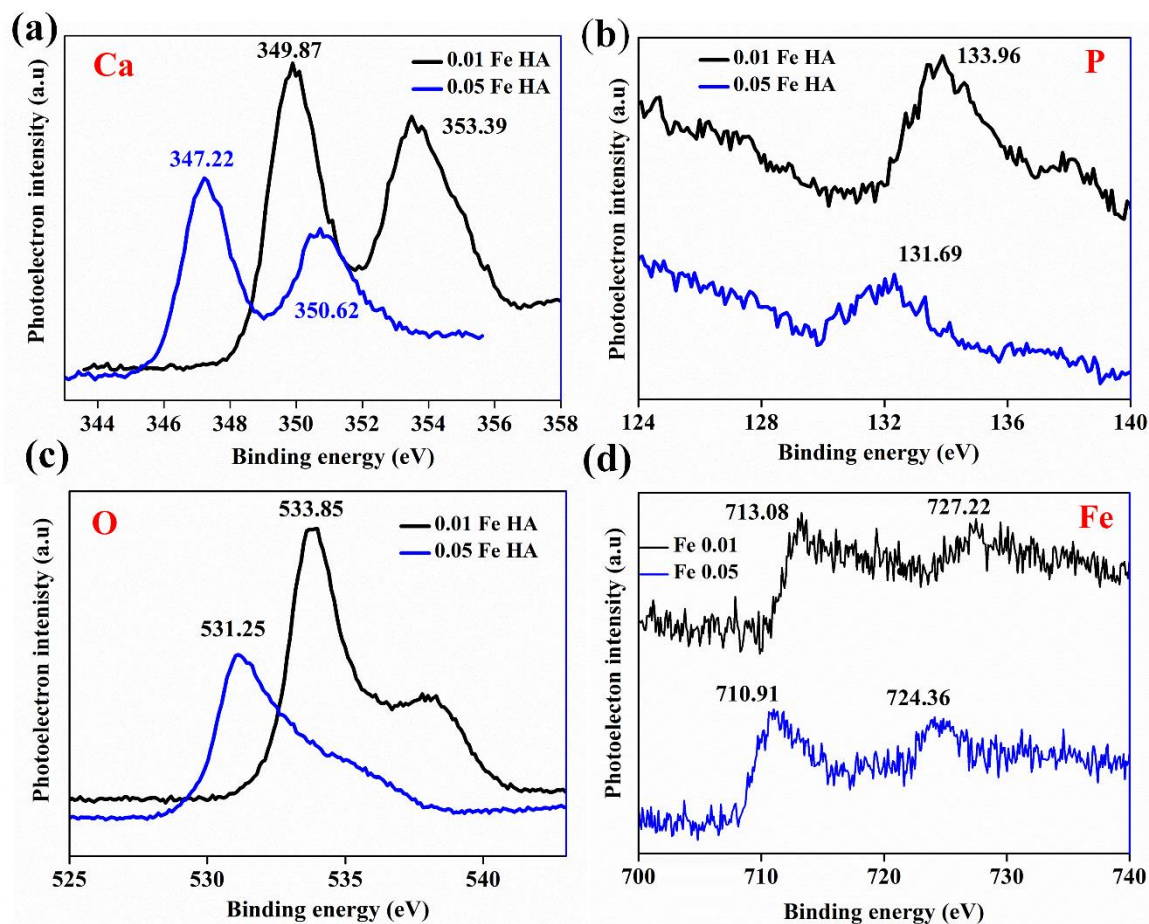
Figure 5.7: XPS high resolution spectra of 0.01 Fe HA and 0.05 Fe HA; (a) Ca, (b) P, (c) O and (d) Fe

5.2 UV-vis spectral assessment of undoped and Fe doped hydroxyapatite

UV–Vis absorption spectra of undoped HA and 0.01, 0.02, 0.03, 0.04 and 0.05 M Fe-HA are presented in Figure 5.8 (a). Fe-HA exhibits absorption from UV (200 nm – 400 nm) to region (300 nm – 700 nm), whereas undoped HA does not show any absorption in the UV-visible range. 0.05 M Fe- HA powder shows the highest absorption at 240 nm with considerable intensity tabulated in Table 5.4. The absorption band near 290 nm can be attributed to $^6A_1$ to $^4T_1(^4P)$ ligand field transition due to the incorporation of Fe(III). A strong UV absorption is observed because of the presence of Fe^{3+} ionic substitution in hydroxyapatite ($Ca_{10-x}Fe_x(PO_4)_6(OH)_2$). No detection of α-

Fe_2O_3 in XRD data, but traces of α- Fe_2O_3 were observed in XPS analysis, hence contribution from α- Fe_2O_3 is negligible for UV absorption.

Table 5.3: Details of XPS analysis of binding energies from survey scan and high-resolution deconvoluted spectra of elements

Elements	XPS binding energies (eV)		Peaks assignment
	0.01 M	0.05 M	
Ca 2p	349.87 (2p $_{3/2}$), 351.42 (2p $_{1/2}$), 353.39 (2p $_{1/2}$), 354.77 (2p $_{1/2}$)	347.22 (2p $_{3/2}$), 348.70 (2p $_{3/2}$), 351.76 (2p $_{1/2}$), 350.62 (2p $_{1/2}$)	Related to calcium phase on HA
P 2p	133.96 (2p), 137.23 (2p $_{3/2}$)	131.69 (2p), 132.76 (2p), 134.29 (2p)	Related to phosphate group in HA
O 1s	-	531.25 (O 1s)	Contribution of a hydroxyl group (OH)
	533.85 (O 1s)	533.47 (O 1s)	Phosphate group (P-O)
	536.26 (O 1s)	535.71 (O 1s)	Phosphate group (P-O-P)
	538.37 (O 1s)	-	Shake-up peak
Fe 2p	-	710.91 (2p $_{3/2}$)	Fe_2O_3
	713.08 (2p $_{3/2}$)	714.02 (2p $_{3/2}$)	$FePO_4$ (HA)
	717.20 (2p $_{3/2}$)	719.02 (2p $_{1/2}$)	Shake-up peaks *
	727.22 (2p $_{1/2}$)	724.36 (2p $_{1/2}$)	α- Fe_2O_3
	733.80 (2p $_{1/2}$).	730.15 (2p $_{1/2}$)	Shake-up peaks *
			*Characteristic of Fe^{3+} in Fe_2O_3

Table 5.4: A summary of size, shape and optical properties of 0.05 M Fe-HA powders

Sample	Particle size	Morphology	UV absorption	Band gap (eV)
0.05 M Fe-HA (Cuttlefish bone based HA)	~88 nm	Rod-like structure with a cluster of agglomerated tiny particles	UVA and UVB (Peak at 240 nm)	2.18
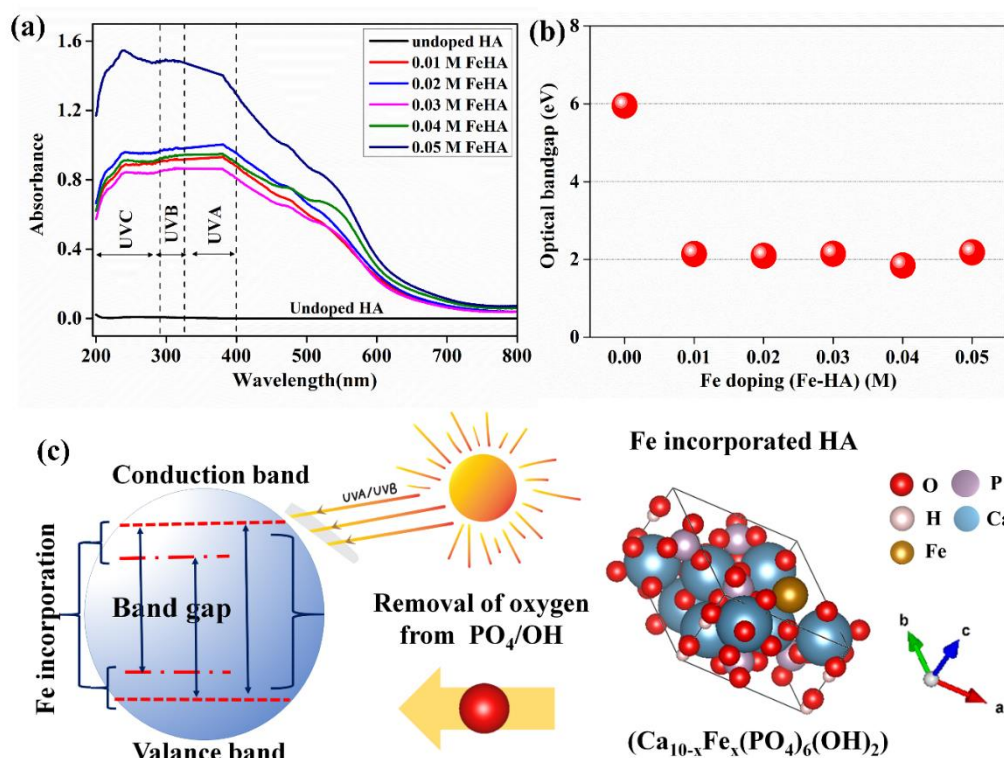
Figure 5.8: (a) UV-vis spectra of undoped HA and Fe-HA (0.01, 0.02, 0.03, 0.04 and 0.05M), (b) variation of optical bandgap as a function of Fe concentration, (c) Schematic representation of absorption of Fe-HA and a variation of bandgap due to the removal of oxygen and simultaneously the incorporation of Fe in HA during irradiation of UV light.

Fine particles in sunscreen filters (< 100 nm) are used to have more efficiency in UV absorption over an entire range including both UVA and UVB (Pal et al. 2020). Nanoparticle (< 100 nm) scatters UVB and UVA but permits visible light (370–720 nm) to penetrate, owing to Rayleigh scattering, as the intensity of scattered light depends on the wavelength and is directly proportional to particle radius. The inorganic oxides like TiO_2 lead to white coloration due to their high refractive index turn down the aesthetic worth of sunscreens. To defeat the whitening effect, nanoparticle (< 100 nm) is preferable active ingredients of sunscreen filters. In this study, Fe^{3+} substituted HA-based nano-structured ingredients, can offer better protection from harmful UV without any adverse effect on the skin (Piccirillo et al. 2014). HA is undoubtedly biocompatible and Fe is also proven to be less toxic than manganese and other metals (Piccirillo et al. 2014; Araujo et al. 2010). A considerable quantity of these blocking

components can protect the skin by absorbing radiation as well as by scattering. Piccirillo et al demonstrated the *in vivo* test of the acute irritant potential to check the skin tolerance of Fe-HA based sunscreen cream; no active compounds were found which could cause any irritant reaction or erythema formation (Piccirillo et al. 2014).

Figure 5.8 (b) shows that the narrowing down of optical bandgap is due to the substitution of Fe^{3+} ions in HA. The optical band gap of undoped HA obtained from the Tauc plot of UV absorption is found to be 5.95 eV, which is drastically fallen to 2.14, 2.08, 2.14, 1.84 and 2.18 eV for 0.01, 0.02, 0.03, 0.04 and 0.05 M Fe-HA respectively. The change in bandgap energy could be ascribed to a difference in the energy of Ca^{2+} in comparison to that of Fe^{3+} (Burns and Burns 1993). A summary of variation in band gap with respect to increasing Fe content is tabulated in Table 5.5. Atomic % of Fe in undoped and doped HA was obtained from EDS. If the dopant induced band is near to either the conduction or valence band edge resulted in a reduction in the bandgap. Dopants always create more allowed states near the band, which decreases the bandgap.

Table 5.5: A summary of variation band gap with respect to increasing in Fe content

Sample		Fe content (atomic %)	Band gap (eV)
Fe-incorporated hydroxyapatite	HA (undoped)	0.22	5.95
	0.01 M Fe-HA	2.23	2.14
	0.02 M Fe-HA	2.32	2.08
	0.03 M Fe-HA	2.57	2.14
	0.04 M Fe-HA	3.81	1.84
	0.05 M Fe-HA	3.9	2.18

The Fe-incorporated-HA becomes oxygen-deficient under the UV irradiation resulted in the modulation (reduction) of band gap (Figure 5. 8(c)). The oxygen from the system transfers to the atmosphere by releasing two electrons in the crystal according to the following equation (1).

$$O_o^x \leftrightharpoons V_o^{\cdot\cdot} + 2e^- + \frac{1}{2}O_2 \uparrow \ldots\ldots\ldots (5.4)$$
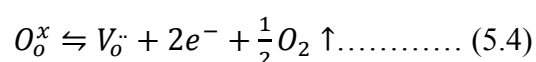
The possible sites for the oxygen vacancy in HA crystal (OH-, PO_4^{3-}, and PO_4^{3-} + OH^-) contribute to the reduction in the bandgap (Bystrov et al. 2016). From the crystal

field theory in the hexagonal system, Fe^{2+} is comparatively unstable due to the loss of d^6 electronic order, which tends to oxidization to form Fe^{3+} (d^5). Hence, the oxidation process transfers an electron to the surface of adsorbed O_2. The Fe^{3+} ions can be a potential electron trap, which can even act as hole traps to promote the further formation of Fe^{2+} and Fe^{4+}. Fe^{4+} acts as a hole trap followed by the reaction with a surface hydroxyl group (OH^-) to form a respective radical ($^{\cdot}OH$), which recombines with mobile electrons to form Fe^{3+}. Although most of the Fe atoms in HA crystal exist in the Fe^{3+} state, both Fe^{2+} and Fe^{3+} could play a role as recombination centers for the electron-hole pair. As the redox reactions proceed, the availability of hole traps is reduced because of the decrease in Fe^{3+} concentration, whereas surplus Fe^{3+} acts again as recombination center. Therefore, Fe^{2+} and Fe^{3+} ions take part in the cyclic process, resulted in a substantial reduction of the bandgap (Han et al. 2019).

5.3 Computational assessment of Fe incorporated hydroxyapatite

To have a clear understanding of the band energies and the formation of the trap states, electronic structure calculations have been performed. HA exists in a hexagonal structure (space group $P6_{3/m}$) which is consisting of 44 atoms per unit cell with lattice parameters a = b ≠ c and α = β = 90°, γ = 120°. The optimized lattice parameters from our DFT calculations are a = b = 9.55 Å and c = 6.94 Å, which are in well agreement with the earlier reported experimental values.

To understand the interactions of electrons in the valence band of HA and the effect of Fe doping on the electronic properties of HA, the band structure and density of states of undoped HA and Fe-doped HA are calculated, which are shown in Figure 5.9 (a) and Figure 5.9 (b) respectively. In the doped system, 10 atomic % of Ca was replaced with Fe in the unit cell. To compare the change in the electronic band structure, the valence band maximum of both the system is set as 0 eV. The calculated PBE band gap of undoped HA is 5.9 eV, which is consistent with the experimentally reported value. When the transition metal Fe is substituted into HA, the bandgap is significantly decreased as shown in Figure 5.9 (b), which is mainly due to the new energy states of Fe d character introduced at the top of the valence band owing to the interaction in between 3d energy states of iron and 2p states of oxygen.
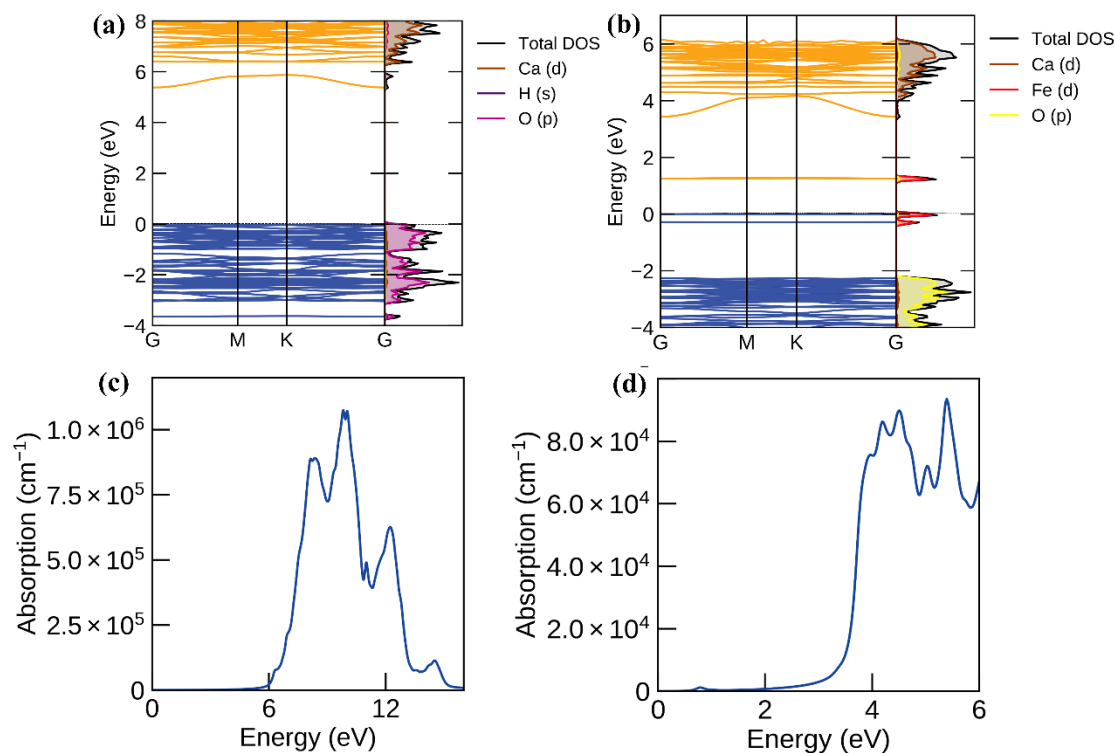
Figure 5.9: Calculated band structures, atom projected density of state plots of (a) undoped HA and (b) Fe-HA. Absorption coefficient plots of (c) undoped HA and (d) Fe-HA.

Next, calculation of the frequency dependent dielectric function was performed applying density functional perturbation theory on top of the ground state electronic structure. The optical properties of the system are then obtained from the complex dielectric function. Figure 5.9 (c) and (d) represent the calculated absorption coefficient of the considered HA and Fe-HA. The materials show a high absorption coefficient with a maximum absorption obtained with HA. Absorption is strong (above 10^5 cm^{-1}) for energies above 6 eV in the undoped HA, while in the case of Fe-HA, strong absorption occurs with comparatively much lower energy (~ 3.8 eV). A natural origin (biogenic) HA with Fe^{3+} substitution in it proves its potentiality in replacing conventionally available products such as ZnO and TiO_2, in the field of sunscreen filters. As the non-toxic nature of HA; in fact, HA is present in great amounts in human anatomy; hence, it is a completely biocompatible material used predominately in biomedical applications. Fe-HA can be a promising additive in cosmetic products as it provides complete UV protection over the entire range of UVA and UVB.

5.4 Conclusions

In this chapter, in depth study of structural, morphological, elemental spectral analysis verifies the incorporation of Fe in HA. The particle size was estimated from the BET method to ensure the nanostructure of Fe-HA. The optical property of Fe-HA is found to be of greater importance as the absorption spectra of Fe-HA powder cover the entire UV and visible range with maximum absorption at 240 nm. The optical band gap of undoped HA (5.95 eV) is drastically fallen to 2.14, 2.08, 2.14, 1.84 and 2.18 eV for 0.01, 0.02, 0.03, 0.04 and 0.05 M Fe-HA respectively, which can be attributed to a difference in the energy level of Fe^{3+} in comparison to that of Ca^{2+}. The results obtained with DFT calculations are in good agreement with experimental data. It ensures proper coverage of the harmful UVB (290 - 320 nm) and UVA (320 – 400 nm) to protect human skin. Especially, HA is derived from natural origin, free of toxicity or chemical reactivity; hence ion exchange processed Fe-HA can have a potential application as an active UV absorbing material of sunscreen filters.

Page left intentionally blank

CHAPTER 6

Exploration of prawn exoskeleton as natural protection from UV radiation

In this study, a comprehensive study on the prawn (*Fenneropenaeus indicus*) (Figure 6.1) exoskeleton (shell) has been exploited to recognize the nature of the composite consisting of chitin-proteins as matrix phase, regular spherical shaped calcite (CaCO₃) and nanoscopic proteins as disperse phase. The thermal analysis was performed to get clear information of compositional aspects of the exoskeleton, a compositional mapping was executed from the thermal analysis. A range of UV absorption studies was correlated with crystal, microstructural and elemental analysis using X-ray diffraction, Fourier-transform infrared spectroscopy, scanning electron microscopy, energy-dispersive X-ray spectroscopy and X-ray photoelectron spectroscopy.

Figure 6.1: Optical photograph of prawn (*Fenneropenaeus indicus*)

6.1 Structural, thermal and morphological assessment of prawn exoskeleton

Figure 6.2 (a) shows the XRD patterns of the prawn shell as collected and annealed at 500 ˚C and Table 6.1 reveals the list of compounds available in prawn exoskeleton with their planes. As collected shell is mainly composed of α-chitin and calcite. α-chitin at peak positions and their corresponding planes are 19.4˚ (110), 21.2˚ (120) and 23.7˚ (130) (Jang et al. 2004) and calcite peaks are observed at 29.38˚ (104), 35.96˚ (110), 39.4˚ (11$\bar{3}$), 47.56˚ (018), 48.5˚ (11$\bar{6}$) with ICDD**:**00-047-1743. When

the shell was annealed at 500 °C, organic matter was decomposed and burned out, pure calcite was left out appeared as peaks in XRD.
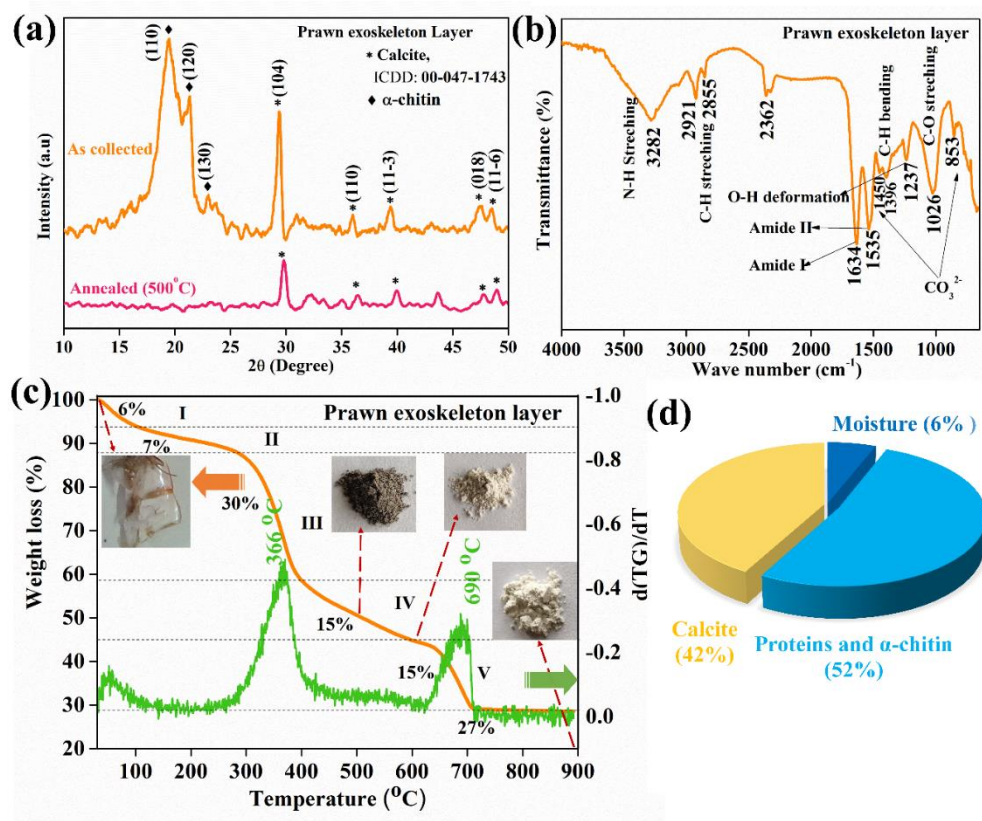
Figure 6.2: Structural and thermal assessment of the prawn shell. (a) X-ray diffraction pattern of as-collected and annealed (500 °C) shell. (b) FTIR spectrum, (c) TGA plot and (d) a complete compositional (weight %) picture of prawn shell drawn from TGA.

FTIR spectrum of prawn shell is shown in Figure 6.2(b), it specifies the presence of characteristic bands of respective components present in the shell (Table 6.1), namely calcite, α-chitin and proteins. The broad characteristic peak around 3282 cm^{-1} corresponds to N-H stretching, which is due to the presence of α-chitin and an amino acid group of proteins (Ghimire et al. 2017). The characteristic bands at 2921 cm^{-1} and 2855 cm^{-1} indicate the stretching vibration of methyl C-H bond of acetyl groups presence in α-chitin and proteins. The peaks at 1634 cm^{-1} and 1535 cm^{-1} belong to amide I (C=O stretching) and amide II (N-H bending) respectively present in α-chitin and proteins. Also, characteristic bands at 1396 cm^{-1} (C-H bending) and 1237 cm^{-1} (O-H deformation) belong to α-chitin and proteins, and 1026 cm^{-1} (C-O stretching)

belongs to calcite (Ghimire et al. 2017). Likewise, calcite characteristic bands at 1450 cm^{-1} and 853 cm^{-1} are attributed to the presence of CO_3^{2-} (Zhou, Ge, Fan, & Xia, 2018).

Table 6.1: A summary of the structural characterization of prawn shell.

Name of the materials	XRD (2θ and Planes)	FTIR (cm^{-1})
Calcite (CaCO$_3$)	29.38˚ (104), 35.96˚ (110), 39.4˚ (11$\bar{3}$), 47.56˚ (018), 48.5˚ (11$\bar{6}$)	1450 (CO$_3^{2-}$) 1026 (C-O stretching) 853 (CO$_3^{2-}$)
α-Chitin (C$_8$H$_{13}$O$_5$N)	19.4˚ (110), 21.2˚ (120) and 23.7˚ (130)	3282 (N-H stretching), 2921 & 2855 (C-H stretching in acetyl group), 1634 (Amide I), 1535 (Amide II), 1396 (C-H bending) and 1237 (O-H deformation)
Mycosporine-like amino acids (tryptophan, phenylalanine and tyrosine)	-	3282 (N-H stretching), 2921 & 2855 (C-H stretching in acetyl group), 1634 (Amide I), 1535 (Amide II), 1396 (C-H bending), 1237 (O-H deformation)

Figure 6.2(c) shows the weight loss versus temperature profile of prawn shells from the thermal analysis, the entire weight loss profile is divided into five evaporation/decomposition stages from stage I to stage V (Table 6.2). The prawn shell is consisting of calcite, α-chitin and proteins. In stage I, the interval between 30 ℃ and 100 ℃, which is attributed to the evaporation of water with a weight loss of ~ 6 %. In stage II, the temperature ranges from 100 - 290 ℃ with weight loss of ~ 7 % are due to the removal of water and deproteinization (Zhou et al. 2018). In stage III, a significant weight loss of ~ 30 % is observed in between 290 °C and 400 °C, the peak at 366 °C is corresponding to the weight loss with respect to the (a) degradation of the saccharide structure of the molecule present in α-chitin fibre, including the dehydration of saccharide rings and (b) decomposition of the α-chitin (Ospina et al. 2014). In stage IV, temperature ranges from 400 °C – 595 °C is associated with a weight loss of ~ 15 %, because of the complete decomposition of the α-chitin (Ospina

et al. 2014). Finally, in stage V, 595 °C – 710 °C is resembling the calcination of calcite to CaO (weight loss ~ 15 %) with an intense peak at 690 °C, therefore, 27 % of residual mass as CaO remains constant even after heating up to 900 °C (Zhou et al. 2018). A complete compositional picture of prawn shell drawn from TGA presented in Figure 6.2(d) contains 6 % of moisture, 42 % of calcite and the remaining 52 % of organic matter, includes α-chitin and proteins; well match with reported literature (Knorr 1984).

Table 6.2: A summary of the weight loss profile of prawn shell from TGA.

Stage	Temperature interval (°C)	Weight loss (%)	Reasoning
I	30 - 100	6	Removal of water
II	100 - 290	7	Removal of water, deproteinization
III	290 - 400	30	Deproteinization, the degradation of the saccharide structure presence in α-chitin and decomposition of the α-chitin
IV	400 - 595	15	decomposition of the α-chitin
V	595 - 710	15	Calcination of $CaCO_3$

The prawn shell surface and cross-sectional morphological analysis by SEM and elemental identification by EDAX are reported in Figure 6.3. The optical photograph of a prawn (*Fenneropenaeus Indicus*) and dried shells are shown in Figure 6.3(a). Topological SEM image shows that regular spherical shaped calcites (0.74 ± 0.154 μm) are embedded into α-chitin/protein matrix (Figure 6.3(b)). Elemental analysis is shown in Figure 6.3(c) confirms the presence of Ca and P along with a trace amount of Mg in prawn shells (Hansen and Illanes 1994). The presence of Ca is found in the form of calcite and calcium phosphate, whereas P is attributed to calcium phosphate (Hansen and Illanes 1994). A uniform distribution of Mg and Ca is observed on topological surfaces, as shown in Figure 6.3(d) and Figure 6.3(e) respectively. The layered structures of prawn shells are observed in cross-sectional SEM image (Figure 6.3(f)). Prawn exocuticle is appeared by white colour in cross sectional SEM, are rich with calcium as shown in Figure 6.3(g). In the elemental
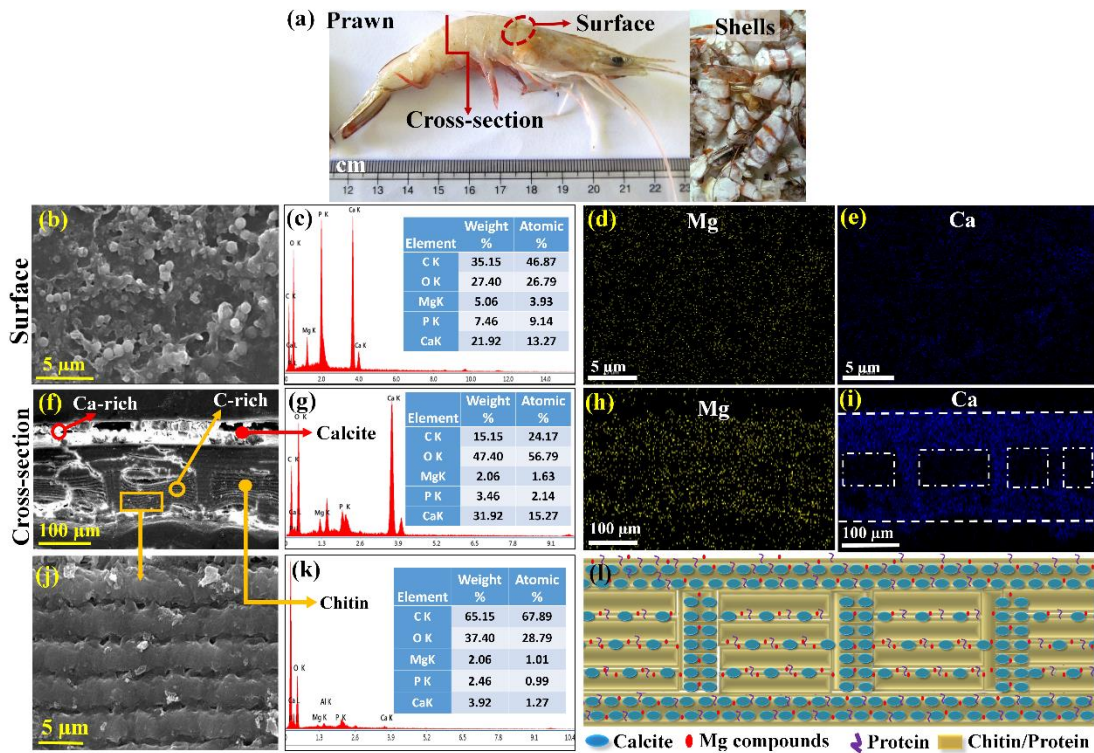
Figure 6.3: Prawn exoskeleton surface, cross-section morphology and their compositional analysis. (a) Optical photograph of prawn and shells, (b) topological SEM image of shell's surface with corresponding (c) EDAX, (d, e) elemental mapping of Mg and Ca. (f) SEM image of a cross-sectional view of a shell with (g) corresponding EDAX, (h, i) elemental mapping of Mg and Ca in the cross-sectional view, (j) a magnified view of SEM image and (k) corresponding EDAX, (l) Schematic representation of the cross-sectional view of the prawn shell.

mapping, it is observed that the non-uniform distribution of Ca and Mg (Figure 6.3(h) and (i)) in the discontinuous chitin-protein rich endocuticle. A high-resolution version of layered structured prawn shell exhibits the stacking (Figure 6.3(j)) and corresponding EDAX analysis reveals the C-rich nature of endocuticle (dark colour) layer (Figure 6.3(k)). Exocuticle and endocuticle layers with thicknesses of 33 ± 3.1 μm and 80 ± 3 μm, respectively are stacked sequentially. The top and bottom exocuticle are enriched with Ca, whereas a C-rich endocuticle consisting of bouligand structure of chitin-protein multilayer (Raabe et al. 2005), is there in between. The

101

individual layer of chitin protein in the multi-layered bouligand structure is around 2.6 ± 0.07 μm. Also, the chitin-protein rich endocuticle is found to be surrounded by Ca-rich exocuticles. Figure 6.3 (l) shows the schematic illustration of the cross-sectional view of the prawn shell. The organic matrix which are composed of chitin-protein fibers is embedded in regular spherical calcite particles (0.74 ± 0.154 μm). The organic matrix and chitin-protein fibers facilitate the branched twisted woven networks (Raabe et al. 2005). In between the top and bottom exocuticle layer, discontinuous endocuticle consists of multilayer stacking of chitin-protein fibers; spherical shaped calcite particles are also dispersed in between the successive multilayers. Mg compounds are distributed as trace elements throughout the shell. Meanwhile, nanoscopic proteins may be dispersed in the entire prawn exoskeleton (Ibrahim et al. 1999).

6.1.1 XPS analysis of prawn exoskeleton

XPS investigation is carried out on the prawn exoskeleton to recognize the elements present along with their chemical states. The wide survey spectrum reveals the presence of peaks of C 1s (284.9 eV), O 1s (530.54 eV), Mg (1302.9 eV), P 2p (133.08 eV), Na 1s (1070.38 eV) and N 1s (399.48 eV) in prawn exoskeleton as shown in Figure 6.4.

Figure 6.4: XPS survey of spectrum of prawn shell

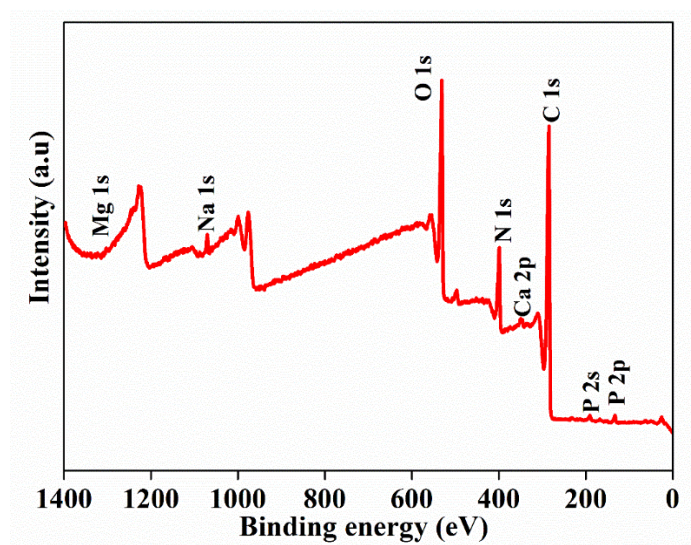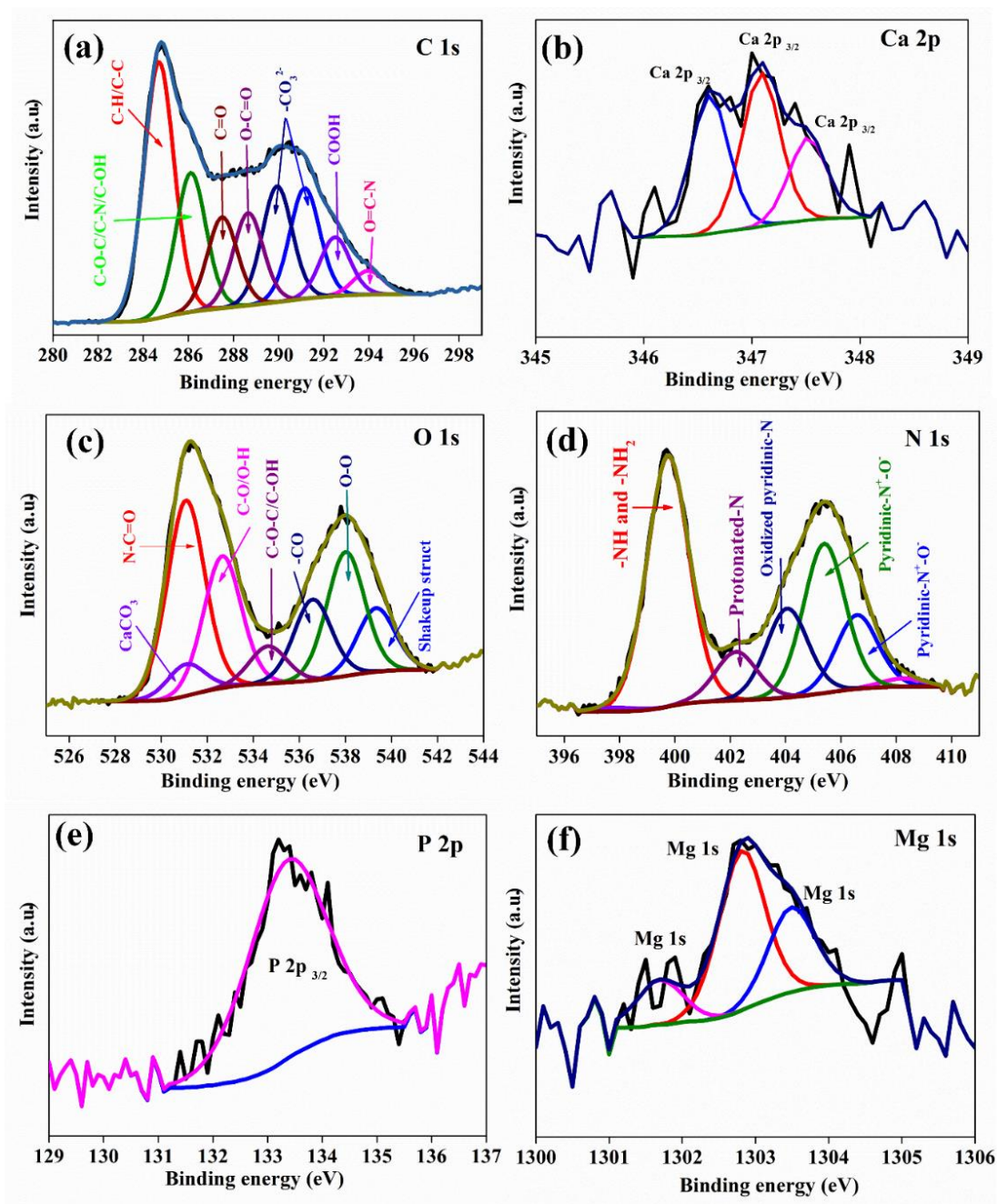Figure 6.5: XPS investigation reveals the surface chemistry of the prawn exoskeleton. XPS deconvoluted high-resolution spectra of (a) C 1s, (b) Ca 2p, (c) O 1s, (d) N 1s, (e) P 2p and (f) Mg 1s.

XPS survey of deconvoluted high-resolution spectra of (a) C 1s, (b) Ca 2p, (c) O 1s, (d) N 1s, (e) P 1s and (f) Mg 1s are shown in Figure 6.5. The high-resolution spectra of C 1s deconvoluted peaks are plotted in Figure 6.5 (a) with tabulated peak fitting parameters in Table A-VIII (Appendix). The dominant peak of C 1s at 284.68 eV binding energy is due to the presence of aliphatic carbon (C-H/C-C), a second peak at 286.2 eV is corresponding to C-O-C/C-N/C-OH linkage present in both α-chitin and protein molecule. Binding energies at 287.55 eV correspond to the C=O bond, which is assigned to the specific part of α-chitin and protein molecules (Feng et al. 2018; Wu et al. 2019). Binding energies at 288.65 eV (O-C=O) correlates to the presence of protein molecules (Feng et al. 2018; Wu et al. 2019). Again, binding energies at 289.96 eV (Sosulnikov and Teterin 1991) and 291.19 eV (Shinoda et al. 1994) belong to carbonate ions (CO_3^{2-}) of calcite. Similarly, binding energies, 292.5 eV and 293.87 eV attribute to COOH and O=C-N, respectively present in chitin/protein (Ieva et al. 2009). The fractional area of C due to the existence of calcite is lesser than the area fraction of C corresponds to α-chitin and protein; indicates the abundance of α-chitin-protein content in prawn shell. In summary, the chemical bonds of C-H, C-OH, C-N, C-O-C are representing α-chitin ($C_8H_{13}O_5N)_n$ and a range of different protein molecules present in the shell. Figure 6.5(b) shows the deconvoluted high-resolution spectra of Ca at a binding energy of 346.6 eV (Järvinen et al. 2014) belongs to Ca-O, whereas 347.1 eV and 347.5 eV (Sosulnikov & Teterin, 1991) corresponds to $CaCO_3$. High-resolution spectra of O 1s deconvoluted peaks are shown in Figure 6.5(c), binding energies at 531.1 eV (N-C=O) and 532.7 eV (C-O/OH) belong to α-chitin. Again, peaks at 536.7 eV (–CO) are due to the carboxylic groups (C-O) present in proteins (Feng et al. 2018). O 1s binding energy at 531.1 eV belongs to $CaCO_3$ (Christie et al. 1983), whereas the peak at 538.1 eV (O-O) signifies O^{2-} (Yuan et al. 2015). Likewise, O 1s peak at 534.61 eV (C-O-C/C-OH) corresponds to organic compounds (α-chitin/protein), and higher binding energies at 539.29 eV corresponds to unsaturated and aromatic functionalities in organic compounds appeared as shakeup peaks. Figure 6.5(d) shows the deconvoluted high-resolution spectra of N 1s, binding energy at 399.8 eV represents –NH and –NH_2 domains of α-chitin and proteins. The binding energy at 402.2 eV attributes to protonated-N and peak at 404.05 eV indicates the presence of oxidized pyridinic-N; both are belonging

to aromatic rings of mycosporine-like amino acids, a complex amino acid with the central aromatic ring (Yuan et al. 2015). Also, N 1s peaks found at 405.4 eV, and 406.5 eV resemble the pyridinic-N$^+$- O$^-$, which is produced during the regeneration process of chitin/protein. The pyridinic-N can be defined as an N atom in an aromatic ring, where N forms bonding with two C atoms on the edge of a C plane. Pyridinic-N contributes one p-electron to the aromatic π system and has a lone pair electron in the carbon matrix. Deconvoluted high-resolution spectrum of P 2p is shown in Figure 6.5(e), binding energy at 133.47 eV corresponds to phosphate groups of calcium phosphates present in prawn shells. Similarly, Mg 1s is shown in Figure 6.5(f) with binding energies of 1302.8 eV (Mg(OH)$_2$), 1301.7 eV (MgO) and 1303.5 eV (MgO), where a ratio of Mg(OH)$_2$: MgO $\equiv$ 1.8: 1 is maintained. Table 6.3 provides the details of the XPS survey scan to identify the elements present and their respective binding energies from high-resolution deconvoluted spectra. Three unique positions of binding energies, 288.65, 402.2, 404.05 eV are attributed to O-C=O, protonated-N and oxidized pyridinic-N, respectively, which signify the presence of mycosporine-like amino acids, namely tryptophan (C$_{11}$H$_{12}$N$_2$O$_2$), phenylalanine (C$_9$H$_{11}$NO$_2$), tyrosine (C$_9$H$_{11}$NO$_3$) etc.

Table 6.3: A summary of XPS survey of elements with corresponding binding energies from high-resolution deconvoluted spectra

Name of the material	XPS binding energies (eV)				UV-visible (nm)
	C 1s	O 1s	N 1s	Ca 2p	
Calcite (CaCO$_3$)	289.96 & 291.19 (CO$_3^{2-}$)	531.1 (C-O)	-	346.6, 347.1 & 347.5 (Ca^{2+} in CaCO$_3$)	-
α-Chitin (C$_8$H$_{13}$O$_5$N)	284.68 (C-H/C-C) 286.2 (C-O-C/C-N/C-OH) 287.55 (C=O)	531.1(N-C=O)	399.8 (–NH)	-	-
Mycosporine-like amino acids (tryptophan, phenylalanine and tyrosine)	288.65 (O-C=O) 284.68 (C-H/C-C) 286.2 (C-O-C/C-N/C-OH) 287.55 (C=O/C=N)	532.7 (C-O/OH) 536.7 eV (–CO)	399.8 (-NH$_2$ and -NH) 402.2 (protonated-N) 404.05 (oxidized pyridinic-N)	-	~290, 320

6.2 UV-vis spectroscopic analysis of prawn exoskeleton
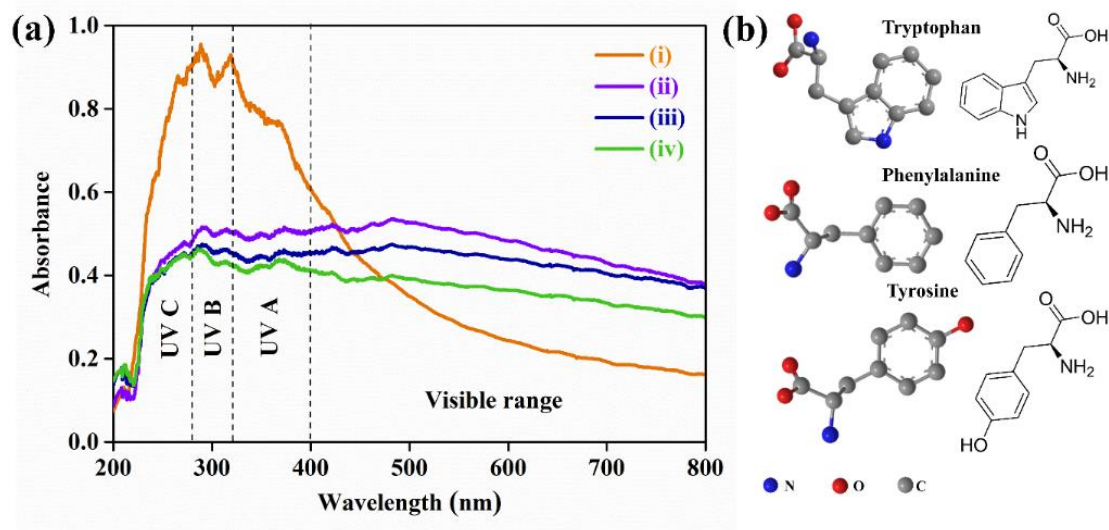
Figure 6.6: Prawn exoskeleton exhibits wide absorption over UV irradiation in the range of 200 - 400 nm. This is attributed to the presence of mycosporine-like amino acids (tryptophan, phenylalanine and tyrosine). (a) UV-visible spectra of the prawn shell (i) as-collected and shell annealed at (ii) 500 °C, (iii) 600 ºC and (iv) 900 ºC. (b) Schematic representation of the chemical structure of tryptophan, phenylalanine and tyrosine.

UV-visible spectra of prawn shells as collected and annealed at 500, 600 and 900 °C are shown in Figure 6.5(a). It is observed that the as-collected prawn shell (Figure 6.6(a).i) shows broad absorbance in the entire UV range with intense peaks at 290 and 320 nm. It is due to the presence of mycosporine-like amino acids such as tryptophan, phenylalanine and tyrosine; a complex amino acid with a central aromatic ring. As mycosporine forms resonance tautomers, whose extensive conjugation expedite the absorption of UV radiation (Fernandes et al. 2015). Prawn shells annealed at 500, 600 and 900 °C are showing negligible absorbance in the UV range (Figure 6.6(a)ii, (a)iii and (a)iv; it is because of the decomposition of the proteins. A detail of the proteins present in the shrimp/prawn shell reported in the literature is tabulated in Table 6.4 with a clear demarcation of UV absorbing and non-UV absorbing proteins. Upon compiling both, XPS and UV-visible spectroscopy, it can be inferred that there is a presence of UV absorbing proteins, which are mycosporine-like amino acids with a central aromatic

ring, namely tryptophan, phenylalanine and tyrosine (Figure 6.6(b)). The chemical structures were obtained with reference to the Chemical Abstracts Service (CAS) registry number, CAS No: 54-12-6 (tryptophan), CAS No: 150-30-1 (phenylalanine) and CAS No: 556-03-6 (Tyrosine). Prawn exoskeleton and its derivative can be used as permissible sunscreen filters in cosmetics, textiles, and also in biodegradable packaging of food, drugs etc. The exoskeleton of prawns can also be utilised as constituents in polymer coatings to protect from harmful UV radiation.

6.3 Conclusions

The prawns (*Fenneropenaeus Indicus*) exoskeleton containing mycosporine-like amino acids with a central aromatic ring can offer excellent UV protection (200 – 400 nm). The prawn outershell composite is composed of α-chitin, spherical calcites (0.74 ± 0.154 μm), proteins and traces of $Mg(OH_2)/MgO$. The unique design of α-chitin and protein fibres in the composite resembles a twisted woven-rope with periodic branches. The prawn shell contains 6 % moisture, 42 % calcite and the remaining 52 % organic matter includes α-chitin and proteins. XPS confirms the presence of O-C=O, protonated-N and oxidized pyridinic-N at 288.65, 402.2 and 404.05 eV respectively, which signifies the presence of mycosporine-like amino acids. Absorption in the entire UV range (200 - 400 nm) with two intense peaks at 290 and 320 nm is due to the presence of mycosporine-like amino acids with a central aromatic ring, such as tryptophan, phenylalanine and tyrosine. As mycosporine forms resonance tautomers, whose extensive conjugation expedite the absorption of UV rays. Extraction of UV absorbing protein from prawn shells can have versatile potential applications as sunscreen filters in cosmetics, textiles, food, pharmaceuticals and biodegradable packaging products.

Page left intentionally blank

CHAPTER 7

CONCLUSIONS

In the present thesis, abundantly available marine benthos biowaste namely, *Austromegabalanus psittacus* (AMBP), star fish (*Asteroidea*), sea urchin (*Echinoidea*) cuttlefish bone (*Sepia officinalis*), goose barnacle (*Lepas anserifera*), sea crab (*Neptunus sanguinolentus*), prawn (*Fenneropenaeus indicus*) and sand dollar (*Clypeaster humilis*) based calcite/aragonite was utilized to the synthesis of biogenic HA with wet chemical precipitation method. Porous HA scaffold was developed by the addition of organic pore formers where porous architecture was established by the decompose/burn out of organics during sintering at 1100 °C. Secondly, Fe^{3+} ionic substitution in cuttlefish bone based HA was carried out by ion exchange procedure to enhance UV absorption properties. Finally, the exploration of the prawn exoskeleton as a natural impermeable layer of UV protection and identification of the constituents responsible for UV absorption was executed. Based on experimental findings and analysis, the following conclusions are drawn:

> Along with the crystalline phase of HA from all benthos, HA shows needle shape morphology with a stoichiometric Ca/P ratio ~ 1.66.

> Sintered dense HA from prawn shell, shows the highest compressive strength of 65.5 ± 21.7 MPa with compressive modulus of 4.15 ± 0.2 GPa with the lowest porosity ~ 1.3 %, which can be a suitable candidate for dense HA applications.

> HA from *Austromegabalanus psittacus*, cuttlefish bone, goose barnacle, prawn and sand dollar was used to prepare porous scaffolds by the addition of 10 wt. % wheat flour as organic pore former. HA from cuttlefish bone based exhibits a union of moderate compressive strength of 12-15 MPa with elastic modulus up to 1.6 GPa are accomplished with ~98 % interconnected porosity and 34 % open porosity using wheat flour as the pore former (10 wt.%).

> A tailored porous architecture from cuttlefish bone based HA scaffolds were established with aid of organic pore formers such as milk powder, wheat flour, and wax.

- The faster biomineralization with full coverage of new apatite on porous HA was achieved within 3 days of incubation in SBF, this could be attributed to the existence of the presence of trace elements like Na^+ and Fe^{2+}.

- The biogenic HA with pore former scaffolds are hydrophilic compared to non-biogenic and biogenic HA without pore formers leads to a more suitable surface for cell adhesion.

- An increase in osteoblast (MC3T3-E1) cell viability on HA/wheat flour and HA/milk powder scaffold surface was observed in comparison with biogenic dense HA and non-biogenic HA without pore formers for an incubation period of 7 days. A combination of porous architecture and advantageous trace elements in biogenic HA scaffolds can have potential applications in bone repair and regeneration.

- Undoped HA and Fe-HA both are similar in terms of crystallinity, but crystallite size and lattice parameters decrease with an increase in the concentration of Fe^{3+}.

- The Raman spectra signatures at 1085 cm^{-1} are gradually shifted to 1033 cm^{-1} for Fe-HA, which is accounted for the substitution of Fe^{3+} in place of Ca^{2+}. With the increase of Fe concentration, the crystallite size reduces, but particle size increases, which may be due to the agglomeration of Fe- HA nanosized particles.

- The optical property of Fe-HA was established to be of greater importance as the absorption spectra of Fe-HA powder covered the entire UV range with maximum absorption at 240 nm, which could be a promising biocompatible UV absorbing material in potential sunscreen filter applications.

- The optical band gap of undoped HA (5.95eV) was drastically fallen to 2.14, 2.08, 2.14, 1.84 and 2.18 eV for 0.01, 0.02, 0.03, 0.04 and 0.05 M Fe-HA respectively, which could be attributed to a difference in the energy levels of conduction and valance bands.

- The architecture of exoskeleton composite constitutes a matrix of α-chitin-proteins with distinct reinforcements such as spherical calcites ($CaCO_3$) (0.74 ± 0.154 μm), microscopic proteins, and traces of hydroxides/oxides of

magnesium. The prawn shell contains 6% moisture, 42% calcite and the remaining 52% organic matter includes α-chitin and proteins.

➤ XPS confirms the existence of O-C=O, protonated-N and oxidized pyridinic-N at 288.65, 402.2 and 404.05 eV respectively, which signifies the presence of mycosporine-like amino acids. A prawn exoskeleton with mycosporine-like amino acids with a central aromatic ring can offer excellent UV protection.

➤ Absorption in the entire UV range with two intense peaks at 290 and 320 nm is due to the presence of tryptophan, phenylalanine and tyrosine.

➤ The extraction of UV absorbing proteins present in the prawn exoskeleton can have versatile potential applications as sunscreen filters in cosmetics, textiles, food, pharmaceuticals as well as biodegradable packaging products.

7.1 Scope for future work

The results and analysis of the current study are aimed at the low cost synthesis of biogenic HA from marine benthos biowaste. Biogenic HA based dense bodies and porous scaffolds can be a new class of biomaterials mainly in tissue engineering. To establish the significance of the present study and *in vivo* animal model can be carried out to understand the biocompatibility of the developed material.

Fe-HA based biocompatible UV absorbing material in sunscreen filters has scope for future study on various applications like cosmetics and other UV protecting products. The preparation of cream from Fe-HA powder, testing of creams like photostability and *in vivo* test of the acute irritant potential can be assessed for safe cosmetic applications. Extraction of UV absorbing proteins from abundant prawn exoskeleton can allow a new direction to develop natural UV protection for cosmetics, textiles, food, pharmaceuticals and biodegradable packaging products.

APPENDIX I

Differential scanning calorimetric (DSC) analysis of aragonite/calcite ($CaCO_3$) obtained from marine benthos
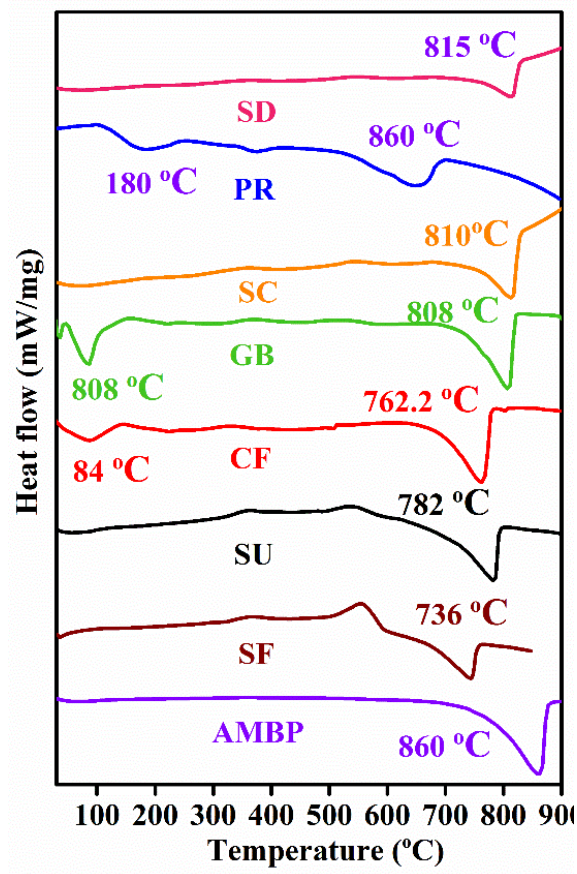
Figure A-I: DSC analysis of aragonite/calcite ($CaCO_3$) from marine benthos namely *Austromegabalanus psittacus* (AMBP), star fish (SF), sea urchin (SU) cuttlefish bone (CF), goose barnacle (*Lepas anserifera*), sea crab (*Neptunus sanguinolentus*), prawn (*Fenneropenaeus indicus*) and sand dollar (*Clypeaster humilis*).

Lattice parameter calculation

$$\frac{1}{d^2} = \frac{\frac{4}{3}(h^2 + hk + k^2)}{a^2} + \frac{l^2}{c^2}$$

where, d is lattice space between two planes, h, k and l are miller indexes, a and c are lattice parameters

112

Table A-I: X-ray diffraction parameters of sintered hydroxyapatite from cuttlefish bone

2θ Experimental	2θ Theoretical	(hkl)	d spacing experimental	d spacing theoretical	Lattice parameter 'a' Å	Lattice parameter 'c' Å	Standard a and c Å
31.9	31.79	211	2.729	2.8146	9.2809	6.226	a = 9.418 and c = 6.887
32.9	33.1	300	2.678	2.72047	9.276		
					9.278	6.226	

APPENDIX II

Structural characterization of sintered HA from cuttlefish bone
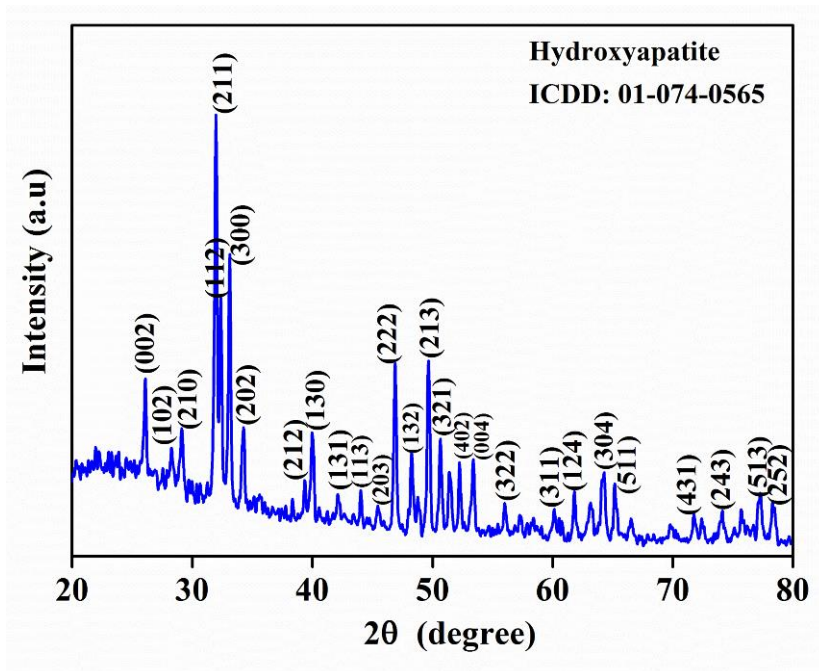
Figure A-II. XRD pattern of cuttlefish-bone-derived HA powder sintered at 1100 °C

APPENDIX III

XPS survey spectrum of as-synthesized hydroxyapatite from cuttlefish bone
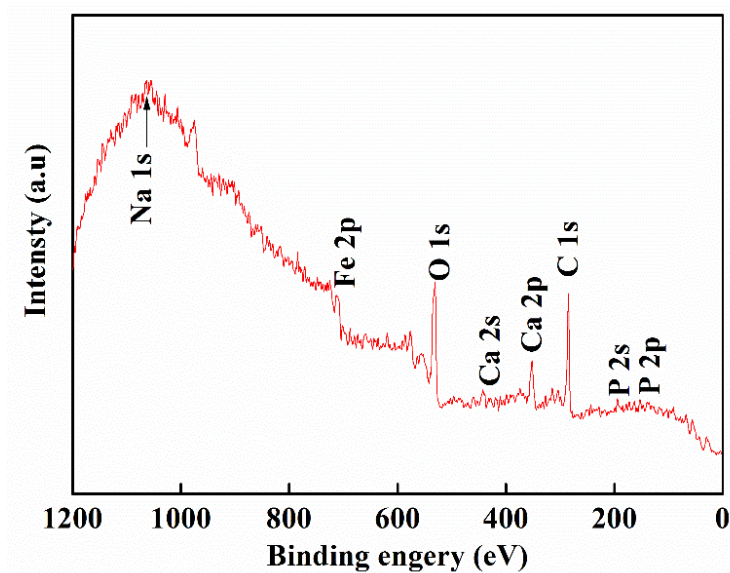
Figure A-III: XPS survey spectrum of as-synthesized hydroxyapatite from cuttlefish bone

APPENDIX IV

Thermo-gravimetric analysis of as-synthesised hydroxyaptite powder from cuttlefish bone
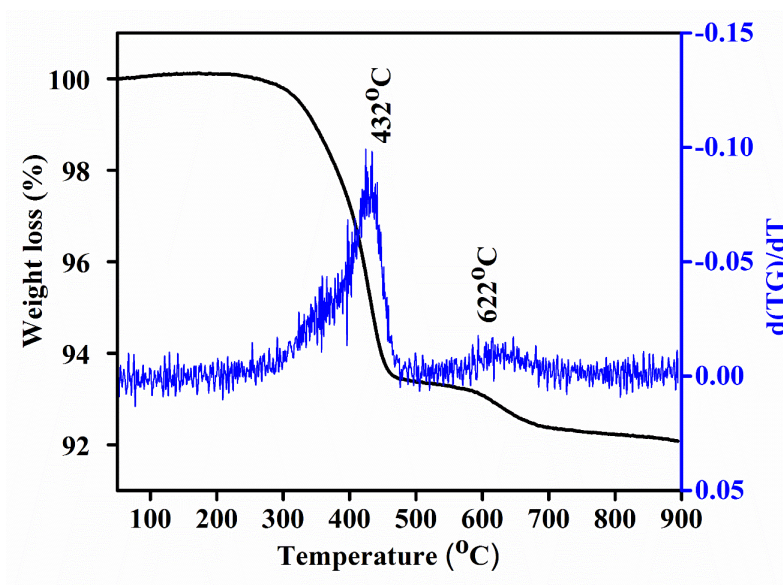
Figure A-IV: TGA and differential TG graph of as-synthesised hydroxyaptite powder from cuttlefish bone

APPENDIX V

X-ray diffraction analysis of new apatite formed on HA scaffold surface in SBF
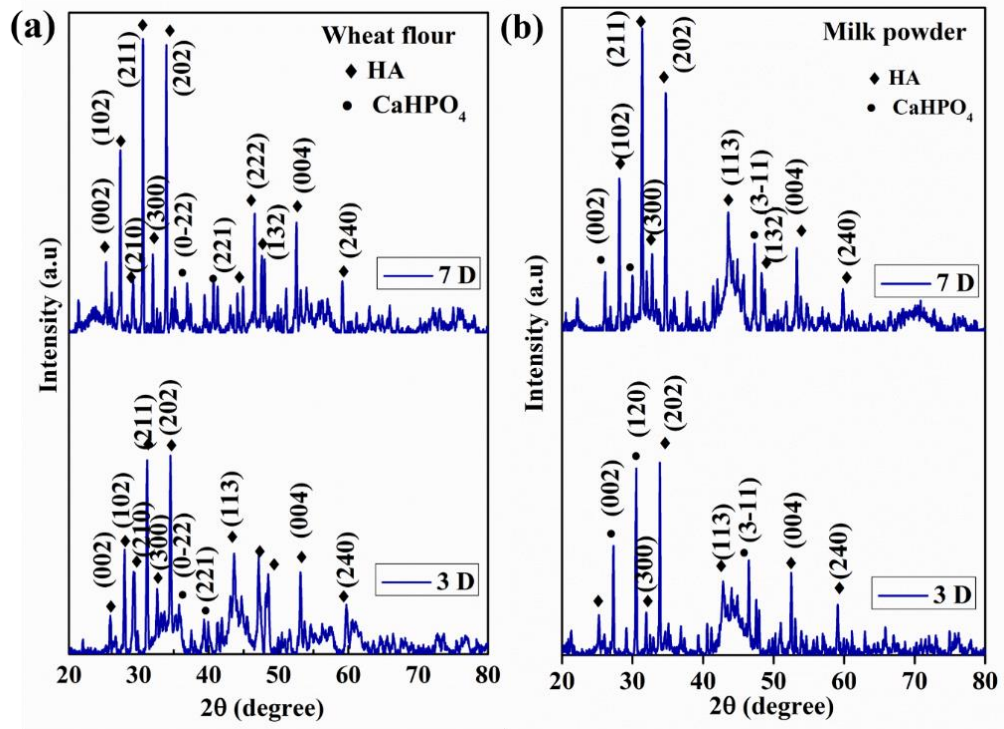
Figure A-V: X-ray diffraction pattern of new apatite on HA scaffold surface when immersed in simulated body fluid for 3 and 7 days: a) HA scaffold with wheat flour as pore former and b) HA scaffold with milk powder as pore former.

APPENDIX VI

Table A-VI: Spreadsheet for the calculation of precise lattice parameters 'a' and 'c' of 0.01 M Fe-HA using Cohen's analysis method.

2θ	θ	h	k	l	α	γ	δ	α²	αγ	αδ	γ²	γδ	δ²	α(sin²θ)	γ(Sin²θ)	δ(Sin²θ)
28.82	14.41	2	1	0	7	0	0.2323	49	0	1.6261	0	0	0.053963	0.4333	0	0.014379
31.89	15.945	2	1	1	7	1	0.279	49	7	1.953	1	0.279	0.077841	0.52822	0.07546	0.021053
33.04	16.52	3	0	0	9	0	0.2972	81	0	2.6748	0	0	0.088328	0.72	0	0.023776
34.15	17.075	2	0	2	4	4	0.3151	16	16	1.2604	16	1.2604	0.099288	0.3448	0.3448	0.027162
39.22	19.61	2	1	2	7	4	0.399	49	28	2.793	16	1.596	0.159201	0.7882	0.4504	0.044927
40.24	20.12	1	3	0	13	0	0.4173	169	0	5.4249	0	0	0.174139	1.5379	0	0.049367
46.76	23.38	2	2	2	12	4	0.5306	144	48	6.3672	16	2.1224	0.281536	1.8888	0.6296	0.083516
49.49	24.745	2	1	3	7	9	0.578	49	63	4.046	81	5.202	0.334084	1.2264	1.5768	0.101266
50.9	25.45	3	2	1	19	1	0.6022	361	19	11.4418	1	0.6022	0.362645	3.5074	0.1846	0.111166
53.32	26.66	0	0	4	0	16	0.6431	0	0	0	256	10.2896	0.413578	0	2.95456	0.118755

$\alpha = (h^2 - k^2 - hk)$ $\Sigma\alpha^2 = 967$ $\Sigma\alpha\gamma = 181$ $\Sigma\alpha\delta = 37.587$ $\Sigma\gamma^2 = 387$ $\Sigma\gamma\delta = 21.3516$ $\Sigma\delta^2 = 2.0446$ $\Sigma\alpha\sin\theta = 10.975$ $\Sigma\gamma\sin\theta = 6.2162$ $\Sigma\delta\sin\theta = 0.5953$

$\gamma = l^2$, $\delta = Sin^2 2\theta$

$$967A + 181B + 37.587C = 10.975$$
$$181A + 387B + 21.3516C = 6.2162$$
$$81A + 387B + 21.3516C = 6.2162$$

$$a = \frac{\lambda}{(3A)^{1/2}} = 9.343 \text{ Å} \qquad\qquad c = \frac{\lambda}{(4B)^{1/2}} = 7.13 \text{ Å}$$

APPENDIX VII

The XPS spectra were calibrated by carbon 1s (C 1s) peak centered at 284.7 eV. The C 1s peak fitting analysis is performed in order to determine the position of the C-H/C-C peak so as to account for charge correction. Four synthetic peaks namely C-H/C-C (peak I), C-O (peak II), C=O (peak III), O-C=O (peak IV) were fit into the experimental data of C 1s by fixing Full Width Half Maximum (FWHM = 1.17), Gaussian-Lorentzian (GL) product peak positions relative to the main C-H/C-C peak. Table A-VII provides the peak position constraints and parameters of deconvoluted peaks for 0.01 M and 0.05 M Fe-HA.

Table A-VII. Peak fit parameters of C 1s for 0.01 M and 0.05 M Fe-HA

Signatures of deconvoluted peaks	Position constraints	GL ratio	Position (eV)	Area	FWHM constraints	FWHM	Area (%)
C-H/C-C (peak I)	--	30	284.7	622.49	--	1.17	34.77
C-O (peak II)	Peak I + 1.5 eV	30	286.2	303.77	(Peak I) × 1	1.17	16.97
C=O (peak III)	Peak I + 3.0 eV	30	287.7	304.95	(Peak I) × 1	1.17	17.03
O=C-O (peak IV)	Peak I + 4.0 eV	30	289.2	405.99	(Peak I) × 1	1.17	22.68

APPENDIX VIII

The peak fitting procedure is the same as that of A-VII. Table A-VIII gives the peak fitting parameters of C 1s for prawn exoskeleton

Table A-VIII: Peak fit parameters of C 1s for prawn exoskeleton

Signatures of deconvoluted peaks	Position constraints	GL ratio	Positions (eV)	Area	FWHM constraints	FW HM	Area (%)
C-H/C-C (peak I)	--	30	284.68	4159.1	--	1.57	28.81
C-O (peak II)	Peak I + 1.5 eV	30	291.19	1799.4	(Peak I) × 1	1.57	12.47
C=O (peak III)	Peak I + 3.0 eV	30	286.2	2262.1	(Peak I) × 1	1.57	15.67
O=C-O (peak IV)	Peak I + 4.0 eV	30	289.96	1885.6	(Peak I) × 1	1.57	13.06
CO_3^{2-} (peak V)	Peak I + 4.0 eV	30	288.65	502.61	(Peak I) × 1	1.57	10.41
CO_3^{2-} (peak VI)	Peak I + 4.0 eV	30	287.55	1481.3	(Peak I) × 1	1.57	10.26

Page left intentionally blank

REFERENCES

Abazović, N. D., Mirenghi, L., Janković, I. A., Bibić, N., Šojić, D. V., Abramović, B. F. and Čomor, M. I. (2009). "Synthesis and characterization of rutile TiO₂ nanopowders doped with iron ions". *Nanoscale Res. Lett.,* 4(6), 518-525.

Ağaoğullari, D., Kel, D., Gökçe, H., Duman, I., Öveçoglu, M., Akarsubaşi, Akarsubaşic, T., Bilgiç, D. and Oktar, F.N. (2012). "Bioceramic Production from Sea Urchins". *Acta Phys. Pol. A,* 121(1), 23-26.

Akram, M., Ahmed, R., Shakir, I., Ibrahim, W. A. W. and Hussain, R. (2014). "Extracting hydroxyapatite and its precursors from natural resources". *J. Mater. Sci.,* 49(4), 1461-1475.

Albayrak, O., Ipekoglu, M., Mahmutyazicioglu, N., Varmis, M., Kaya, E. and Altintas, S. (2016). "Preparation and characterization of porous hydroxyapatite pellets: Effects of calcination and sintering on the porous structure and mechanical properties". *P. I. Mech. Eng. L- J. Mat.,* 230(6), 985-993.

Alshemary, A. Z., Akram, M., Goh, Y.-F., Kadir, M. R. A., Abdolahi, A. and Hussain, R. (2015). "Structural characterization, optical properties and in vitro bioactivity of mesoporous erbium-doped hydroxyapatite". *J. Alloy. Compd.,* 645, 478-486.

Anjaneyulu, U., Pattanayak, D. K. and Vijayalakshmi, U. (2016). "Snail shell derived natural hydroxyapatite: effects on NIH-3T3 cells for orthopedic applications". *Mater. Manuf. Process.,* 31(2), 206-216.

Antoniac, V. I., Lesci, I. G., Blajan, A. I., Vitioanu, G. and Antoniac, A. (2015). "Bioceramics and biocomposites from marine sources". *Key Eng. Mater.,* 672, 276-292.

Antoniou, C., Kosmadaki, M. G., Stratigos, A. J. and Katsambas, A. D. (2008). "Sunscreens–what's important to know". *J. Eur. Acad. Dermatol. Venereol.,* 22(9), 1110-1119.

Anwar, A., Kanwal, Q., Akbar, S., Munawar, A., Durrani, A. and Farooq, M. H. (2017). "Synthesis and characterization of pure and nanosized hydroxyapatite bioceramics". *Nanotechnol. Rev.,* 6(2), 149-157.

Basu, B. (2017). "Biomaterials science and tissue engineering: principles and methods". *Cambridge University Press.*

Basu, B., Swain, S. K. and Sarkar, D. (2013). "Cryogenically cured hydroxyapatite–gelatin nanobiocomposite for bovine serum albumin protein adsorption and release". *RSC Adv.,* 3(34), 14622-14633.

Bhaskar, N., Sarkar, D. and Basu, B. (2018). "Probing cytocompatibility, hemocompatibility, and quantitative inflammatory response in mus musculus toward oxide bioceramic wear particulates and a comparison with CoCr". *ACS Biomater. Sci. Eng.,* 4(9), 3194-3210.

Bogdanoviciene, I., Beganskiene, A., Tonsuaadu, K., Glaser, J., Meyer, H.-J. and Kareiva, A. (2006). "Calcium hydroxyapatite, $Ca_{10}(PO_4)_6(OH)_2$ ceramics prepared by aqueous sol–gel processing". *Mater. Res. Bull.,* 41(9), 1754-1762.

Burns, R. G. (1993). "Mineralogical applications of crystal field theory (Vol. 5)": *Cambridge University Press.*

Bystrov, V., Piccirillo, C., Tobaldi, D., Castro, P., Coutinho, J., Kopyl, S. and Pullar, R. (2016). "Oxygen vacancies, the optical band gap (Eg) and photocatalysis of hydroxyapatite: comparing modelling with measured data". *Appl. Catal. B.,* 196, 100-107.

Cadman, J., Zhou, S., Chen, Y. and Li, Q. (2012). "Cuttlebone: characterisation, application and development of biomimetic materials". *J. Bionic Eng., 9*(3), 367-376.

Chang, C. (1988). "Measuring density and porosity of grain kernels using a gas pycnometer". *Cereal. Chem.,* 65(1), 13-15.

Chavan, P. N., Bahir, M. M., Mene, R. U., Mahabole, M. P. and Khairnar, R. S. (2010). "Study of nanobiomaterial hydroxyapatite in simulated body fluid: formation and growth of apatite". *Mater. Sci. Eng. B,* 168(1-3), 224-230.

Chen, J., Wen, Z., Zhong, S., Wang, Z., Wu, J. and Zhang, Q. (2015). "Synthesis of hydroxyapatite nanorods from abalone shells via hydrothermal solid-state conversion". *Mater. Des.,* 87, 445-449.

Christie, A., Lee, J., Sutherland, I. and Walls, J. (1983). "An XPS study of ion-induced compositional changes with group II and group IV compounds". *Appl. Surf. Sci.,* 15(1-4), 224-237.

Cullity, B. D. (1956). "Elements of X-ray diffraction", *Addison-Wesley Publishing*.

De Araujo, T., De Souza, S. and De Sousa, E. (2010). "Effect of Zn^{2+}, Fe^{3+} and Cr^{3+} addition to hydroxyapatite for its application as an active constituent of sunscreens". *J. Phys. Conf. Ser.,* 249, 012012 (1-7).

De Araujo, T., De Souza, S., Miyakawa, W. and De Sousa, E. (2010). "Phosphates nanoparticles doped with zinc and manganese for sunscreens". *Mater. Chem. Phys.,* 124(2-3), 1071-1076.

Deravi, L. F., Magyar, A. P., Sheehy, S. P., Bell, G. R., Mäthger, L. M., Senft, S. L., Trevor, J. W., William, S. L., Alan, M. K,, Roger, T., Hanlon, Evelyn, L. H. and Kevin, K. P. (2014). "The structure–function relationships of a natural nanoscale photonic device in cuttlefish chromatophores". *J. R. Soc. Interface,* 11(93), 20130942 (1-9).

Eddya, M., Tbib, B. and El-Hami, K. (2018). "High photocatalytic activity of hydroxyapatite bio-degradable semiconductor for solar panels and environment protection". *ISTE OPEN SCIENCE*, 1-8.

Eilbagi, M., Emadi, R., Raeissi, K., Kharaziha, M. and Valiani, A. (2016). "Mechanical and cytotoxicity evaluation of nanostructured hydroxyapatite-bredigite scaffolds for bone regeneration". *Mater. Sci. Eng. C,* 68, 603-612.

Eslami, H., Soulati, H. M. and Tahriri, M. (2008). "Synthesis and characterization of hydroxyapatite nanocrystals via chemical precipitation technique". *Iran. J. Pharm. Sci.* 4(2), 127-134.

Fadli, A., Akbar, F., Putri, P., Pratiwi, D. I. and Muhara, I. (2014). "Hydroxyapatite powder prepared by low temperature hydrothermal method from sea shells". *Sci. Eng., 1-6.*

Faksawat, K., Sujinnapram, S., Limsuwan, P., Hoonnivathana, E. and Naemchanthara, K. (2015). "Preparation and characteristic of hydroxyapatite synthesized from cuttlefish bone by precipitation method". *Adv. Mater. Res.,* 1125*,* 421-425.

Feng, M., Lu, X., Jiang, K., Zhang, J., Xin, J., Shi, C., Kefeng, W. and Suojiang, Z. (2018). "One-step preparation of an antibacterial chitin/Zn composite from shrimp shells using urea-Zn $(OAc)_2 \cdot 2H_2O$ aqueous solution". *Green Chem.,* 20(10), 2212-2217.

Fernandes, S. C., Alonso-Varona, A., Palomares, T., Zubillaga, V. N., Labidi, J. and Bulone, V. (2015). "Exploiting mycosporines as natural molecular sunscreens for the fabrication of UV-absorbing green materials". *ACS Appl. Mater. Interfaces,* 7(30), 16558-16564.

Ghimire, S., Neupane, B., Pokhrel, S., Le, H. H., Lebek, W., Heinrich, G., Yadav, P. N and Adhikari, R. (2017). "Conversion of chitin isolated from fresh-water prawns to chitosan and its characterization". *Polym. Res. J.,* 11(1), 1-15.

Gunduz, O., Sahin, Y., Agathopoulos, S., Ben-Nissan, B. and Oktar, F. N. (2014). "A new method for fabrication of nanohydroxyapatite and TCP from the sea snail Cerithium vulgatum". *J. Nanomater.,* 382861 (1-6).

Hamed, I., Özogul, F. and Regenstein, J. (2016). "Industrial applications of crustacean by-products (chitin, chitosan, and chitooligosaccharides): a review". *Trends Food Sci. Technol.* 48, 40-50.

Han, C., Duan, L., Zhao, X., Hu, Z., Niu, Y. and Geng, W. (2019). "Effect of Fe doping on structural and optical properties of ZnO films and nanorods". *J. Alloy. Compd.,* 770, 854-863.

Hannink, G. and Arts, J. C. (2011). "Bioresorbability, porosity and mechanical strength of bone substitutes: what is optimal for bone regeneration?". *Injury,* 42, S22-S25.

Hansen, M. and Illanes, A. (1994). "Applications of crustacean wastes in biotechnology" *Fisheries Processing,* 174-205.

Hazra, C., Samanta, T. and Mahalingam, V. (2014). "A resonance energy transfer approach for the selective detection of aromatic amino acids". *J. Mater. Chem. C,* 2(47), 10157-10163.

Helen, S. and Kumar, A. R. (2019). "Study of structural, mechanical and dielectrical properties of ions doped apatite for antibacterial activity". *Mater. Chem. Phys.,* 237, 121867 (1-12).

Ibrahim, H., Salama, M. and El-Banna, H. (1999). "Shrimp's waste: Chemical composition, nutritional value and utilization". *Food/Nahrung,* 43(6), 418-423.

Ieva, E., Trapani, A., Cioffi, N., Ditaranto, N., Monopoli, A. and Sabbatini, L. (2009). "Analytical characterization of chitosan nanoparticles for peptide drug delivery applications". *Anal. Bioanal. Chem.,* 393(1), 207-215.

Jain, S. and Jain, N. (2010). "Multiparticulate carriers for sun-screening agents". *Int. J. Cosm. Sci.* 32(2), 89-98.

Jang, D.-W., Franco, R. A., Sarkar, S. K. and Lee, B.-T. (2014). "Fabrication of porous hydroxyapatite scaffolds as artificial bone preform and its biocompatibility evaluation". *Asaio J.* 60(2), 216.

Jang, M. K., Kong, B. G., Jeong, Y. I., Lee, C. H. and Nah, J. W. (2004). "Physicochemical characterization of α-chitin, β-chitin, and γ-chitin separated from natural resources". *J. Polym. Sci. A: Polym. Chem.,* 42(14), 3423-3432.

Järvinen, L., Leiro, J. and Heinonen, M. (2014). "Core level studies of calcite and dolomite". *Surf. Interface Anal.,* 46(6), 399-406.

Jiménez-Flores, Y., Suárez-Quezada, M., Rojas-Trigos, J., Lartundo-Rojas, L., Suárez, V. and Mantilla, A. (2017). "Characterization of Tb-doped hydroxyapatite for biomedical applications: optical properties and energy band gap determination". *J. Mater. Sci.,* 52(17), 9990-10000.

Kasemo, B. (2002). "Biological surface science". *Surf. Sci.,* 500(1-3), 656-677.

Kaygili, O., Dorozhkin, S. V., Ates, T., Al-Ghamdi, A. A. and Yakuphanoglu, F. (2014). "Dielectric properties of Fe doped hydroxyapatite prepared by sol–gel method". *Ceram. Inter.,* 40(7), 9395-9402.

Kel, D., Gökçe, H., Bilgiç, D., Ağaoğulları, D., Duman, I., Öveçoğlu, M.L., Eyup, S. K., Ismail, A. K., Simeon, A. and Oktar, F.N. (2012). "Production of natural bioceramic from land snails". *Key Eng. Mater.,* 493, 287-292.

Khandan, A., Karamian, E. and Bonakdarchian, M. (2014). "Mechanochemical synthesis evaluation of nanocrystalline bone-derived bioceramic powder using for bone tissue engineering". *Dent. Hypotheses,* 5(4), 155.

Kim, B.-S., Kang, H. J., Yang, S.-S. and Lee, J. (2014). "Comparison of *in vitro* and *in vivo* bioactivity: cuttlefish-bone-derived hydroxyapatite and synthetic hydroxyapatite granules as a bone graft substitute". *Biomed. Mater.,* 9(2), 025004 (1-9).

Kim, H., Mondal, S., Bharathiraja, S., Manivasagan, P., Moorthy, M. S. and Oh, J. (2018). "Optimized Zn-doped hydroxyapatite/doxorubicin bioceramics system for efficient drug delivery and tissue engineering application". *Ceram. Inter.,* 44(6), 6062-6071.

Kim, Y., Suhr, J., Seo, H. W., Sun, H., Kim, S., Park, I. K., Kim, S. H., Lee, Y., Kim, K. J. and Nam, J. D. (2017). "All biomass and UV protective composite composed of compatibilized lignin and poly (lactic-acid)". *Sci. Rep.,* 7, 43596 (1-11).

Knorr, D. (1984). "Use of chitinous polymers in food: a challenge for food research and development". *Food Technol. (USA).*

Kokubo, T. and Takadama, H. (2006). "How useful is SBF in predicting in vivo bone bioactivity?". *Biomaterials,* 27(15), 2907-2915.

Kramer, E. R., Morey, A. M., Staruch, M., Suib, S. L., Jain, M., Budnick, J. I. and Wei, M. (2013). "Synthesis and characterization of iron-substituted hydroxyapatite via a simple ion-exchange procedure". *J. Mater. Sci.,* 48(2), 665-673.

Kresse, G. and Furthmüller, J. (1996). "Efficiency of ab-initio total energy calculations for metals and semiconductors using a plane-wave basis set". *Comput. Mater. Sci.,* 6(1), 15-50.

Liu, D.-M. (1997). "Influence of porosity and pore size on the compressive strength of porous hydroxyapatite ceramic". *Ceram. Inter.,* 23(2), 135-139.

Luo, J.and Stevens, R. (1999). "Porosity-dependence of elastic moduli and hardness of 3Y-TZP ceramics". *Ceram. Inter.,* 25(3), 281-286.

Mahmood, B. K., Kaygili, O., Bulut, N., Dorozhkin, S. V., Ates, T., Koytepe, S., Gürsese, C., Ercan, F., Kebiroglu, H., Agid, R. S. and İnce, T. (2020). "Effects of strontium-erbium co-doping on the structural properties of hydroxyapatite: an experimental and theoretical study". *Ceram. Inter.,* 46(10), 16354-16363.

Mariappan, A., Pandi, P., Balasubramanian, N., Palanichamy, R. R. and Neyvasagam, K. (2017). "Structural, optical and antimicrobial activity of copper and zinc doped hydroxyapatite nanopowders using sol-gel method". *Mech. Mater. Sci. Eng.,* 9 (1), 01497923 (1-6).

Mehta, D., Mondal, P., Saharan, V. K. and George, S. (2017). "Synthesis of hydroxyapatite nanorods for application in water defluoridation and optimization of process variables: advantage of ultrasonication with precipitation method over conventional method". *Ultrason. Sonochem.* 37, 56-70.

Mehta, P. K. and Monteiro, P. J. (2017). "Concrete microstructure, properties and materials". *University of California, Berkeley.*

Moradi, K. and Alvani, A. S. (2019). "First-principles study on Sr-doped hydroxyapatite as a biocompatible filler for photo-cured dental composites". *J. Aust Ceram. Soc.*, 56, 591–598.

Nandi, S. K., Kundu, B., Mukherjee, J., Mahato, A., Datta, S. and Balla, V. K. (2015). "Converted marine coral hydroxyapatite implants with growth factors: *in vivo* bone regeneration". *Mater. Sci. Eng. C,* 49, 816-823.

Ocampo, J. I. G., Sierra, D. M. E. and Orozco, C. P. O. (2016). "Porous bodies of hydroxyapatite produced by a combination of the gel-casting and polymer sponge methods". *J. Adv. Res.,* 7(2), 297-304.

Oliveira, J. M., Silva, S. S., Malafaya, P. B., Rodrigues, M. T., Kotobuki, N., Hirose, M. and Reis, R. L. (2009). "Macroporous hydroxyapatite scaffolds for bone tissue engineering applications: Physicochemical characterization and assessment of rat bone marrow stromal cell viability". *J. Biomed. Mater. Res. A,* 91(1), 175-186.

Ospina Álvarez, S. P., Ramírez Cadavid, D. A., Escobar Sierra, D. M., Ossa Orozco, C. P., Rojas Vahos, D. F., Zapata Ocampo, P. and Atehortúa, L. (2014). "Comparison of extraction methods of chitin from ganoderma lucidum mushroom obtained in submerged culture". *BioMed. Res. Inter.,* 169071 (1-7).

Oyamada, C., Kaneniwa, M., Ebitani, K., Murata, M. and Ishihara, K. (2008). "Mycosporine-like amino acids extracted from scallop (*Patinopecten yessoensis*) ovaries: UV protection and growth stimulation activities on human cells". *Mar. Biotech.,* 10(2), 141-150.

Ozyegin, L., Sima, F., Ristoscu, C., Kiyici, I. A., Mihailescu, I. N., Meydanoglu, O., Agathopoulos, S. and Oktar, F. (2012). "*Sea snail: an alternative source for nano-bioceramic production". Key Eng. Mater.,* 493-494, 781-786.

Pal, A., Hadagalli, K., Bhat, P., Goel, V. and Mandal, S. (2020). " Hydroxyapatite - a promising sunscreen filter" . *J. Aust. Ceram. Soc.,* 56(1), 345-351.

Perdew, J. P., Burke, K. and Ernzerhof, M. (1996). "Generalized gradient approximation made simple". *Phys. Rev. Lett.* 77(18), 3865-3868.

Perdew, J. P. and Wang, Y. (1992). "Accurate and simple analytic representation of the electron-gas correlation energy". *Phys. Rev. B,* 45(23), 13244.

Phani, K. K. and Niyogi, S. (1987). "Elastic modulus-porosity relation in polycrystalline rare-earth oxides". *J. Am. Ceram. Soc.,* 70(12), 362-366.

Piccirillo, C., Pullar, R., Costa, E., Santos-Silva, A., Pintado, M. and Castro, P. M. (2015). "Hydroxyapatite-based materials of marine origin: a bioactivity and sintering study. *Mater. Sci. Eng. C,* 51, 309-315.

Piccirillo, C., Rocha, C., Tobaldi, D., Pullar, R., Labrincha, J., Ferreira, M., Castroa, P. M. L. and Pintado, M. (2014). "A hydroxyapatite - Fe_2O_3 based material of natural origin as an active sunscreen filter". *J. Mater. Chem. B,* 2(36), 5999-6009.

Poinern, G. E. J., Brundavanam, R. K., Le, X. T., Nicholls, P. K., Cake, M. A. and Fawcett, D. (2014). "The synthesis, characterisation and *in vivo* study of a bioceramic for potential tissue regeneration applications". *Sci. Rep.,* 4, 6235 (1-9).

Prakasam, M., Locs, J., Salma-Ancane, K., Loca, D., Largeteau, A. and Berzina-Cimdina, L. (2015). "Fabrication, properties and applications of dense hydroxyapatite: a review". *J. Funct. Biomater.,* 6(4), 1099-1140.

Qian, Y., Qiu, X., and Zhu, S. (2015). "Lignin: a nature-inspired sun blocker for broad-spectrum sunscreens". *Green Chem.,* 17(1), 320-324.

Raabe, D., Sachs, C. and Romano, P. (2005). "The crustacean exoskeleton as an example of a structurally and mechanically graded biological nanocomposite material". *Acta Mater.,* 53(15), 4281-4292.

Sabree, I., Gough, J. and Derby, B. (2015). "Mechanical properties of porous ceramic scaffolds: influence of internal dimensions". *Ceram. Inter.,* 41(7), 8425-8432.

Sagadevan, S. and Dakshnamoorthy, A. (2013). "Synthesis and characterization of nano-hydroxyapatite (n-HAP) using the wet chemical technique". *Int. J. Phys. Sci.,* 8(32), 1639-1645.

Sahin, Y. M., Orman, Z. and Yucel, S. (2019). "*In vitro* studies of α-TCP and β-TCP produced from clinocardium ciliatum seashells". *J. Aust. Ceram. Soc.,* 56, 477–488.

Santhosh, S. and Balasivanandha Prabu, S. (2012). "Characterization of hydroxyapatite synthesized from sea shells and electrospin coating of hydroxyapatite for biomedical applications". *Adv. Mater. Res.,* 584, 435-439.

Sayre, R. M., Dowdy, J. C., Gerwig, A. J., Shlelds, W. J. and Lioyd, R. V. (2005). "Unexpected photolysis of the sunscreen octinoxate in the presence of the sunscreen avobenzone". *Photochem. Photobio.,* 81(2), 452-456.

Scholz, D. J. (1961). "Radiation pasteurized shrimp and crabmeat". *Oregon State University.*

Shih, W.-J., Chen, Y.-F., Wang, M.-C. and Hon, M.-H. (2004). "Crystal growth and morphology of the nano-sized hydroxyapatite powders synthesized from $CaHPO_4 \cdot 2H_2O$ and $CaCO_3$ by hydrolysis method". *J. Cryst. Growth,* 270(1-2), 211-218.

Shinoda, M., Nishide, T. and Shichi, Y. (1994). "Adhesion between polycarbonate substrate and SiO_2 film formed from silane and nitrous oxide by plasma-enhanced chemical vapor deposition". *J. Vac. Sci. Technol. A,* 12(3), 746-750.

Sivakumar, M., Kumar, T. S., Shantha, K. and Rao, K. P. (1996). "Development of hydroxyapatite derived from Indian coral". *Biomaterials,* 17(17), 1709-1714.

Smijs, T. G. and Pavel, S. (2011). "Titanium dioxide and zinc oxide nanoparticles in sunscreens: focus on their safety and effectiveness". *Nanotechnol. Sci. Aappl.,* 4, 95-112.

Sosulnikov, M. and Teterin, Y. A. (1991). "X-ray photoelectron study of calcium, strontium, barium and their oxides". *Dokl. Akad. Nauk SSSR,* 317(2), 418-421.

Subramaniyan, G., Sundaramoorthy, S. and Andiappan, M. (2013). "Ultraviolet protection property of mulberry fruit extract on cotton fabrics". *NISCAIR-CSIR*, INDIA, 420-423.

Tadic, D. and Epple, M. (2003). "Mechanically stable implants of synthetic bone mineral by cold isostatic pressing". *Biomaterials,* 24(25), 4565-4571.

Teixeira, M., Piccirillo, C., Tobaldi, D., Pullar, R., Labrincha, J., Ferreira, M., Castro, P. M. L. and Pintado, M. (2017). "Effect of preparation and processing conditions on UV absorbing properties of hydroxyapatite-Fe_2O_3 sunscreen". *Mater. Sci. Eng. C,* 71, 141-149.

Teixeira, S., Rodriguez, M., Pena, P., De Aza, A., De Aza, S., Ferraz, M. and Monteiro, F. (2009). "Physical characterization of hydroxyapatite porous scaffolds for tissue engineering". *Mater. Sci. Eng. C,* 29(5), 1510-1514.

Tok, A., Luo, L. and Boey, F (2004). "Carbonate Co-precipitation of Gd_2O_3-doped CeO_2 solid solution nano-particles". *Mater. Sci. Eng. A,* 383(2) 229-234.

Tripathi, G. and Basu, B. (2012). "A porous hydroxyapatite scaffold for bone tissue engineering: physico-mechanical and biological evaluations". *Ceram. Inter.,* 38(1), 341-349.

Tsukada, M., Wakamura, M., Yoshida, N. and Watanabe, T. (2011). "Band gap and photocatalytic properties of Ti-substituted hydroxyapatite: comparison with anatase-TiO_2". *J. Mol. Catal. A: Chem.,* 338(1-2), 18-23.

Varma, H. and Babu, S. S. (2005). "Synthesis of calcium phosphate bioceramics by citrate gel pyrolysis method". *Ceram. Inter.,* 31(1), 109-114.

Vecchio, K. S., Zhang, X., Massie, J. B., Wang, M. and Kim, C. W. (2007). "Conversion of bulk seashells to biocompatible hydroxyapatite for bone implants". *Acta Biomater.,* 3(6), 910-918.

Veljović, D., Jančić-Hajneman, R., Balać, I., Jokić, B., Putić, S., Petrović, R. and Janaćković, D. (2011). "The effect of the shape and size of the pores on the mechanical properties of porous HAP-based bioceramics". *Ceram. Inter.,* 37(2), 471-479.

Venkatesan, J., Qian, Z. J., Ryu, B., Thomas, N. V. and Kim, S. K. (2011). "A comparative study of thermal calcination and an alkaline hydrolysis method in the isolation of hydroxyapatite from thunnus obesus bone". *Biomed. Mater.,* 6(3), 035003 (1-12).

Venkateswarlu, K., Bose, A. C. and Rameshbabu, N. (2010). "X-ray peak broadening studies of nanocrystalline hydroxyapatite by Williamson–Hall analysis". *Physica B: Condens. Matter,* 405(20), 4256-4261.

Wu, W., Liu, T., Deng, X., Sun, Q., Cao, X., Feng, Y. Wang, B., Vellaisamy, A. L. and Li, R. K. (2019). "Ecofriendly UV-protective films based on poly (propylene carbonate)

biocomposites filled with TiO$_2$ decorated lignin". *Int. J. Biol. Macromol.,* 126, 1030-1036.

Yuan, H., Deng, L., Cai, X., Zhou, S., Chen, Y. and Yuan, Y. (2015). "Nitrogen-doped carbon sheets derived from chitin as non-metal bifunctional electrocatalysts for oxygen reduction and evolution". *RSC Adv.,* 5(69), 56121-56129.

Zhong, Q., Li, W., Su, X., Li, G., Zhou, Y., Kundu, S. C., Juming, Y. and Cai, Y. (2016). "Degradation pattern of porous CaCO$_3$ and hydroxyapatite microspheres *in vitro* and *in vivo* for potential application in bone tissue engineering". *Colloids Surf. B,* 143, 56-63.

Zhou, Y., Ge, L., Fan, N. and Xia, M. (2018). "Adsorption of Congo red from aqueous solution onto shrimp shell powder". *Adsorp. Sci. Technol.,* 36(5-6), 1310-1330.

Zilm, M., Chen, L., Sharma, V., McDannald, A., Jain, M., Ramprasad, R. and Wei, M. (2016). "Hydroxyapatite substituted by transition metals: experiment and theory". *Phys. Chem. Chem. Phys.,* 18(24), 16457-16465.

LIST OF PUBLICATIONS

PATENTS FILED:

Pavan Pujar, **Komalakrushna Hadagalli**, Shakya Kaushal Rajendraprasad, Dipti Gupta, Saumen Mandal, "Method and system for fabricating a porous ceramic structure using combustible pore former", Indian Patent, Application No.: 201841033533 dated 6th September, 2018 (**Filed**).

Saumen Mandal, Bikesh Gupta, Pavan Pujar, **Komalakrushna Hadagalli**, Robbi Vivek Vardhan, "Fabrication of High Conductive Metallic Films at Low Temperature", Indian Patent, Patent No.: 347677, Application No.: 201741005384 dated 15th February, 2017 (**Granted**).

JOURNAL PUBLICATIONS

Komalakrushna Hadagalli, Sulakshana Shenoy, Kaushal R Shakya, Manjunath G, Kartick Tarafder, Saumen Mandal, Bikramjit Basu "Effect of Fe^{3+} substitution on the structural modification and band structure modulated UV absorption of hydroxyapatite" **International Journal of Applied Ceramic Technology,** 2020; 00: 1-13.

Komalakrushna Hadagalli, Rahul Kumar, Saumen Mandal, Bikramjit Basu, "Structural, compositional and spectral investigation of prawn exoskeleton nanocomposite: UV protection from mycosporine-like amino acids", **Materials Chemistry and Physics,** 249, 2020, 123002 (1-7).

Komalakrushna Hadagalli, Asish Kumar Panda, Saumen Mandal, Bikramjit Basu. "Faster Biomineralization and Tailored Mechanical Properties of Marine-Resource-Derived Hydroxyapatite Scaffolds with Tunable Interconnected Porous Architecture", **ACS, Applied. Bio Materials**, 2, 2019, 2171−2184.

Komalakrishna Hadagalli, Gaurav Kumar, Biswanath Kundu, Saumen Mandal, "Development of porous nano-hydroxyapatite from *Austromegabalanus psittacus* marine species using camphor and wheat flour as pore formers", **Advanced Science Letters,** 24, 2018, 847–852.

Komalakrishna Hadagalli, Shine Jyoth T.G, Biswanath Kundu, Saumen Mandal, "Low Temperature Development of Nano-Hydroxyapatite from *Austromegabalanus psittacus*, Star fish and Sea urchin", **Materials Today: Proceedings,** 4, 2017, 11933–11938.

Abhishesh Pal, **Komalakrushna Hadagalli**, Poorvi Bhat, Vishesh Goel, Saumen Mandal **"**Hydroxyapatite - A promising sunscreen filter**"** **Journal of the Australian Ceramic Society,** 56 (1), 2020, 345-351

OTHER PUBLICATIONS

Raj, V. A., **Komalakrushna Hadagalli,** Jana, P., & Mandal, S. Improved Fracture Toughness and Crack Arrest Ability of Graphene–Alumina Nanocomposite. **Journal of Materials Engineering and Performance**, (2021), 1-11.

CONFERENCE PRESENTATIONS

Komalakrushna Hadagalli, Kaushal R Shakya, Gavrav Kumar, Saumen Mandal, "Study of Bio-mineralization of porous hydroxyapatite scaffold developed from cuttlefish bone" 81 st Annual session of Indian ceramic society and international conference on Expanding horizons of Technological applications of Ceramics and Glasses (**EH-TACAG'17**), 14-16 December 2017, COE Pune. **(Poster presentation).**

Komalakrushna Hadagalli, Shine Jyoth T.G., R. Santhanu Panikara, Saumen Mandal, Biswanath Kundu, "Low temperature development of nano-hydroxyapatite from austromegabalanus psittacus, star fish and sea urchin", International Conference on Nanotechnology (**ICNano-2016**), 21-23 April 2016, Bangaluru, India. (**Best Poster Award).**

Komalakrushna Hadagalli, Saumen Mandal, Biswanath Kundu, "Fabrication and characterization of hydroxyapatite from Cuttlefish bone, Goose barnacles and Prawn shell to bone/hard tissue engineering approach", Fourth International Conference on Nanomedicine and Tissue Engineering (**ICNT 2016**) 12-14 August 2016, Kottayam, Kerala, India. **(Oral presentation).**

Komalakrushna Hadagalli, Gaurav Kumar, Biswanath Kundu, Saumen Mandal, "Development of porous nano-hydroxyapatite from *Austromegabalanus psittacus* marine species using camphor and wheat flour as pore formers", 2nd International Conference on Recent Advances in Nanosciences and Nanotechnology-2016 (**ICRANN-2016**), 19-20 December 2016, JNU, New Delhi, Delhi, India. (**Poster presentation**).

Deeksha M. Kodangal, Poorvi, **Komalakrushna Hadagalli,** Saumen Mandal. "Synthesis and characterization of highly dense hydroxyapatite from prawn shells (Fenneropenaeus indicus)", National Conference on Processing of Materials (**NCOPOM18),** 19-21 September 2018, NITK Surathkal. (**Best Poster award).**

Yashaswini Karanth, Meghana Banavath, **Komalakrushna Hadagalli**, Kaushal R Shakya, K Rajendra Udupa, Saumen Mandal. "Development of nano hydroxyapatite-Fe2O3 based UV absorbing sun screen filter from austromegabalanus psittacus" at **NANOBIOTECK**–2017, 6-8 December 2017, KTDC-Samudra, Trivandrum. (**Poster presentation**).

Gaurav kumar, **Komalakrushna Hadagalli**, Saumen Mandal, "Fabrication of porous hydroxyapatite from cuttlefish bone using camphor and wax as pore formers", International Conference on Material Sciences (**SCICON' 2016**), 19-21 December 2016, Amrita Vishwa Vidyapeetham, Coimbatore, India. (**Poster presentation**).

Kokila Rajaram, Sahil Hegde, **Komalakrushna Hadagalli**, K Rajendra Udupa, Saumen Mandal, "Fabrication and Characterization of Nano-Hydroxyapatite from Neptunus Sanguinolentus and Scylla Serrata", International Symposium for Research Scholar on Metallurgy, Materials Science and Engineering (**ISRS 2016**), 21-23 December 2016, IIT Madras, India. (**Poster presentation**).

Page left intentionally blank

BIO DATA

Name	:	Komalakrushna Hadagalli
Father's name	:	Basavarajappa H
Date of birth	:	21st July 1991
Permanent address	:	Amma Nilaya,274/B/1/17
		Kalamma Badavane, 10th ward
		Huvina Hadagali
		Bellari - 583219
		Karnataka, India.
Mobile	:	+91-9113520154
E-mail	:	komalkrishna121@gmail.com

Academic qualification:

Bachelor of Engineering (B.E.) in Mechanical Engineering from Basaveshwar Engineering College Bagalkot, Karnataka (CGPA: 8.55 out of 10).

Masters of Technology (M.Tech.) in Materials Engineering from National Institute of Technology Karnataka (NITK) Surathkal (CGPA: 7.69 out of 10).